Flight Validated High-Order Models of UAV Helicopter Dynamics in
Hover and Forward Flight using Analytical and Parameter Identification Techniques

by

Subodh Bhandari

M. S. A. E., Mississippi State University, Starkville, Mississippi, 2004

Submitted to the Department of Aerospace Engineering and the
Faculty of the Graduate School of the University of Kansas
in partial fulfillment of the requirements for the degree of
Doctor of Philosophy

Committee members:

_____
Chairperson: Dr. Richard Colgren

_____
Dr. David Downing

_____
Dr. Chuan-Tau Edward Lan

_____
Dr. Mark Ewing

_____
Dr. Bozenna Pasik-Duncan

Date defended:_____

The Dissertation Committee for Subodh Bhandari certifies
that this is the approved version of the following dissertation:

Flight Validated High-Order Models of UAV Helicopter Dynamics in
Hover and Forward Flight using Analytical and Parameter Identification Techniques

Committee members:

_____
Chairperson: Dr. Richard Colgren

_____
Dr. David Downing

_____
Dr. Chuan-Tau Edward Lan

_____
Dr. Mark Ewing

_____
Dr. Bozenna Pasik-Duncan

Date accepted:_____

Abstract

There has been a significant growth in the use of UAV helicopters for a multitude of military and civilian applications over the last few years. Due to these numerous applications, from crop dusting to remote sensing, UAV helicopters are now a major topic of interest within the aerospace community. The main research focus is on the development of automatic flight control systems (AFCS). The design of AFCS for these vehicles requires a mathematical model representing the dynamics of the vehicle. The mathematical model is developed either from first-principles, using the equations of motion of the vehicle, or from the flight data, using parameter identification techniques. The traditional six-degrees-of-freedom (6-DoF) dynamics model is not suitable for high-bandwidth control system design. Such models are valid only within the low- to mid-frequency range.

The agility and high maneuverability of small-scale helicopters require a high-bandwidth control system for full authority autonomous performance. The design of a high-bandwidth control system in turn requires a high-fidelity simulation model that is able to capture the key dynamics of the helicopter. These dynamics include the rotor dynamics.

This dissertation presents the development of a 14-degrees-of-freedom (14-DoF) state-space linear model for the KU Thunder Tiger Raptor 50 UAV helicopter from first-principles and from flight test data using a parameter identification technique for the hovering and forward flight conditions. The model includes rigid body, rotor

regressive, rotor inflow, stabilizer bar, and rotor coning dynamics. The model is implemented within The MathWork's MATLAB/Simulink environment. The simulation results show that the high-order model is able to predict the helicopter's dynamics up to the frequency of 30 rad/sec.

The main contributions of this dissertation are the development of a high-order simulation model for a small UAV helicopter from first-principles and the identification of a high-order model for a UAV helicopter of the size of the Raptor 50 helicopter using flight test data. Another key contribution of this research is the calculation and identification of stability and control derivatives for the Raptor 50 helicopter. These can readily be used without any further modification for the design of control systems.

Keywords: High-Order Model, Stability and Control Derivatives, Hybrid Model, CIFER, Bandwidth, Rotor Dynamics

Dedication

To,

My wife, son, daughter, and my parents

Acknowledgements

I would like to thank those who have helped me finish this work. First of all, I am extremely grateful to my advisor, Professor Richard D. Colgren, for giving me the idea for this work. Without his guidance, support, and patience, this work would not be possible. He has been a constant source of inspiration for this research and other activities.

My special thank go to my committee members, Professor David Downing, Professor Eddie Lan, Professor Mark Ewing, and Professor Passik-Dunkan Bozenna for their valuable suggestions and comments, which played a key role in fine tuning and completing the work of this dissertation.

I would also like to thank Lance Holly for all his help. His uninterrupted support in getting flight test data played instrumental role in finishing this work. I would like to take this opportunity to thank all those who have supported me in this work, especially Allwyn Samuel and Nelson Brown.

To my parents, my sincere thanks for their love and support throughout my educational career. Without their love and encouragement, I would not be at the position where I am right now.

Last but not least, I would like to thank my wife, Usha. Thanks for bearing with me throughout all these years and for keeping our hopes alive. Thanks to my son, Utkarsha, and my daughter Ashna for providing me with such joyful moments and the motivation to finish this dissertation. I finally thank Almighty God for his blessings.

Table of Contents

List of Figures

List of Tables

List of Symbols

SYMBOL	DESCRIPTION	UNIT
a	main rotor blade lift curve slope	1/rad
a_T	main rotor blade lift curve slope	1/rad
a_0	main rotor blade coning angle	rad
a_1	main rotor longitudinal flapping angle	rad
A	rotor disc area	ft^2
A_1	main rotor lateral cyclic	rad
A_b	main rotor blade area	ft^2
b_1	main rotor lateal flapping angle	rad
a_{1_s}	stabilizer bar longitudinal flapping angle	rad
b_{1_s}	stabilizer bar lateral flapping angle	rad
B_1	main rotor longitudinal cyclic	rad
C'	lift deficiency function	
C_H	rotor H-force coefficient	
C_L	rotor rolling moment coefficient	
C_{L_a}	roll moment coefficient	
C_M	rotor pitching moment coefficient	
C_{M_a}	aerodynamic flap moment about pitch axis	

C_Q	rotor torque coefficient	
C_T	main rotor thrust coefficient	
C_{T_T}	tail rotor thrust coefficient	
C_Y	Y force coefficient	
e	flap hinge offset	ft
F_{1_c}	longitudinal component of out-of-plane rotor force	lb
F_{1_s}	lateral component of out-of-plane rotor force	lb
F_r	section radial aerodynamic force	lb
F_x	force along X axis	lb
F_x	section aerodynamic force component parallel to the disk plane	lb
F_y	force along Y axis	lb
F_z	force along Z axis	lb
F_{zz}	section aerodynamic force normal to disk plane	lb
g	acceleration due to gravity	ft/sec^2
I_b	blade moment of inertia about the flapping hinge	slug-ft^2
I_x	moment of inertia of the helicopter about x axis	slug-ft^2
I_y	moment of inertia of the helicopter about y axis	slug-ft^2
I_z	moment of inertia of the helicopter about z axis	slug-ft^2

K_R	dynamic wake correction factor	
K_β	center-spring rotor flap stiffness	ft-lb/rad
K_ζ	lag hinge spring constant	ft-lb/rad
L	rolling moment	ft-lb
L_{b_1}	body roll moment due to tip path plane tilt	$1/\text{sec}^2$
$L_{f_{a_1}}$	coupling term due to rotor flapping restraint	$1/\text{sec}^2$
m_{am}	apparent mass of air	slug
M	pitching moment	ft-lb
M_{a_1}	body pitch moment due to tip path plane tilt	$1/\text{sec}^2$
$M_{f_{b_1}}$	coupling term due to rotor flapping restraint	$1/\text{sec}^2$
M_F	aerodynamic flap moment	ft-lb
$M_{F_{1c}}$	longitudinal component of aerodynamic flap moment	ft-lb
$M_{F_{1s}}$	lateral component of aerodynamic flap moment	ft-lb
M_x	rotor hub roll moment	ft-lb
M_y	rotor hub pitch moment	ft-lb
N	yawing moment	ft-lb
N , N_b	number of blades	
N_x	measured longitudinal acceleration	ft/sec^2

N_y	measured lateral acceleration	ft/sec^2
p	roll rate	rad/sec
$\overline{p}$	roll rate non-dimensionalized by Ω	
$\dot{p}$	roll acceleration	rad/sec^2
q	pitch rate	rad/sec
$\overline{q}$	pitch rate non-dimensionalized by Ω	
$\dot{q}$	pitch acceleration	rad/sec^2
r	yaw rate	rad/sec
r , r_b	blade radial coordinate	ft
R	main rotor radius	ft
R_T	tail rotor radius	ft
T	main rotor thrust	lb
T_T	tail rotor thrust	lb
u	forward velocity in body axis	ft/sec
U_p	normal rotor velocity	ft/sec
U_T	in-plane rotor velocity	ft/sec
$\dot{u}$	time rate of change of forward velocity	ft/sec^2
v	helicopter side velocity	ft/sec
$\dot{v}$	time rate of change of lateral velocity	ft/sec^2
v_i	rotor induced velocity	ft/sec

V_c	rotor climb velocity	ft/sec
V_d	rotor descent velocity	ft/sec
w	helicopter vertical velocity	ft/sec
$\dot{w}$	time rate of change of vertical velocity	ft/sec^2
X_{a_1}	longitudinal rotor force derivative	ft/sec^2
Y_{b_1}	lateral rotor force derivative	ft/sec^2
Y_T	component of Y force from tail rotor	lb
α_d	disc incidence angle	rad
β	rotor blade flapping angle	rad
β_{1_c}	longitudinal tip-path-plane tilt	rad
β_{1_s}	lateral tip-path-plane tilt	rad
β_s	stabilizer bar flaping angle	rad
δ_{col}	main rotor collective input	deg
δ_{lat}	lateral cyclic input	deg
δ_{lon}	longitudinal cyclic input	deg
δ_{ped}	tail rotor collective input	deg
γ	blade Lock number ($= \rho acR^4 / I_b$)	
γ_s	stabilizer bar Lock number	
λ_o	uniform component of the non-dimensionalized induced velocity	

λ_{1_c}	longitudinal component of the non-dimensionalized induced velocity	
λ_{1_s}	lateral component of the non-dimensionalized induced velocity	
λ_{i_h}	hover inflow ratio	
λ_i	main rotor inflow	
λ_β	flapping frequency ratio	
μ	advance ratio	
μ_c	normalized climb velocity	
μ_d	normalized descent velocity	
μ_z	normalized velocity of rotor hub in hub/shaft axis	
ϕ	helicopter bank angle	rad
ρ	air density	slug/ft^3
ψ	rotor blade azimuth angle	rad
σ	main rotor solidity ($= N_b c/\pi R$)	
σ_T	tail rotor solidity	
θ	helicopter pitch attitude angle	rad
θ_0	collective pitch angle	rad
θ_{1_c}	lateral cyclic pitch angle	rad
θ_{1_s}	lateral cyclic pitch angle	rad

θ_{tw}	main rotor blade linear twist	rad
ν_{ζ}	lag frequency ratio	
ω	natural frequency of dynamic modes	rad/sec
Ω	main rotor speed	rad/sec
Ω_T	tail rotor speed	rad/sec

1 Introduction

This chapter presents previous helicopter dynamics modeling work followed by a summary of this research. In the first section of this chapter, an overview of this research is presented. Section two is the background section of this dissertation. The third section discusses helicopter dynamics modeling techniques. Previous work on helicopter dynamics is discussed in the fourth section. The fifth section presents an outline of the present work. In the sixth section, the contributions that the present work makes to the helicopter dynamics modeling community are discussed, followed by a description of the Raptor 50 helicopter. Finally, the organization of this dissertation is presented.

1.1 Overview

There has been a significant growth in the use of UAV helicopters for a multitude of military and civilian applications over the last few years. Due to these numerous applications, from crop dusting to remote sensing, UAV helicopters are a major topic of interest within the aerospace community. With the availability of highly accurate and miniaturized sensors like micro electronic sensors (MEMS), the research focus is on developing models for the design of autonomous flight control systems (AFCS) embedded within the avionics system.

Helicopters can take-off and land vertically, can hover, and also have the capability for forward flight. These features make helicopters suitable for several operations that the fixed-wing aircraft cannot easily achieve. Helicopter UAVs have

the further advantages of size, agility, and maneuverability. These qualities make the UAV helicopters suitable for various tasks such as battleground monitoring without risking the loss of human life.

Helicopter dynamics are inherently unstable. This requires continuous attention from the pilot, which can be very fatiguing and can even lead to accidents. This, in turn, requires a stability augmentation system (SAS) and an AFCS. The intended use of UAV helicopters as autonomous vehicles also require an SAS and AFCS installed onboard. The design of the SAS and AFCS usually require mathematical models that represent the flight dynamics of the helicopter[1]. The mathematical models for the helicopters are either single-input-single-output (SISO) models in the form of transfer functions or multiple-input-multiple-output (MIMO) models in the form of 6-DoF state-space models[2, 3].

The agility and high maneuverability of small-scale helicopters require a high-bandwidth control system for full authority autonomous performance. The design of a high-bandwidth control system, in turn, requires a high-fidelity simulation model that captures the key dynamics of the helicopter[4]. Traditional 6-DoF dynamics models, in which rotor dynamics are modeled using the quasi-static assumption[3,5], are not suitable for high-bandwidth control system design. Such models are valid within the low- to mid-frequency range (0.5-8 rad/sec). To obtain a model that is valid over the entire frequency range of interest (up to 30 rad/sec), rotor flapping and lead-lag dynamics need to be explicitly modeled as separate degrees-of-freedom[6, 7, 8, 9]. Also

important are the rotor inflow dynamics. For small-scale UAV helicopters, the stabilizer bar plays a very important role, and its dynamics must be modeled in order to get an accurate and a high-fidelity model[10].

This dissertation presents the development of a 14-degrees-of-freedom (14-DoF) state-space model for a KU Thunder Tiger Raptor 50 V2 UAV helicopter (Raptor 50) using analytical and parameter identification techniques. The model includes the rotor flapping degrees-of-freedom, rotor inflow dynamics and stabilizer bar dynamics. No work exists in the literature on the development of a high-order model for the helicopter of the size of the Raptor 50. The high order model presented in this dissertation can be used by anyone working on the Raptor 50 without further model develpment. This is the primary contribution of this dissertation. Other unique contributions are: consideration of parameter variation in the model development of a UAV helicopter and inclusion of inflow dynamics in the model.

1.2 Background

Unlike fixed-wing aircraft, helicopters possess significant coupling between the longitudinal and the lateral dynamics. One of the main sources of this coupling is the rotor flapping due to pitch and roll velocities[11]. An offset in the flapping hinge also causes a coupling between the two dynamics. Ref. 11 provides further detail about different sources of coupling between the longitudinal and the lateral dynamics of helicopters.

Due to couplings and other complexities, the development of a model for the

helicopter is much more difficult than for their fixed-wing counterparts. These complexities arise mainly due to the rotor being a complex dynamic system. In helicopters, the rotor is responsible for producing lifting forces. The rotor is also used for controlling the helicopter. Since the rotor is a dynamic system, the forces produced by it not only depend on the pilot input, but also on the rotor states. Also, the rotor behavior changes significantly as the helicopter moves from one flight regime to another, e.g., from hover to forward flight and from hover to vertical flight, etc. These properties make the development of dynamics models for helicopters extremely difficult.

A significant amount of research is ongoing in helicopter dynamics modeling due to these difficulties. One of the problems the rotorcraft dynamic modeling communities faces is in the off-axes response (the roll rate due to the longitudinal cyclic or the pitch rate due to the lateral cyclic). The traditional six-degree-of-freedom (6-DoF) models give the off-axes responses in the wrong direction as compared with the flight data. There is usually a 180° phase difference between the flight data and the model prediction. For a long time, the cause of this error was not understood. Another problem the community faced was that the 6-DoF models were able to predict the helicopter dynamics only at the lower frequencies. Such models were not sufficient for the high-bandwidth control systems required for the helicopters.

For high-bandwidth control system design, the models that could predict the

helicopter dynamics accurately at the mid- and high-frequencies were required. This required an explicit modeling of the rotor dynamics that comes into play at the higher frequencies.

The past decade has seen a rapid growth in the use of UAVs, from military applications, such as battleground monitoring, weapon dropping, border surveillance et cetera, to civilian uses such as remote sensing, crop dusting, fire fighting, etc. The use of UAV helicopters is also on the rise, in part due to their unique capabilities. Consequently, there has been a significant research effort on UAV helicopters, mostly on the development of autonomous UAV helicopters.

Various universities and organizations are doing research on helicopter UAVs. The premier organizations that are involved in helicopter UAV research include Georgia Tech, Carnegie Mellon University, MIT, and the U. S. Army Aeroflightdynamics Directorate (AFDD). Georgia Tech is conducting dynamics and controls research on Aerial Robotics and Vision Based Control Systems using an R-MAX UAV helicopter[12], while Carnegie Mellon has used its Yamaha R-50 helicopter for research on vision-based guidance[13]. MIT researchers used an X-Cell 60 UAV helicopter for autonomy research and dynamics modeling of aerobatic maneuvers[14, 15]. AFDD at the Ames Research Center is doing research on its R-MAX helicopter for flight dynamics, control and simulation studies[16].

Intelligent Uninhabited Air Vehicles represent a major area of multidisciplinary systems-oriented research and development at The University of Kansas (KU). The

research emphasis at KU is on designing, modeling, and flight-testing these vehicles to develop accurate dynamic computer simulations. Another key research topic to enable unpiloted vehicles as viable systems is the development of reliable autonomous control technologies implemented within embedded computer systems. Figure 1 shows the KU R-MAX and Raptor 50 helicopters that are being used as research vehicles.

Figure 1: Yamaha R-MAX and Raptor 50 V2 Helicopters

1.3 Helicopter Modeling Techniques

There are currently two approaches to the development of a simulation model for helicopters. The first approach is the parameter identification technique, in which the data obtained during flight tests are used to extract a simulation model. This approach is relatively simple, and no a-priori knowledge of the dynamics system is required.

However, this method generates models that are valid for particular flight conditions and thus are not suitable for the development of a control system that is valid for an entire flight envelope. Another limitation to this approach is that it cannot be used for vehicles that are still in the design phase. It requires a vehicle ready to fly, so that flight data for parameter identification can be collected. Despite these limitations, parameter identification techniques so far dominate the work done on helicopter dynamics modeling for control system design applications. CIFER (Comprehensive Identification from FrEquency Response)[17] software developed by the U.S. Army, NASA, and Sterling Software has been used extensively for this purpose. Other software such as MMLE has also been used for parameter identification of helicopter dynamics[18]. Even with the parameter identification technique, a model structure has to be defined that explicitly models the rotor degrees-of-freedom (in order to get a model that captures the rotor dynamics) and that is suitable for the design of a high-bandwidth control system. In Ref. 19, Tischler and Cauffman have developed a hybrid model for the BO-105 helicopter, taking into account the coupling between rotor and fuselage dynamics.

The development of an autonomous system requires a simulation model that is valid over a large portion of the flight envelope. Such a model can be developed from first principles using the equations of motion for the helicopter's flight dynamics. The development of such a model requires significant knowledge about the flight dynamics of the helicopter. This approach does not require flight data, and can predict

the dynamic response of a helicopter that is still in the design phase. The initial development of the analytical model from first principles is time consuming. Once developed, however, analytical models can be generated for different vehicles and for different flight conditions just by supplying the appropriate geometric and mass characteristics of the helicopters.

1.4 Literature Survey

As discussed earlier, due to complexities involved with the rotorcraft dynamics modeling, the rotorcraft research community has not been able to develop models for helicopters equivalent to the models for fixed-wing aircraft in terms of accuracy. The difficulty mainly arises due to the rotor being a complex rotating system, which is responsible for producing lift and controlling the helicopter attitude. The unsteady aerodynamics involved with the rotor inflow dynamics[20] further complicates the rotorcraft dynamics modeling. Another important aspect is that different helicopters come with different rotor head designs[3]. Rotor flapping and lead-lag dynamics are other aspects that complicate rotorcraft modeling. Further, the helicopters can take off and land vertically, and posses the capability for forward flight like fixed-wing aircraft. These features complicate the development of a model that is valid for all helicopters and for all flight regimes.

Due to these difficulties, the rotorcraft community depends more on parameter identification techniques rather than theoretical modeling, though analytical modeling is necessary to understand underlying principles. Since traditional 6-DoF models are

not able to capture high-frequency dynamics and are not suitable for high-bandwidth control system design, current research focuses on the development of a high-order model that includes rotor degrees-of-freedom. A significant amount of work has been done on the development of high-order mathematical models from first-principles for full-scale helicopters. An example is the GenHel[21] nonlinear simulation code developed by Sikorsky Aircraft for the UH-60 Black Hawk Helicopter. This model is comprehensive and includes rigid body, rotor flapping and lead-lag, rotor speed, and rotor inflow degrees-of-freedom. The model proved to be useful for motion analysis and the pilot-in-the-loop simulation. However, the model was not suitable for the design of control systems using the existing and the most prevalent linear control system design techniques. In Ref. 22, Kapilta, et al. used the GenHel code for the CH-53E helicopter to show the validity of the code in the frequency-domain. The authors also showed the shortcomings of the GenHel code and suggested improvements.

Refs. 4 and 23 discuss about the extraction and validation of a high-order linear model from the GenHel simulation code. This model includes the rotor flap and lag-degrees-of-freedom as well as the rotor inflow dynamics. The model prediction showed a high degree of correlation with the flight data. The validity of a reduced order model was also demonstrated in these works. Another example of the extraction of a high-order linear model from the GenHel code is found in Ref. 24. In this reference, a linearized model was extracted from the GenHel code for the UH-60 Black Hawk helicopter. The author showed the high frequency rotor modes that can

couple with the fuselage dynamics as shown in Figure 2. In the figure, it is seen that the rotor regressive flap, lag, uniform inflow, and collective lag modes are at frequencies that are close to the rigid body modes (body pitch and roll modes, etc.).

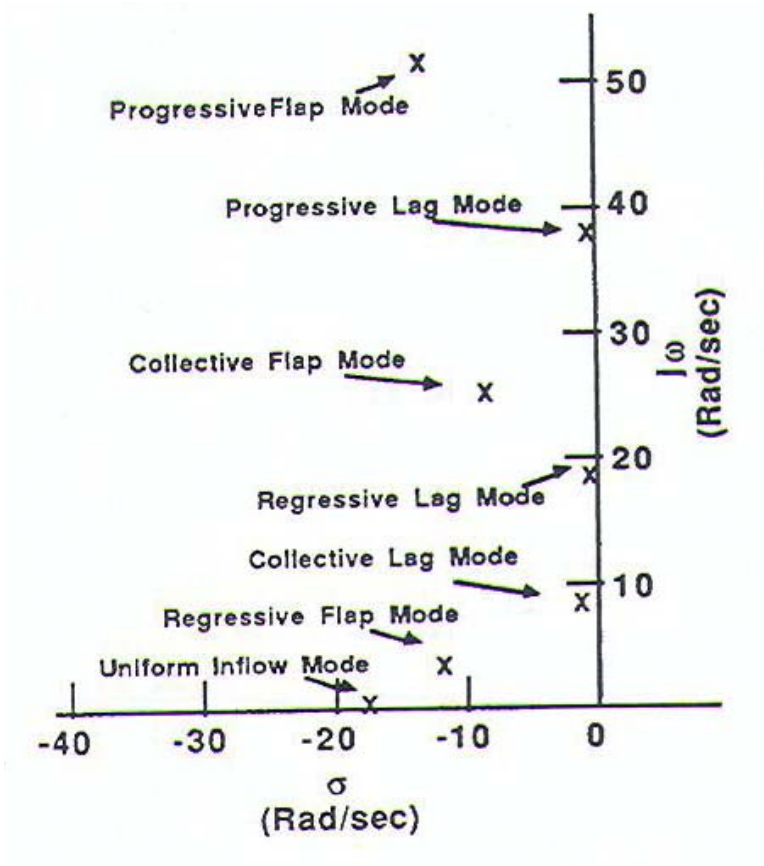

Figure 2: High Frequency Rotor Modes for the UH-60 Helicopter

In the reference, the author also showed the limitation of the 6-DoF models on the roll rate feedback gain as shown in Figure 2 and Figure 3[24]. It is clear from the figure that when the gain is increased, the regressive flap/body mode moves toward right-half plane, causing vibration and instability.

Refs. 25 and 26 discuss the validity of the GenHel code via flight test data and

parameter identification in time- and frequency-domains.

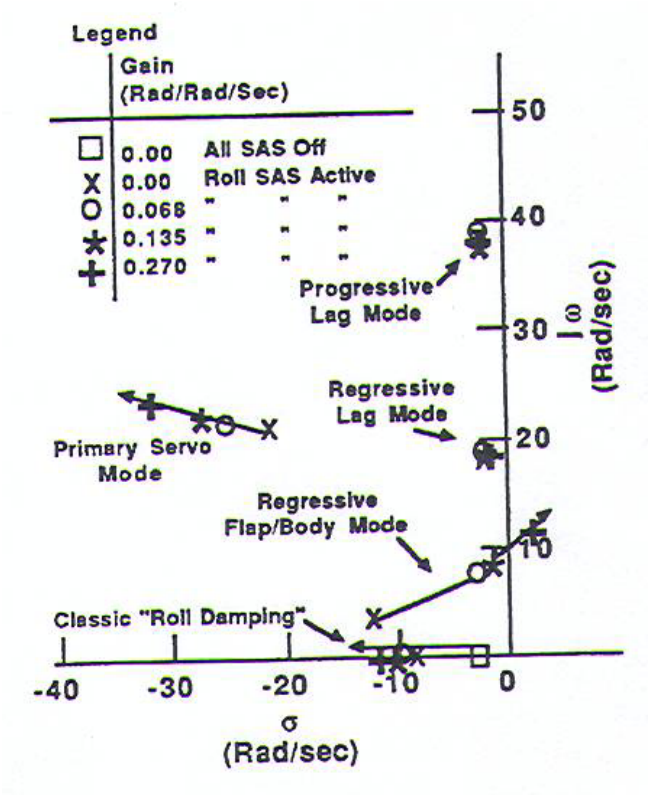

Figure 3: Roll Rate to Lateral Cyclic Root Locus for the UH-60 Helicopter

A helicopter mathematical model named ARMCOP[27] is another example of a high order (10-DoF) nonlinear, total force and moment model that includes six rigid body, three rotor flapping, and rotor rotational degrees-of-freedom. The model is suitable for the piloted simulation. Ref. 28 discusses the effect of the addition of the dynamic inflow and the rotor lead-lag dynamics into the ARMCOP model with emphasis on the improvement in the model response.

In Ref. 29, Curtiss and Zhao describe a method for obtaining a high-order linearized model using a symbolic automatic equation-generating program called

Reduce implemented in the MACSYMA[30] software. The model includes rigid body, rotor flapping, lead-lag, and rotor inflow dynamics. This linear model was validated via flight test data. The authors' emphasis is on the inclusion of rotor dynamics to have a model that is valid at higher frequencies, and is suitable for the design of high-bandwidth control systems. Ref. 31 discusses the influence of rotor dynamics and the dynamic inflow on the stability and the control characteristics of helicopters in near-hovering flights. The paper discusses the body attitude and the rate feedback limitations that arise due to rotor flapping, lag, and inflow dynamics. It is shown that attitude feedback gain is limited by body-flap coupling and rate gain is limited by lag-body coupling. Also discussed are resulting instabilities when a control system devised on the quasi-static flapping assumption is applied to a model with flapping dynamics included.

The stability and the control characteristics for the hingeless rotors are discussed in Ref. 32. The paper focuses mainly on the induced flow field and rotor flapwise bending modes with emphasis on the importance of the rotor-fuselage coupling.

Ref. 33 showed the influence of the high-order rotor flapping dynamics on the 6-DoF stability and control derivatives. It was shown that a model with the rotor dynamics was found to be a substantial improvement over the conventional model, effectively doubling the relative bandwidth and providing a more accurate representation of the short-period and the cross-axis characteristics. In Ref. 34, McKillip and Curtiss have suggested an approximate form for augmenting the linear

rotor/body response to include the rotor lag dynamics. The authors discuss the implication of the approximation, and the effect of the lag dynamics on stability with body rate feedback.

The modeling of helicopter dynamics started in the 1950's and is still going on. The modeling effort up to 1970 used analytical techniques. The early 1970's saw the advent of the development of mathematical models of helicopter dynamics using parameter identification techniques. Since helicopter dynamics are extremely complex, and the analytical models were not able to predict the helicopter dynamics at higher frequencies, it was realized that there was a need for the development of mathematical models using flight data that would more accurately predict helicopter dynamics. Though model development using parameter identification techniques has certain limitations, it has become a popular model building technique among the rotorcraft dynamics modeling community. Unlike analytical modeling techniques, this technique is not suitable for the development of models for helicopters that are still in the design phase. Another limitation is that each flight condition requires a separate model identified for it. Nonetheless, there is a lot of current work on using parameter identification techniques. Accurate determination of the stability and the control derivatives (S&C) from the flight test data is useful for handling qualities assessment, better AFCs design, stability prediction, etc.

In the early 1970's, there were several works accomplished in the identification of the S&C derivatives for both fixed- and rotary-wing aircraft. Refs. 35 and 36 discuss

early work on the extraction of the S&C derivatives from the flight test data. These works have usually been characterized by 3-DoF models. Ref. 37 presented a method to extract the helicopter stability derivatives using Kalman Filtering, and extended the method to extract a 6-DoF model. In Ref. 38, the author applied a Bayesian approach to estimation in the identification of S&C derivatives from the flight data for a CH-53 helicopter flying at 100- and 150-knot trim conditions. The paper highlighted the need for at least a 6-DoF model for the helicopter to capture the key dynamics.

Research on a XV-15 tilt rotor aircraft started the frequency-domain approach to the parameter identification of the S&C derivatives for fixed- and rotary-wing aircraft. Ref. 37 talks about the identification of the open-loop dynamics of the XV-15 aircraft. In the paper, piloting and data analysis techniques are presented to determine frequency response plots and equivalent transfer function models. It was shown that the open-loop pitch and roll dynamics for the hovering flight condition exhibit unstable low-frequency oscillations, whereas the dynamics in the remaining degrees-of-freedom are lightly damped and generally decoupled.

The early work on the parameter identification of the S&C derivatives focused on 6-DoF models. These models suffered from the problem, as did the models developed from first principles, of not being able to predict the dynamics at the higher frequencies. The need to model the rotor dynamics explicitly was identified and the work thereafter focused on the development of a high-order model including rotor dynamics. Ref. 38 talks about the identification of 9- and 12-DoF linear models of

rotor-fuselage dynamics from nonlinear simulation data. The resulting models were used to evaluate the coupling of the fuselage modes with the rotor flapping and lead-lag modes at various frequencies. In Ref. 19, the authors present a comprehensive frequency-response method for the system identification of coupled rotor/fuselage dynamics of a BO-105 helicopter. The authors used CIFER to identify a 9-DoF hybrid model of the helicopter from the flight test data. The identified model includes the coupled body/rotor flapping and lead-lag dynamics, and is accurate up to the frequency of 30 rad/sec. An application of the model to the design of a flight control system showed that the maximum roll rate gain is limited by the destabilization of the lead-lag dynamics.

Refs. 39, 40, and 41 are some of the other works related to the identification of a model including rotor degrees of freedom. In Ref. 39, the authors investigate the use of higher order models that include rotor-degrees-of-freedom in the system identification of a BO-105 helicopter. The authors developed two different models of 10th and 14th order. The 10th order model included first order rotor dynamics while the 14th order model included second order flapping and second order coning dynamics. The prediction capability of the identified model was demonstrated in the verification results. Ref. 40 discusses the development of a high-order model that includes the rotor lag degree-of-freedom and structural modes for a CH-53 helicopter. It is shown that the higher order dynamics of the helicopter are dominated by rotor and structural modes.

Some of the helicopter dynamics modeling work using parameter identification included rotor inflow dynamics. The dynamics associated with rotor inflow have similar time scales to the rotor flapping dynamics, and are strongly coupled with the flap and the fuselage-degrees-of-freedom as discussed in Ref. 31. In Ref. 42, Fletcher discusses the identification of a 14-DoF model, which characterizes the open loop UH-60 flight dynamics in hover using a frequency-response-error-identification method. The model includes rigid body fuselage dynamics, regressing rotor flapping and rotor lead-lag dynamics, main rotor inflow, rotor RPM, and engine governor dynamics. It is shown that the model is applicable within the frequency range of 0.1 to 20 rad/sec. The identified model predicts the on-axis response of the helicopter and has superior off-axis fidelity. The effect of the dynamic inflow on the vertical acceleration response to collective input is also discussed. Ref. 43 talks about the development of a high-order state-space model using CIFER for a SH-2G flapped helicopter. The model includes the coupled rotor/fuselage/engine/inflow dynamics. The model was developed to support the development of a new digital flight control system and piloted simulation. It is shown that for the control system design and the simulation applications, the model should include fuselage rigid body dynamics, rotor regressive flapping dynamics and rotor coning dynamics, dynamic inflow, and engine responses to accurately match the SH-2G response in the frequency range of interest.

Refs. 44, 45, and 46 are other examples of the development of high-order flight mechanic models using parameter identification techniques. In Ref. 44, the authors

developed a mathematical model for the design of a model following control system for a BO-105 helicopter. It was shown that the 6-DoF model was not appropriate for the control system design because the model cannot predict the initial response characteristics. An extended model with 8-DoF, including rotor dynamics effects, was derived and identified. An application of a system identification method to high-bandwidth rotorcraft flight control system design is discussed in Ref. 45 by Tischler. The author shows that there is the need for including coupled body/rotor flapping and lead-lag dynamics in the identification model structure to allow the accurate prediction of control system bandwidth limitations. Schroeder et al. in Ref. 46 developed a 7-DoF hover model for an AH-64 Apache helicopter for use in the testing of a hover-display design. The developed model was an extended 6-DoF stability derivative characterization extracted from an extensive flight database.

One major problem the rotorcraft community faced was the prediction of off-axes responses by the dynamic models in the wrong direction. The longitudinal-cyclic-to-roll-rate and lateral-cyclic-to-pitch-rate responses had a 180^0 phase error when compared with the flight data. There were discrepancies in the magnitude of the responses as well. This became a major area of research during the late 1980's and early 1990's. In Ref. 47, Mark Tischler et al pointed out that the induced velocity model was the source of this error. A work by Rosen and Isser[48] supported this claim. This work showed that the wake distortion due to angular rate was responsible for the sign change. However, the model is not suitable for incorporation into the flight

dynamics model.

J. D. Keller in his papers introduces a dynamic wake correction factor to account for the effect of the rotor pitching and rolling velocities on the induced velocity distribution[49, 50]. He showed that the steady pitching and rolling motion created a distortion in the wake, and that neglecting this distortion was the source of the error in the off-axes responses. With the introduction of the dynamic wake correction factor into the induced velocity model, there was a significant improvement in the off-axes responses.

Another way proposed to improve the off-axis response is the introduction of an aerodynamic phase-lag[51, 52]. As discussed in these references, the aerodynamic phase lag is a first order lag method for correcting off-axes responses. The lag subsumes the influence of several factors including the dynamic wake distortion and 2-D compressible unsteady aerodynamic effects[53].

Compared to their full-scale counterparts, fewer publications exist on the dynamic modeling of small-scale unmanned helicopters. Most of the existing models were generated using parameter identification techniques. Bernard Mettler et al. in Ref. 14 developed and validated a nonlinear model for an X-Cell helicopter. The model was integrated into a real-time hardware-in-the-loop simulation environment used for the development of flight control systems. Refs. 10 and 13 talk about the development of a linearized mathematical model based on a hybrid model formulation for a Carnegie Mellon R-50 helicopter. This model includes the rotor regressive flapping mode and

the stabilizer bar dynamics. Integrated modeling techniques that use both the analytical modeling and the parameter identification techniques are described in Refs. 54 and 55. These models include rotor flapping degrees-of-freedom, inflow dynamics, and stabilizer bar dynamics. Ref. 56 describes the modeling of a UAV helicopter from first principles and discusses the dynamics of the stabilizer bar without providing simulation results.

1.5 Research Outline

This dissertation documents the development of a 14-degrees-of-freedom (14-DoF) state-space model for a KU Thunder Tiger Raptor 50 V2 UAV helicopter using analytical and parameter identification techniques. A model was first developed from first principles for hovering and forward flight conditions within the MATLAB/Simulink[57] environment. The model includes the rotor longitudinal and lateral flapping degrees-of-freedom, modeled as first-order equations, and the rotor coning dynamics, modeled as a second order equation. The coupling between the rotor and the body dynamics is discussed. The model also considers the coupled heave-coning-inflow dynamics. The rotor inflow dynamics are modeled as separate degrees-of-freedom. The effect of the stabilizer bar on the helicopter's stability is discussed and the bar dynamics are included. Dynamic wake distortion due to roll rate and pitch rate is discussed, and a correction factor is included in the model to improve the off-axes responses[49, 50].

As discussed earlier, in the state-space formulation, the rotor forces and moments

are represented by S&C derivatives that are functions of aircraft mass and geometric characteristics, speed, altitude, etc[30]. At each time step of the simulation, the new flight conditions (u, v, w, θ, et cetera) are fed back into the model resulting in a linear parameter-varying (LPV) model. With this approach, the simulation becomes more representative of the actual flight dynamics.

After successful completion of the model development using the documented analytical technique, flight test data was used in the development of the model using a parameter identification technique. The model developed using the parameter identification is a reduced order model and does not include longitudinal and lateral inflow dynamics. Longitudinal and lateral inflow dynamics are dropped from the identification model structure because the sensor package is not able to measure the inflow velocity components. Indeed, there exists no mechanism to measure these velocities. The model includes rigid body, rotor flapping, coning, inflow, and stabilizer bar dynamics.

1.6 Contributions to the Literature

The present thesis makes a number of contributions to the dynamics modeling of small-scale UAV helicopter. The key contributions are described below:

- Development of a high-order state-space model for the Raptor 50 helicopter from first principles. No work exists in the literature in the development of a comprehensive dynamics model for small-scale helicopters from first principles only.

- Development of a LPV model. No prior work has used this approach in the development of a high-order model. With this approach, the simulation becomes more representative of the actual flight condition.
- Development of a high-order model using a parameter identification technique. No work exists in the literature on an identified model for a UAV helicopter of the size of the Raptor 50.
- Inclusion of Heave-Coning-Inflow dynamics in the identification model. There are very few publications in the open literature that have included heave-coning-inflow coupling within the identification model structure.
- Calculation and identification of the S&C derivatives for the Raptor 50 helicopter. These derivatives can be used without any further modification for the design of control systems and for other research purposes.

1.7 Description of the KU Raptor 50 Helicopter

The Thunder Tiger Raptor 50 V2 helicopter is a small helicopter intended for acrobatic maneuvers. It is manufactured by the Thunder Tiger Company in Taiwan and is very popular among hobby pilots. A number of universities are using different variants of Raptor helicopters for various research purposes. These include the University of Texas at Arlington, which is using a Raptor 60 helicopter for the design of a robust controller for the helicopter[58] and Yuan Ze University in Taiwan[59] is using the Raptor 50 helicopter for a simulation model of attitude dynamics.

Two Raptor 50 V2 UAV helicopters were purchased for this research. One was

intended to be a flight test article, while the other serves as a backup and training helicopter.

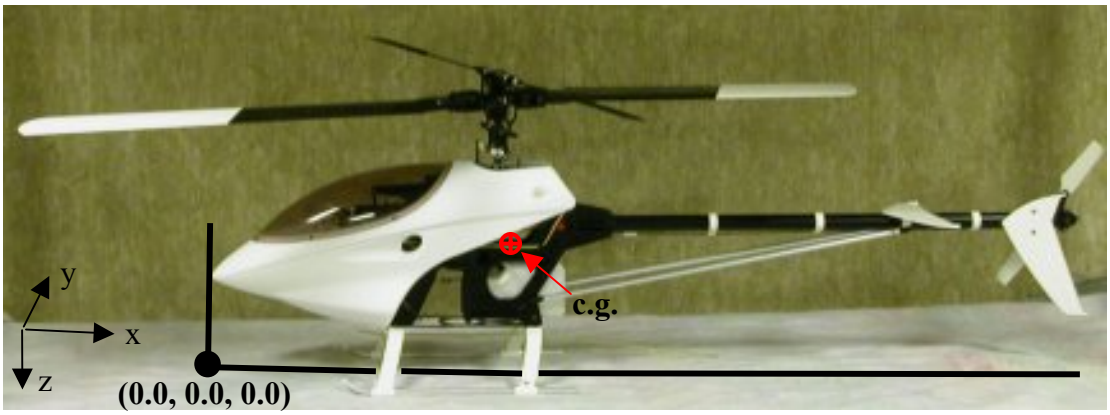

Figure 4: KU Raptor 50 V2 Coordinate System

The center of gravity locations were calculated using three scales. The moments of inertia were calculated using an analytical approach and the parallel-axis theorem as discussed in Ref. 60. The coordinate system used for the helicopter is shown in Figure 4[61]. The center of gravity location in the x direction (fuselage station) is given as a distance that starts at the nose of the helicopter. In the y direction (butt line), the origin is located at the centerline of the helicopter. The origin of the z-axis (water line) is given from the ground.

The helicopter was instrumented to collect flight data as shown in Figure 5. The instruments installed and the purpose of each instrumentation is listed in Table 1.

The flight test instrumentation package is capable of simultaneously recording 12 analog channels and 4 digital channels while sampling at from 0.00027 to 512 Hz. The sampling frequency dictates the data recording duration. For example, a sampling rate of 120 Hz allows data to be collected for approximately 6 minutes, while 512 Hz

sampling allows only 80 seconds of data to be collected.

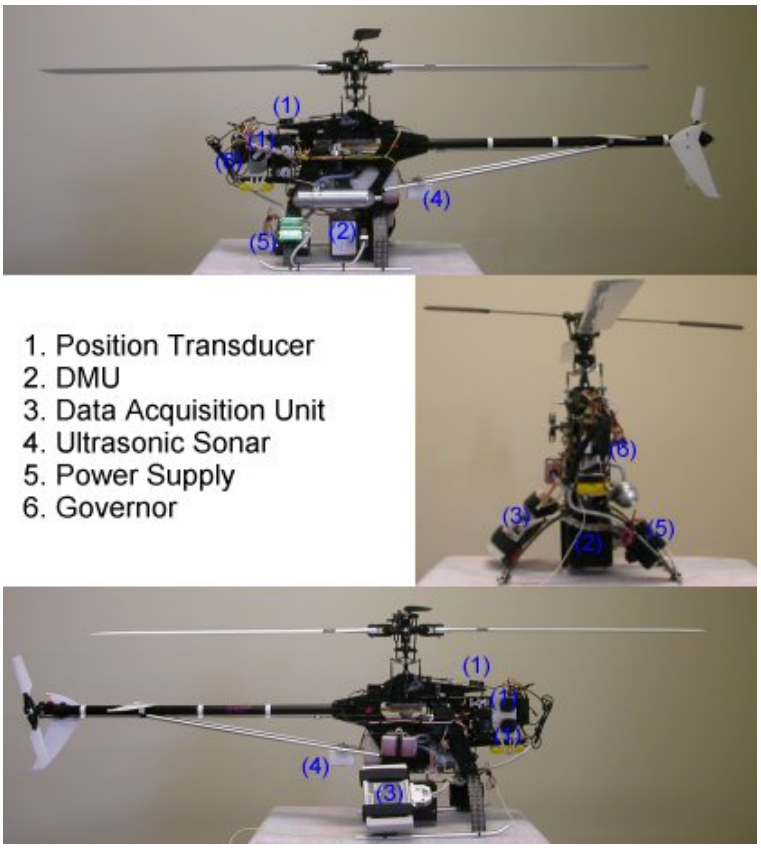

Figure 5: Instrumented Raptor 50 V2 Helicopter

Table 1: Raptor 50 V2 Instrumentation

Instrumentation	Purpose
4 Position Transducers	To measure inputs from the pilot: Main Rotor Collective Servo Pitch Cyclic Servo Lateral Cyclic Servo Tail Rotor Collective Servo
Crossbow Dynamic Measuring Unit (DMU) – Model H6X	To measure the 3 axis linear accelerations and the 3-axis rotation rates.
Crossbow 16 Channel Data Acquisition Unit – Model Ready DAQ AD2012	To collect and store flight data for post-processing.
Power Supply (4 9-Volt Batteries)	To provide constant 18-volt power to the previously mentioned devices.
Governor	To maintain constant main rotor rpm

Table 2 shows the specifications of the Raptor 50 before and after the instrumentation was added.

Table 2: Raptor 50 V2 Stock and Flight Article Specifications

Parameter	Stock	Flight Article
Fuselage Length, in.	47.24	47.24
Fuselage Width, in.	5.51	5.51
Main Rotor Diameter, in.	52.95	52.85
Tail Rotor Diameter, in.	9.26 in	9.26 in
Main Rotor Gearing Ratio	8.50	8.50
Tail Rotor Gearing Ratio	4.56	4.56
Empty Weight, lbs.	7.22 lbs.	10.34 lbs.
Gross Weight, lbs.	7.85 lbs.	10.97 lbs.
x_{cg}, in.	15.73	15.26
y_{cg}, in.	-0.44	-0.47
z_{cg}, in.	-7.42	-7.12
I_{xx}, slug-ft^2	0.0782	0.0782
I_{yy}, slug-ft^2	0.1973	0.1973
I_{zz}, slug-ft^2	0.1926	0.1926

1.8 Organization of the Dissertation

This dissertation is organized as follows. Chapter 1 is an introduction, and mainly discusses previous work on helicopter dynamics modeling. Rotorcraft modeling techniques are discussed along with the background of the research. This chapter also talks about the contribution that this research will have in the area of UAV helicopter dynamics modeling.

In Chapter 2, the theory behind the development of a high-order state-space model is discussed. The first section discusses about the rigid body dynamics. The Rotor

flapping dynamics are covered in the second part. In the third section, the rotor lead-lag dynamics are discussed. The rotor inflow dynamics are discussed in the fourth section. The fifth Section discusses about the tail rotor dynamics. The stabilizer bar and its effect on small-scale helicopters are covered in the sixth section.

In Chapter 3, the approach used in the development of a high-order LPV model is discussed. The first section talks about the rotor body coupling. This section also talks about the hybrid model formulation that combines low frequency body dynamics and high frequency rotor dynamics within a single model. The coupling between the main rotor and the stabilizer bar is covered in the second section. The third section talks about the heave-coning-inflow dynamics. Development of the LPV model is discussed in the fourth section.

Chapter 4 is about the model development using CIFER. The first section covers the theory of frequency response analysis, which includes the definition of frequency response and the method for the calculation of the frequency response that is specific to CIFER. In Section 2, various tools that are used by CIFER for frequency response calculation and parameter identification are described. Various advantages to using CIFER as a parameter identification program are discussed in Section 3. Section 4 is about the flight tests and the flight data acquisition. This section focuses on the ways for obtaining the flight data that can most efficiently be used for identification using CIFER. Some of the flight test rules that must be followed in order to obtain good quality flight data are discussed. Section 5 outlines the model development process,

which talks about the extraction of a model of different orders at different stages. Finally, in Section 6, different methods to check the accuracy of the identified model are discussed.

Chapter 5 presents the results and the verification of the developed models. In the first section, the calculated and the identified derivatives are tabulated. A frequency domain comparison between the theoretical model, the identified model, and the flight data is presented in the second section. This is followed by a time domain comparison between these models and the flight data in the third section. A comparison between the calculated and the identified derivatives is presented in the fourth section. This section also compares the eigenvalues of the helicopter dynamics obtained from the theoretical and analytical models.

In Chapter 6, concluding remarks of this research are discussed. Future work and research recommendations are made in Chapter 7, followed by references and appendices.

2 Theoretical Background

The basis for the development of a mathematical model for any dynamic system is the equations of motion representing the dynamic system. The equations of motion are usually derived using Newtonian mechanics. For helicopters, which are complex dynamic systems, the equations of motion relate the aerodynamic, inertial, centrifugal, and gravitational forces acting on the helicopter.

As with their fixed-wing counterparts, there has been a tradition of building 6-DoF simulation models of helicopters using the quasi-static assumption. In the quasi-static assumption, helicopters are represented as a rigid body. The steady-state rotor forces and moments are absorbed into the rigid body model. However, for the design of a high-bandwidth control system, the rotor dynamics must be modeled explicitly. For small-scale UAV helicopters, also important is the stabilizer bar's dynamics. In the following, rigid body, rotor and stabilizer bar dynamics are discussed.

2.1 Rigid Body Dynamics

The rigid body fuselage dynamics are modeled using equations of motion that describe the rotational and translational motion of the helicopter along and about the three axes as shown in Figure 6[20]. These three force and three moment equations are derived using Newtonian mechanics. Ref. 11 discusses in detail the derivation of these equations and are given as follows:

$$F_x = mg\sin\theta + m(\dot{u} + q \cdot w - r \cdot v) \tag{2.1}$$

$$F_y = -mg\sin\phi + m(\dot{v} + r\cdot u - p\cdot w) \tag{2.2}$$

$$F_z = -mg\cos\theta + m(\dot{w} + p\cdot v - q\cdot u) \tag{2.3}$$

$$L = I_x\cdot\dot{p} - I_{xz}\cdot\dot{r} + q\cdot r(I_z - I_y) - I_{xz}\cdot p\cdot q \tag{2.4}$$

$$M = I_y\cdot\dot{q} + r\cdot p(I_x - I_y) + I_{xz}\cdot(p^2 - r^2) \tag{2.5}$$

$$N = -I_{xz}\cdot\dot{p} + I_z\cdot\dot{r} + p\cdot q(I_y - I_x) + I_{xz}\cdot q\cdot r \tag{2.6}$$

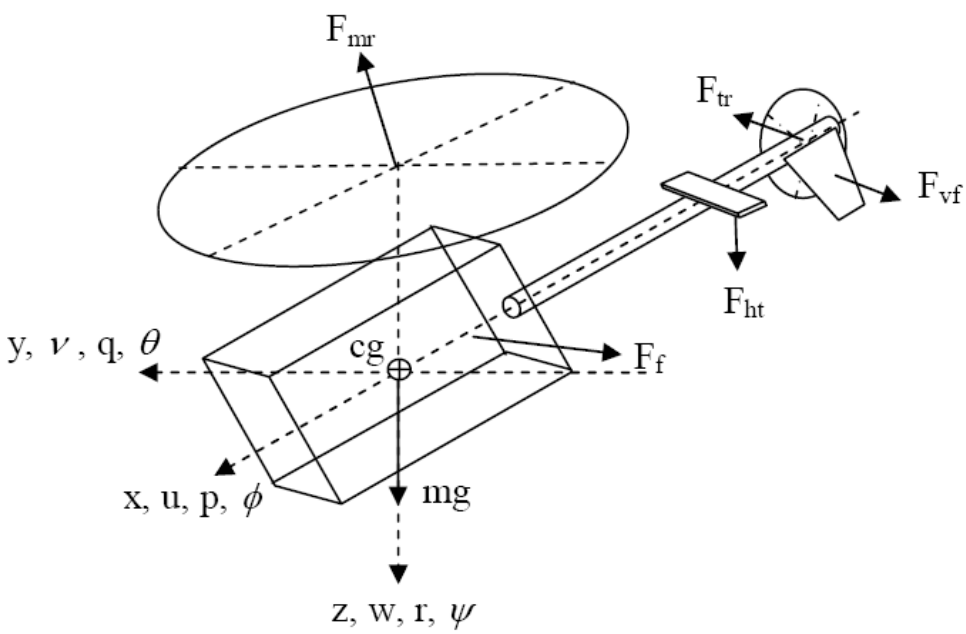

Figure 6: **Diagram Showing Three Axes System along with Principal Variables**

Total forces and moments result from contributions of the main rotor, the tail rotor, the horizontal tail, the vertical tail, and the fuselage. The equations given above are nonlinear. Small perturbation theory and a Taylor series expansion about a trim point are used to linearize these equations[11]. The linearized equations are much easier to use. They are suitable for the analysis of the aircraft's motion and for the design of

control systems. Furthermore, the main advantage of the linearized equations is that they can be used in a state-space formulation. The linearized equations, for example, can be written in the following form:

$$m \cdot \dot{u} = X_u \cdot \Delta u + X_w \cdot \Delta w + X_q \cdot \Delta q + X_p \cdot \Delta p + X_r \cdot \Delta r + X_{\delta_{col}} \delta_{col} + X_{\delta_{ped}} \delta_{ped} + X_{\delta_{lon}} \delta_{lon} + X_{\delta_{lat}} \delta_{lat} \tag{2.7}$$

In the above equation, $X_u = \frac{\partial}{\partial u} X$, $X_w = \frac{\partial}{\partial w} X$, et cetera, are the stability derivatives, and $X_{\delta_{col}} = \frac{\partial}{\partial \delta_{col}} X$, $X_{\delta_{lon}} = \frac{\partial}{\partial \delta_{lon}} X$, et cetera, are the control derivatives. The stability and the control derivatives are functions of aircraft speed and altitude. The formulas for these derivatives are similar to the formulas for the lift and the drag forces. For example, the formula for X_u, the speed-damping derivative, is as follows:

$$X_u = -\rho A_b (\Omega R)^2 \cdot \frac{\partial CH/\sigma}{\partial a_1} \frac{\partial a_1}{\partial u} \tag{2.8}$$

As discussed in Ref. 11, the linearized equations can be solved and reformulated for accelerations as given in the following equations:

$$\dot{u} = X_u u + X_w w + \left(X_q - W_0\right) q - g\theta + X_v v + X_p p + X_r r + X_{\delta_{col}} \delta_{col} + X_{\delta_{lon}} \delta_{lon} + X_{\delta_{lat}} \delta_{lat} + X_{\delta_{ped}} \delta_{ped} \tag{2.9}$$

$$\dot{v} = Y_u u + Y_w w + Y_q q + Y_v v + Y_p p + g\phi + \left(Y_r - U_0\right) r + Y_{\delta_{col}} \delta_{col} + Y_{\delta_{lon}} \delta_{lon} + Y_{\delta_{lat}} \delta_{lat} + Y_{\delta_{ped}} \delta_{ped} \tag{2.10}$$

$$\dot{w} = Z_u u + Z_w w + \left(U_0 + Z_q\right) q - g\theta_0 + Z_r r + Z_{\delta_{col}} \delta_{col} + Z_{\delta_{lon}} \delta_{lon} + Z_{\delta_{ped}} \delta_{ped} \tag{2.11}$$

$$\dot{p} = L_u u + L_w w + L_q q + L_v v + L_p p + L_r r + L_{\delta_{col}} \delta_{col} + L_{\delta_{lat}} \delta_{lat} + L_{\delta_{lon}} \delta_{lon} + L_{\delta_{ped}} \delta_{ped} \tag{2.12}$$

$$\dot{q} = M_u u + M_w w + M_q q + M_v v + M_p p + M_r r + M_{\delta_{col}} \delta_{col} + M_{\delta_{lon}} \delta_{lon} + M_{\delta_{lat}} \delta_{lat} \tag{2.13}$$

$$\dot{r} = N_u u + N_w w + N_v v + N_p p + N_r r + N_{col} \delta_{col} + N_{\delta_{lat}} \delta_{lat} + N_{ped} \delta_{ped} \tag{2.14}$$

2.2 Main Rotor

The main rotor is the primary source of the forces and moments on the helicopter. It is responsible for producing lift and propulsive forces as well as control moments. Being a rotating system, the rotor is a very complex dynamic system, and poses a big challenge in dynamics analysis. Unlike high disk loading propellers, the rotor is more flexible, which results in substantial motion of the rotor blades in response to the aerodynamic forces. This motion can produce high stresses within the blades or large moments at the root, which are transmitted through the hub to the helicopter. To reduce these loads, the rotor blades are usually designed with hinges at the root. The hinges allow free motion of the blade normal to (flapping) and in the plane of the disk (lag). Three different rotor hub designs have been used to allow the flapping and the lag motions. These are articulated, teetering, and hingeless rotor systems as shown in Figure 7[3,20]. All of these designs have been used successfully, and have both

advantages and disadvantages. Detailed discussion on these three rotor systems can be found in Refs. 3 and 20.

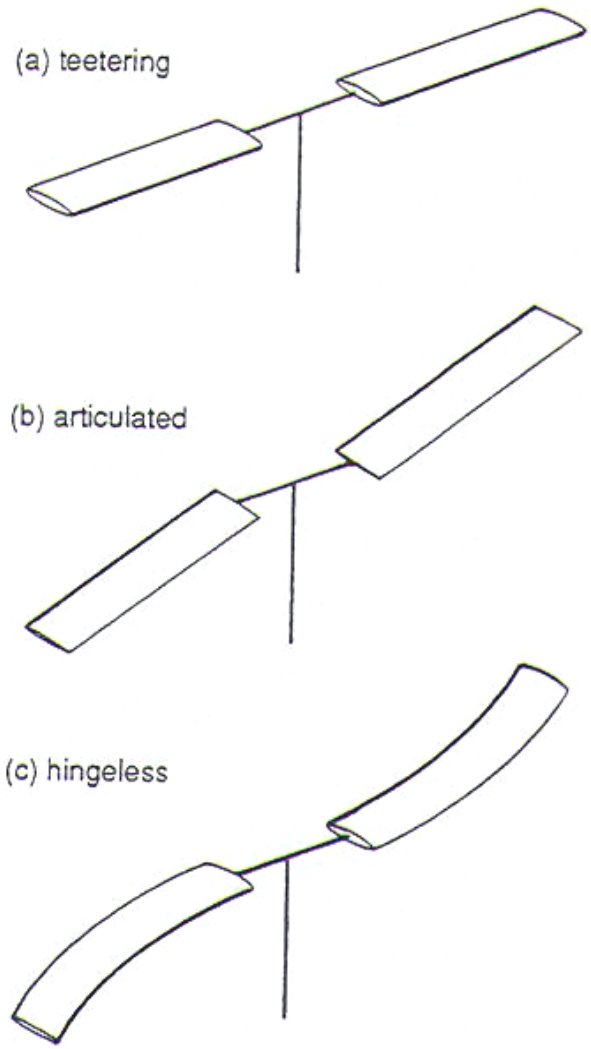

Figure 7: Three Flapping Arrangements

2.2.1 Rotor Flapping Motion

Rotor flapping motion is an out-of-plane motion of the rotor blades with respect to the rotor disk that results from the lateral aerodynamic moment caused by the

dissymmetry of the lift in the advancing and the retreating sides of the blades. The flapping motion takes place at the flapping hinges in articulated rotors. In hingeless rotors, the flapping motion is made possible by the flexibility of the rotor material as discussed in Ref 20. The flapping motion introduces inertial and aerodynamic forces. Also, motion about the flapping hinge is restrained by a centrifugal force when the blade is rotating. The flapping equation of motion of the rotor thus relates inertial, centrifugal, and aerodynamic forces acting on the flapping hinge as given below:

$$\ddot{\beta} + \Omega^2 \beta = \frac{1}{I_b} \int_0^R r F_{zz} dr = \gamma M_F \tag{2.15}$$

where

$$I_b = \int_0^R r^2 m dr \text{ and } \gamma = \frac{\rho a c R^4}{I_b}. \tag{2.16}$$

In equation 2.15, the left-hand side represents a mass spring system with a natural frequency equal to Ω or higher depending on the rotor head design. The right hand side is the aerodynamic forcing moment, which results from the flap moments due to angle-of-attack changes produced by the blade pitch, twist, inflow, flapping velocity, and flapping displacements.

Equation 2.15 represents the flapping equation for an articulated rotor system. For an articulated rotor with a hinge spring at the flapping hinge that produces a restoring moment on the blade as shown in Figure 8[3], the flapping equation becomes:

$$\ddot{\beta} + \nu^2 \beta = \left(\nu^2 - 1\right) \beta_p + \gamma \int_0^1 r \frac{F_{zz}}{ac} dr \tag{2.17}$$

where

$$\nu^2 = 1 + \frac{K_\beta}{I_b \Omega^2} \tag{2.18}$$

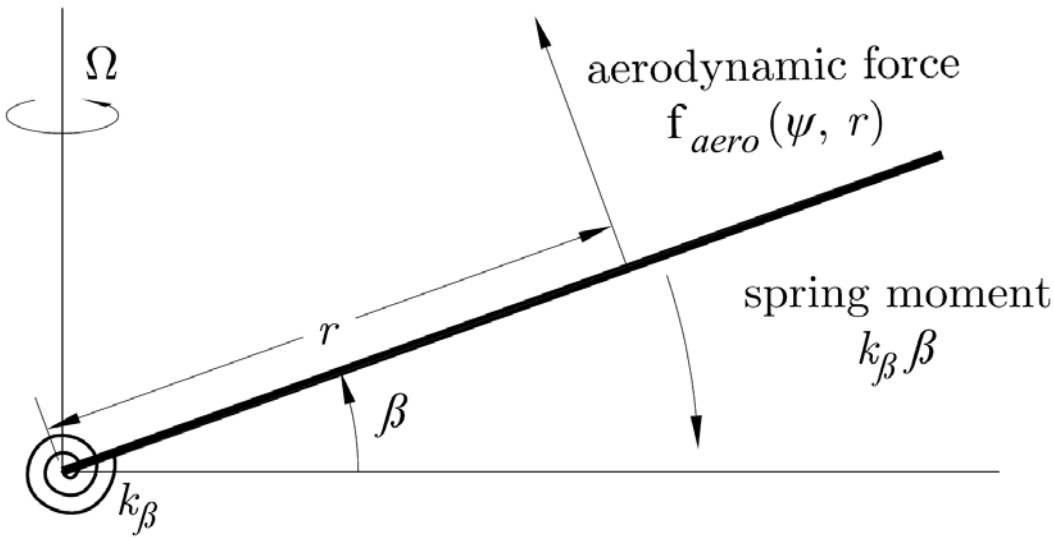

Figure 8: Blade Flapping Motion with a Hinge Spring

In the equation 2.17, ν is the dimensionless natural frequency of the flapping motion in the rotating frame and β_p is the pre-cone angle, which biases the hinge moment to zero for $\beta = \beta_p$.

For an articulated rotor with flap hinge offset (Figure 9[3]), the flapping equation is given by the following equation:

$$\ddot{\beta} + \nu^2 \beta = \frac{K_\beta \eta(1)}{I_b \Omega^2 (1-e)} \beta_p + \gamma \int_e^1 \eta \frac{F_{zz}}{ac} dr \tag{2.19}$$

where

$$\eta = \begin{cases} k(r-e) & r > e \\ 0 & r < e \end{cases} \tag{2.20}$$

is a mode shape, k is a constant determined by the mode shape normalization, and e is the hinge offset. The normalization used requires that the mode shape be equal to unity at the blade tip: $\eta(1) = 1$. Thus, $k = (1-e)^{-1}$, and the mode shape is $\eta = (r-e)/(1-e)$. This reduces to $\eta = r$ for the case of no offset.

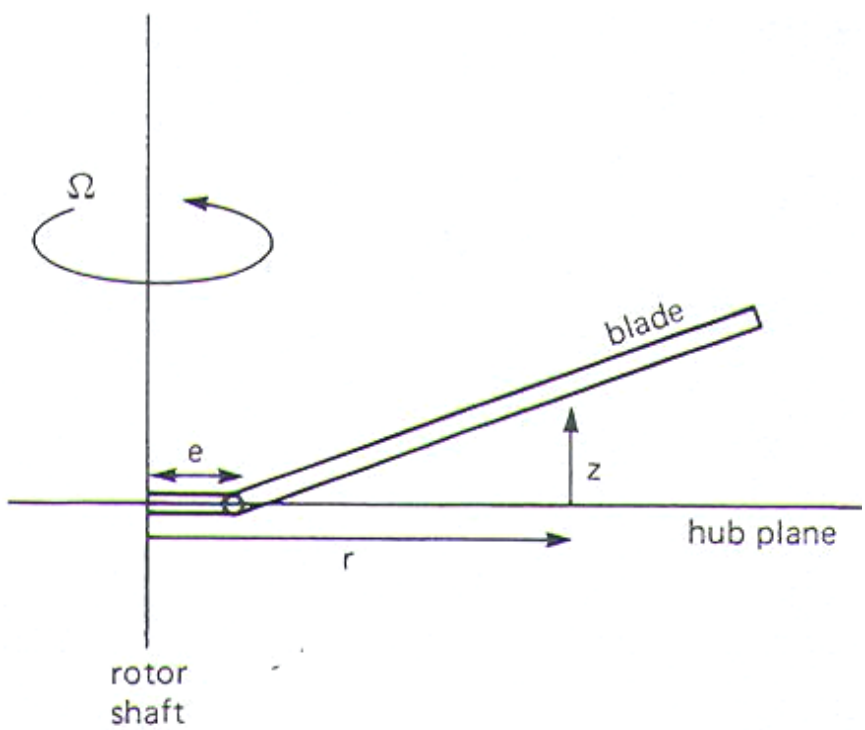

Figure 9: Flapping Motion with Hinge Offset

The natural frequency of the flap motion for the blade with hinge offset and spring is:

$$\nu^2 = 1 + \frac{e}{1-e}\frac{\eta(1)\int_e^1 \eta m dr}{\int_e^1 \eta^2 m dr} + \frac{K_\beta}{I_b \Omega^2 (1-e)} \tag{2.21}$$

In equation 2.21, the first term is the centrifugal spring, the second term is the hinge offset effect, and the third term is the hinge spring effect. For a uniform mass distribution and no hinge spring, the result is:

$$\nu^2 = 1 + \frac{3}{2}\frac{e}{1-e} \tag{2.22}$$

In hingeless rotors, which have no flap or lag hinges, the blades are attached to the hub with a cantilever root restraint. Such a rotor has the advantage of a mechanically simple hub and generally improved handling qualities. The flapping equation for the hingeless rotor is given by

$$\ddot{\beta} + \nu^2 \beta = \gamma \int_0^1 \eta \frac{F_{zz}}{ac} dr \tag{2.23}$$

The hingeless rotor is usually approximated using different models such as an offset hinge or a hinge spring as shown in Figure 10[3].

A gimbaled rotor has three or more blades attached to the hub without flap or lag hinges (cantilever root restraint), and the hub is attached to the rotor shaft by a universal joint or gimbal. The motion of the gimbaled hub relative to the shaft is described by two degrees-of-freedom, the longitudinal and lateral tilt angles β_{1_c} and

β_{1_s}, which corresponds to the tip-path plane tilt of an articulated rotor by cyclic flapping. The flapping equation of motion for the gimbaled rotor is given by the following equation:

$$\ddot{\beta} + \nu^2 \beta = \gamma \int_0^1 \eta \frac{F_{zz}}{ac} dr \tag{2.24}$$

where

$$\nu^2 = 1 + \frac{K_\beta}{\frac{1}{2} N I_b \Omega^2} \tag{2.25}$$

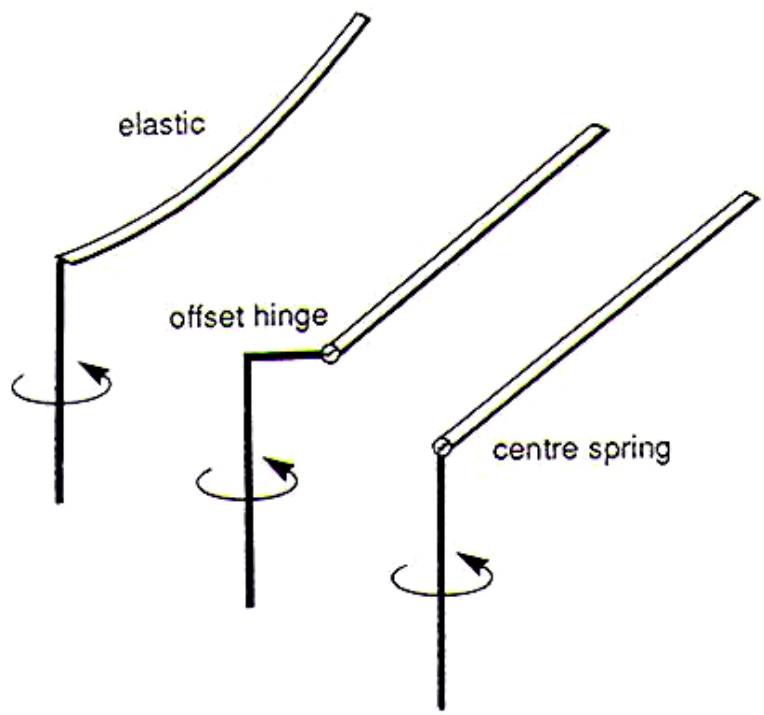

Figure 10: Different Approximate Models for a Hingeless Rotor Blade

Unless there is a hub spring, the frequency is $\nu = 1$ as for an articulated blade without hinge offset.

A teetering rotor has two blades attached to the hub without a flap or a lag hinge. The hub is attached to the shaft by a single flapping hinge, the two blades forming a single structure. The flapping motion is like that of a see-saw or a teeter board. Such a configuration is mechanically very simple. As for the gimbaled rotor, the coning motion gives no net moment about the teetering hinge, and in effect the blades have cantilever root restraint. The flapping equation of motion for the teetering rotor is as given below:

$$\ddot{\beta} + \nu^2 \beta = \gamma \int_0^1 r \frac{F_z}{ac} dr \tag{2.26}$$

where the natural frequency of flapping is:

$$\nu^2 = 1 + \frac{K_\beta}{\frac{1}{2} I_b \Omega^2} \tag{2.27}$$

Usually, a teetering rotor does not have a hub spring, so $\nu = 1$. The tip-path-plane tilt motion of the teetering rotor is thus the same as that of an articulated rotor with no hinge offset.

A detailed discussion on the flapping motion of these kinds of rotors can be found in Refs. 3 and 20. For steady-state conditions, the flapping motion is periodic. Therefore, the general solution to the flapping equation can be represented by an infinite Fourier series. However, all the terms above the first harmonic are not significant and are neglected, retaining the first three terms as given in the equation 2.28.

$$\beta = a_o + a_1 \cos\psi + b_1 \sin\psi \tag{2.28}$$

This representation of the blade flapping motion defines the rotor tip-path-plane (TPP) equation in which a_o represents the blade coning mode while a_1 and b_1 describe the tilting of the rotor tip-path-plane in the longitudinal and lateral directions respectively, as shown in Figure 11[20].

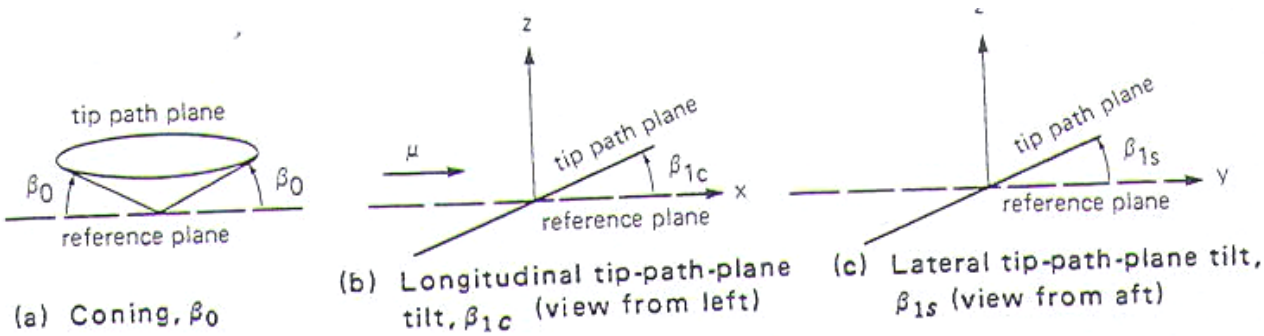

Figure 11: Interpretation of the Blade Flapping Harmonics

The flapping equations used in the present model come from the work by Chen in Ref. 62. In this reference, the author has developed flapping equations that are the most suitable to use in the state-space formulation and are easy to couple with rigid body dynamics. The second order flapping dynamics are represented by the following equation:

$$\ddot{\beta} + D\dot{\beta} + K\beta = f \tag{2.29}$$

where $\beta = \begin{bmatrix} a_0 & a_1 & a_2 \end{bmatrix}'$

The coefficients D, K, and f are functions of the rotor speed, the Lock number, the advance ratio, et cetera, and are as given below:

$$D = \Omega \begin{bmatrix} \frac{\gamma}{8} & 0 & -\frac{\gamma}{12}\mu \\ 0 & \frac{\gamma}{8} & 2 \\ -\frac{\gamma}{6}\mu & -2 & \frac{\gamma}{8} \end{bmatrix} \tag{2.30}$$

$$K = \Omega \begin{bmatrix} P^2 & 0 & 0 \\ -\frac{\gamma}{6}\mu & P^2 - 1 & \frac{\gamma}{8}\left(1 + \frac{\mu^2}{2}\right) \\ 0 & -\frac{\gamma}{8}\left(1 - \frac{\mu^2}{2}\right) & P^2 - 1 \end{bmatrix} \tag{2.31}$$

$$f = \Omega^2 \begin{bmatrix} \frac{\gamma}{8} + \frac{\mu^2}{4} & \frac{\gamma}{10} + \frac{\mu^2}{6} & 0 & -\frac{\gamma\mu}{6} \\ 0 & 0 & \frac{\gamma}{8}\left(1 + \mu^2\right) & 0 \\ -\frac{\gamma\mu}{3} & -\frac{\gamma\mu}{4} & \frac{\gamma}{8}\left(1 + 3\mu^2\right) & 0 \end{bmatrix} \begin{bmatrix} \theta_{0_M} \\ \theta_{0_T} \\ \theta_{1_s} \\ \theta_{1_c} \end{bmatrix} +$$

$$\Omega^2 \begin{bmatrix} \frac{\gamma\mu}{12} & 0 \\ -\frac{2}{\Omega} & -\frac{\gamma}{8\Omega} \\ -\frac{\gamma}{8\Omega} & \frac{2}{\Omega} \end{bmatrix} \begin{bmatrix} p \\ q \end{bmatrix} \tag{2.32}$$

where

$$P^2 = 1 + \frac{K_\beta}{I_b \Omega^2} \tag{2.33}$$

This formulation has been used most widely in helicopter dynamics modeling.

In equation 2.29, coning and differential coning with damping $\frac{\gamma}{8}$ and natural frequency λ_β are the independent and uncoupled degrees of freedom. The cyclic mode equations are coupled, the eigenvalues of which represent two flap modes: regressive and progressive flap modes that are at frequencies of $\lambda_\beta - 1$ and $\lambda_\beta + 1$ respectively[3]. The progressive flap mode is at a higher frequency and does not couple with the fuselage motions. The regressive flap mode can be of the same order as the highest frequency fuselage modes. Therefore, the present work uses a first order approximation of the lateral and the longitudinal flapping equations only to account for the regressive flapping dynamics as given in the following equations:

$$\dot{a}_1 = \frac{1}{\tau_f}\left(-a_1\left(1+\frac{\mu^2}{2}\right) - \tau_f q + \frac{p}{\Omega} + M_{f_{b_1}} b_1 + M_{f_{\delta_{lon}}} \delta_{lon}\left(1+3\mu^2\right) + \right.$$
$$\left. M_{f_{\delta_{lat}}} \delta_{lat} + M_{f_{a_{1_s}}} a_{1_s}\left(1+3\mu^2\right) + \lambda_{1_c}\right) \tag{2.34}$$

$$\dot{b}_1 = \frac{1}{\tau_f}\left(-b_1\left(1+\frac{\mu^2}{2}\right) - \tau_f p - \frac{q}{\Omega} + L_{f_{a_1}} a_1 + L_{f_{\delta_{lon}}} \delta_{lon} + \right.$$
$$\left. L_{f_{\delta_{lat}}} \delta_{lat}\left(1+\mu^2\right) + L_{f_{b_{1_s}}} b_{1_s}\left(1+\mu^2\right) + \lambda_{1_s}\right) \tag{2.35}$$

where $\tau_f = \frac{16}{\gamma\Omega}$ is the main rotor time constant.

Terms such as $M_{f_{\delta_{lon}}}$, $L_{f_{\delta_{lat}}}$, et cetera, represent the mechanical gearing between the swashplate, the rotor, and the stabilizer bar and are calculated using the

helicopter's geometry[56].

2.2.2 Rotor Lead-Lag Motion

The rotor lead-lag produces a blade motion in the disk plane. The lagging is defined to be positive when moving in the opposite direction of the rotation of the rotor. The lag motion is the result of the flapping motion that introduces aerodynamic and the inertial forces, particularly Coriolis forces, in the plane of the rotor disk. Articulated rotors have lag hinges to alleviate the chord-wise root loads by allowing an in-plane motion of the blades, while the structural flexibility provides this capability in the hingeless rotors.

The rigid body rotation about the lag hinge is represented by the lag-degree-of-freedom ζ. The forces acting on the lag hinge are inertial forces that oppose the lag motion; a centrifugal force directed radially outward from the center of the rotation, an aerodynamic force in the drag direction, and a Coriolis force in the same direction as the inertial force. A detailed discussion about the lag motion can be found in Ref. 20. Equilibrium of the moments about the lag hinge (Figure 12[20]), including a spring moment $K_\zeta \zeta$, gives the equation of motion. As discussed in Ref. 20, the differential equation for the blade lag motion is:

$$\ddot{\zeta} + \nu_\zeta^2 \zeta + 2\beta\dot{\beta} = \gamma \int_e^1 \eta \frac{F_x}{ac} dr \tag{2.36}$$

where e is the hinge offset, ν_ζ is the lag frequency ratio, and η is the mode shape of

the fundamental lag mode.

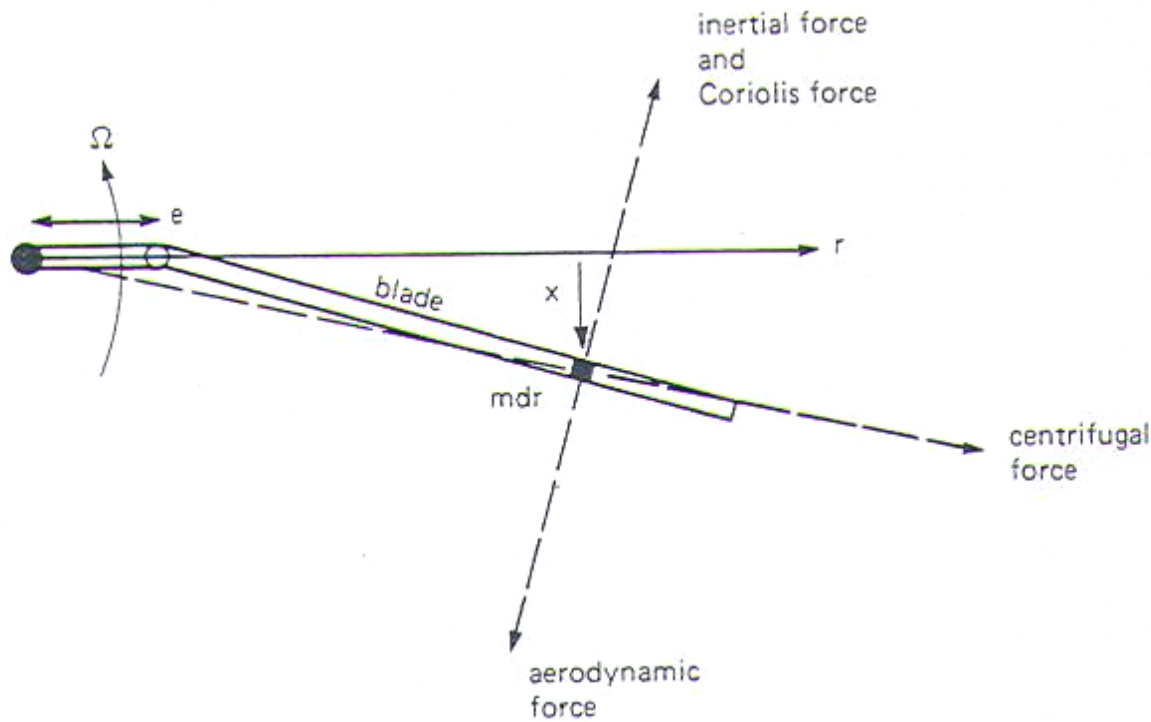

Figure 12: Rotor Blade Lag Moments

The lag dynamics are described by a mass and spring system excited by the in-plane aerodynamic forces and a Coriolis force due to the blade flapping. The aerodynamic forces damp the lag motion but much less effectively than the out-of-plane motion. Articulated rotors usually have a mechanical lag damper. The natural frequency of the lag motion is:

$$\nu_\zeta{}^2 = \frac{e}{1-e}\frac{\int_e^1 \eta m dr}{\int_e^1 \eta^2 m dr} + \frac{K_\zeta}{I_b \Omega^2 (1-e)} \tag{2.37}$$

The first term is the centrifugal spring term on the lag motion and it is zero if there is no hinge offset. For a uniform mass distribution and no hinge spring, the result is simply:

$$\nu_\zeta{}^2 = \frac{3}{2}\frac{e}{1-e} \tag{2.38}$$

Articulated rotors typically have a lag frequency of $\upsilon_\zeta =$ 0.2 to 0.3/rev. With hingeless rotors, a higher lag frequency can be attained. Since the lag frequency must not be too near 1/rev to avoid excessive blade loads, hingeless rotors naturally fall into two classes: soft-in-plane rotors, for which the lag frequency is below 1/rev (typically $\upsilon_\zeta = 0.65$ to 0.80/rev), and stiff in-plane rotors, for which the lag frequency is above 1/rev (typically $\upsilon_\zeta = 1.4$ to 1.6/rev). Gimballed and teetering rotors also fall into the stiff in-plane class. The soft in-plane rotors exhibit a mechanical instability called ground resonance if the lag frequency or the lag damping is too low. For this reason, an articulated rotor and some soft in-plane hingeless rotors must have mechanical dampers.

Similar to the flapping motion, the steady-state lag motion is described by a Fourier series:

$$\zeta = \zeta_0 + \zeta_{1_c}\cos\psi + \zeta_{1_s}\sin\psi + \ldots\ldots\ldots \tag{2.39}$$

where ζ_0 is the mean lag angle of the blades relative to the rotor hub and shaft. The first-harmonic cyclic lags ζ_{1_c} and ζ_{1_s} produce a lateral and longitudinal shift of the blades respectively as shown in Figure 13[20]. The higher order harmonics are usually

neglected in the dynamics analysis.

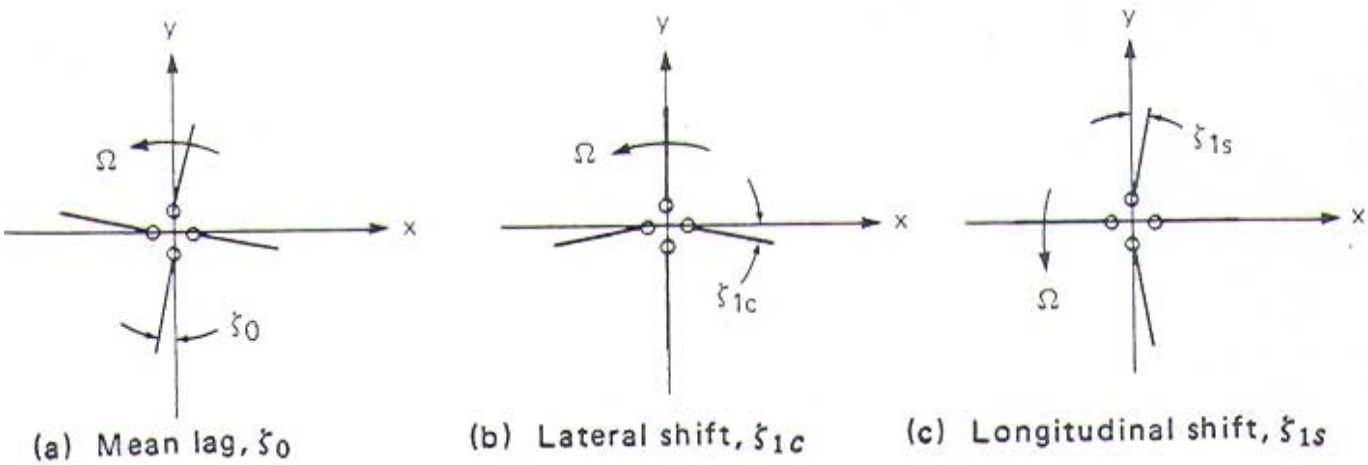

Figure 13: Interpretation of Blade Lag Harmonics

Compared to the flapping dynamics, the lead-lag dynamics are much more complicated. The flapping motion produces in-plane inertial forces that couple the flap and the lag degrees-of-freedom of the blade. Also, for low inflow rotors, the in-plane forces on the blade are small compared to the out-of-plane forces, and consequently more care is required in analyzing the motion resulting from the lag moment balance. No accurate simplification exists that is easy to use with a state-space formulation. However, several approximations have been tried. Refs. 31, 34, 41, and 47 discuss the approximations used previously for the lead-lag dynamics.

2.2.3 Blade Feathering Motion

The blade feathering, or pitching motion, is produced by the rotation of the blade about a hinge, or bearing, at the root, with its axis parallel to the blade spar. The pitching is defined to be positive for a nose-up rotation of the blade. The Fourier

series representation for the blade pitch motion is:

$$\theta = \theta_0 + \theta_{1_c} \cos\psi + \theta_{1_s} \sin\psi + ... \tag{2.40}$$

where θ_0 is the average blade pitch, while the first harmonics give a once-per-revolution variation of the pitch angle.

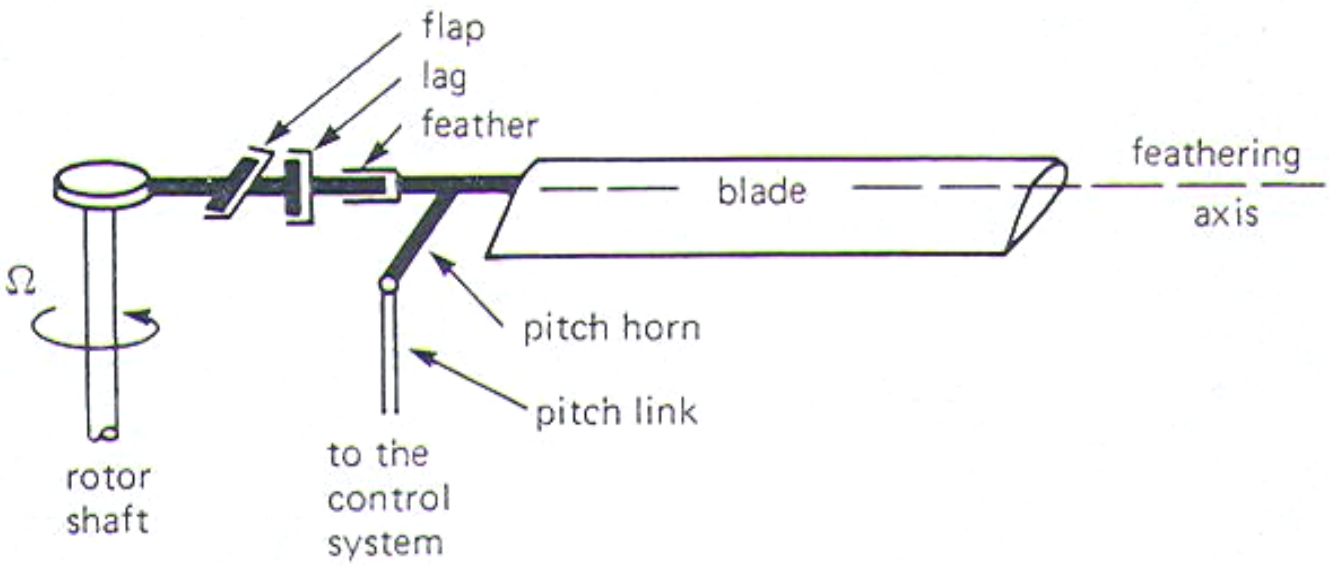

Figure 14: Schematic of the Flap and Lag Hinges, and the Pitch Bearing at the Hub of an Articulated Rotor

Figure 14[3,20] shows the flapping, the lead-lag, and the feathering hinge of an articulated rotor, while Figure 15 and Figure 16[3,20] show the basic blade motions.

The blade pitch or feathering motion has two sources. First, there is an elastic deformation of the control system and the blade, described by the dynamic degrees-of-freedom. Such motion is determined by the conditions for equilibrium of feathering moments on the blade, which give the equation of motion. The second source of the blade pitch is the commanded input from the helicopter control system.

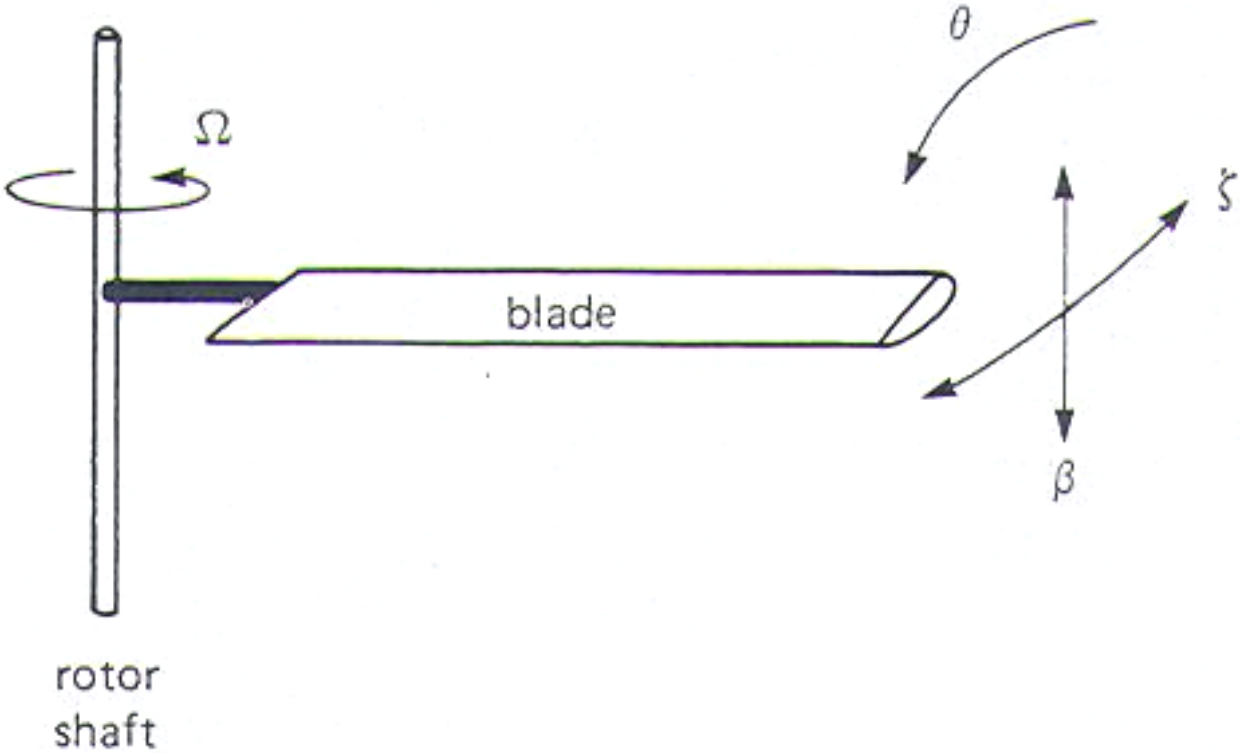

Figure 15: Fundamental Blade Motion

It is by commanding the rotor blade pitch that the pilot controls the helicopter. The feathering moments on the blade are low, and the lift changes due to pitch are large because the angle of attack is directly changed. The control inputs usually consist of just the mean and first harmonics. The mean angle θ_0 is called the collective pitch, and the 1/rev harmonics θ_{1_c} and θ_{1_s} are called the cyclic pitch angles. Basically, the collective pitch controls the average blade force, and hence the rotor thrust magnitude, while the cyclic pitch controls the tip-path-plane tilt.

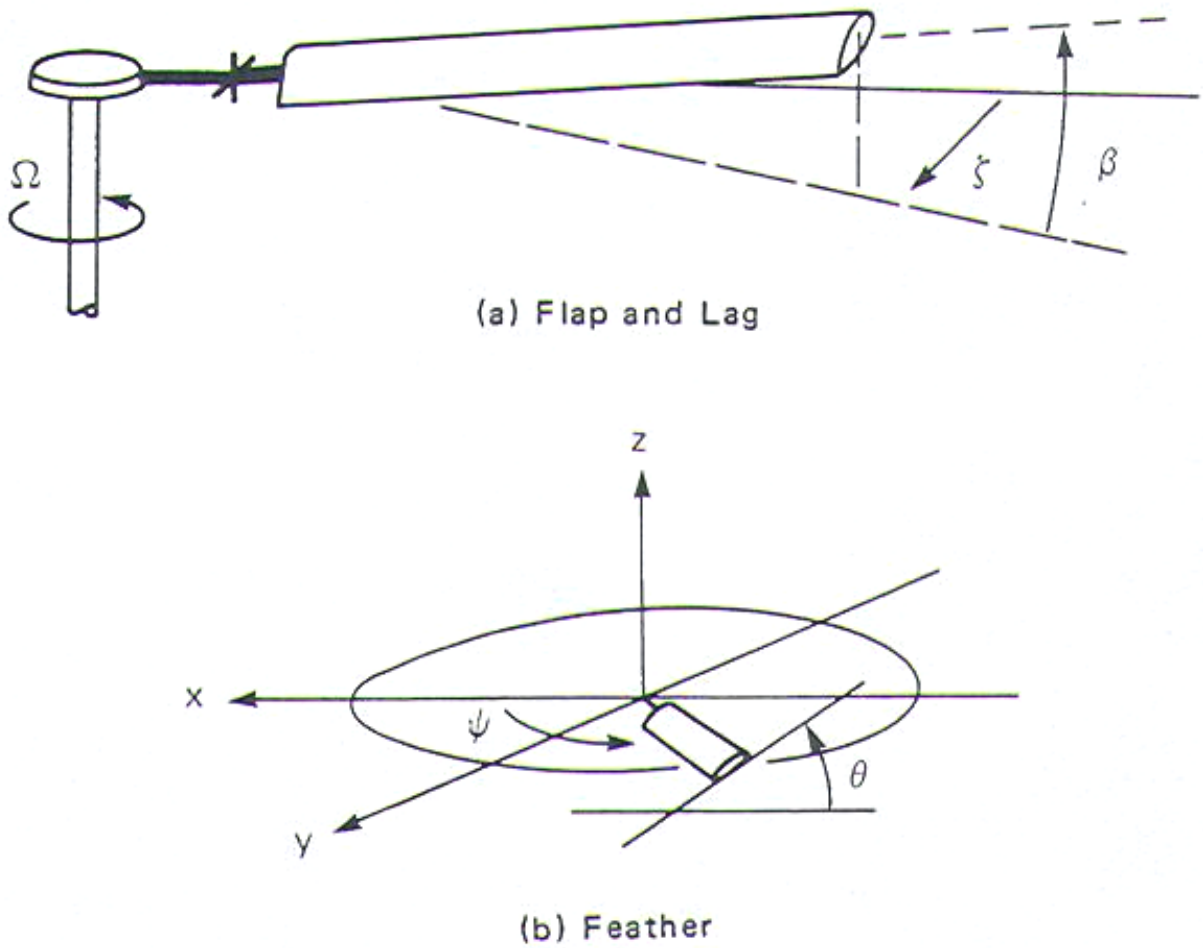

Figure 16: Basic Rotor Blade Motion

The blade pitch motion takes place about a pitch bearing or hinge. A pitch horn is rigidly attached to the pitch horn in such a way that the vertical motion of the link produces the blade pitch motion. A swashplate is most widely used to produce a steady and 1/rev sinusoidal vertical motion of the pitch link. A swashplate is a mechanical device that transmits the pilot's control motion in the non-rotating frame to the blade cyclic pitch motion in the rotating frame.

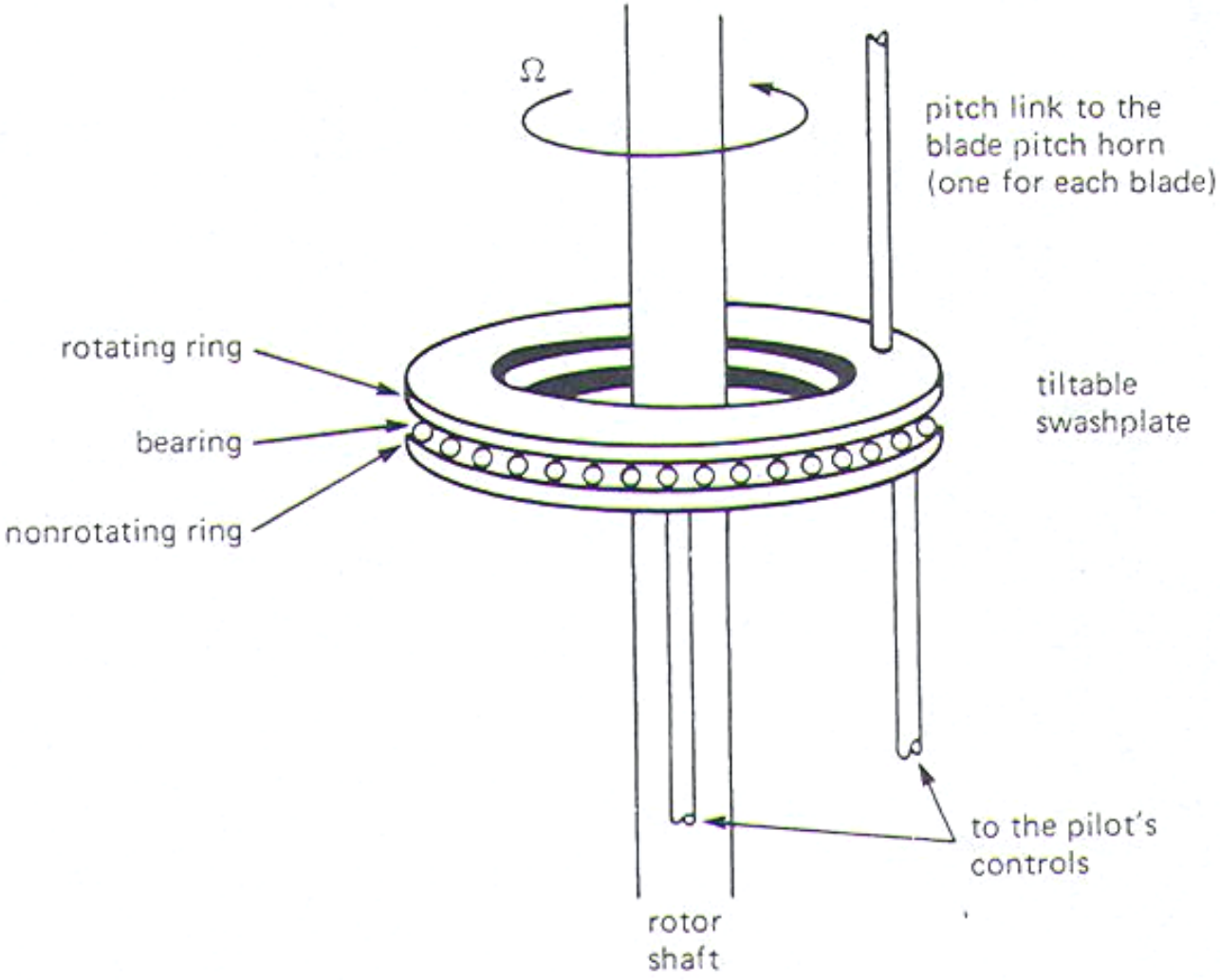

Figure 17: Schematic of the Rotor Swashplate

Figure 17 [3] is a schematic of the swashplate arrangement and defines the principal components that must be present in some form. The swashplate has rotating and non-rotating rings concentric with the shaft, with the bearings between the two rings. The rotating ring is gimbaled to the shaft in an arrangement that allows an arbitrary orientation of the plane of the swashplate relative to the rotor shaft, while one ring is

stationary and the other rotates. The blade pitch links attach to the rotating ring, and links from the pilot's controls attach to the stationary ring. Vertical displacement of the swashplate provides a vertical motion of the pitch links that is independent of azimuth, thereby changing the rotor collective pitch. A detailed discussion of the feathering motion can be found in Ref. 20.

2.2.4 Rotor Inflow Dynamics

The rotor inflow dynamics are the result of the wake-induced flow through the rotor. The induced flow results from the vortex system, which trails from each rotor blade. The vortex system is three-dimensional and results in the induced velocity components normal to and in the plane of the rotor. The rotor inflow is non-uniformly distributed across the rotor tip path plane and is also time dependent. The dynamics associated with the rotor inflow have similar time scales to the rotor dynamics and are strongly coupled with the flap and fuselage-degrees-of-freedom[31].

The inflow dynamics are governed by an infinite-dimensional (distributed parameter) system, which depends on both the aerodynamic loads and motion of the rotor. The inflow contributes to the local blade incidence and the dynamic pressure. The induced flow at the rotor consists of components due to the shed vorticity from all the blades, extending into the far wake of the aircraft. To take account of these effects fully, a complex vortex wake, distorted by itself and the aircraft, would need to be modeled. However, the normal component (i.e. the rotor-induced downwash) is the most important in the computation of the aerodynamic loads for flight dynamics

applications. A number of simplifying approximations to the rotor wake have been used for the flight dynamics application. Refs. 63 and 64 provide two comprehensive reviews of the rotor inflow, which deal with both the quasi-static and the dynamic effects. Ref. 3 and 20 discuss in detail the rotor inflow. Figure 18[3] illustrates the rotor flow states in axial motion.

The inflow in the hovering flight condition is given by the following equation (Ref. 3, 11, 20):

$$\lambda_{ih} = \frac{v_i}{\Omega R} \tag{2.41}$$

where $v_i = \sqrt{\frac{T}{2\rho A}}$ is the hover-induced velocity.

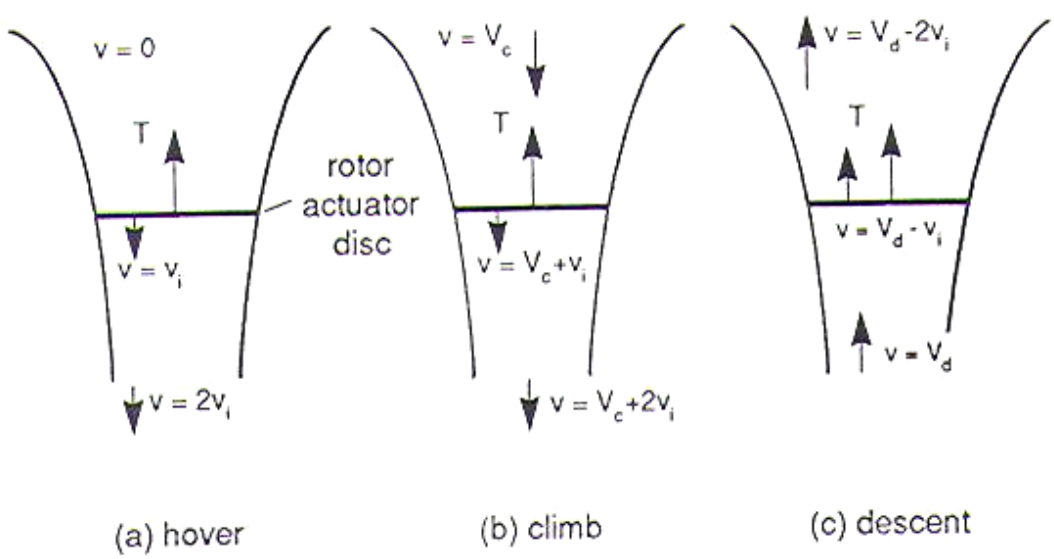

Figure 18: Rotor States in Axial Motion

For a climb, the inflow is given by the following equation:

$$\lambda_{ic} = -\frac{\mu_c}{2} + \sqrt{\left[\frac{\mu_c}{2} + \lambda_{ih}{}^2\right]} \tag{2.42}$$

where

$$\mu_c = \frac{V_c}{\Omega R} \tag{2.43}$$

Similarly, for descent, the inflow is:

$$\lambda_{id} = \frac{\mu_d}{2} + \sqrt{\left[\frac{\mu_d}{2} - \lambda_{ih}{}^2\right]} \tag{2.44}$$

where

$$\mu_d = \frac{V_d}{\Omega R} \tag{2.45}$$

In the high speed flight, the downwash field of a rotor is similar to that of a fixed wing aircraft with circular planform and momentum approximations for deriving the induced flow at the wing apply. Figure 19[3] shows a flow streamtube with freestream velocity V at an angle of incidence α to the disc. The induced velocity in the far wake is again twice the flow at the rotor. The induced velocity at the rotor is given by

$$\lambda_i = \frac{C_T}{2\sqrt{\left[\mu^2 + \left(\lambda_i - \mu_z\right)^2\right]}} \tag{2.46}$$

where

$$\mu = \frac{V\cos\alpha_d}{\Omega R} \text{ and } \mu_z = -\frac{V\sin\alpha_d}{\Omega R} \tag{2.47}$$

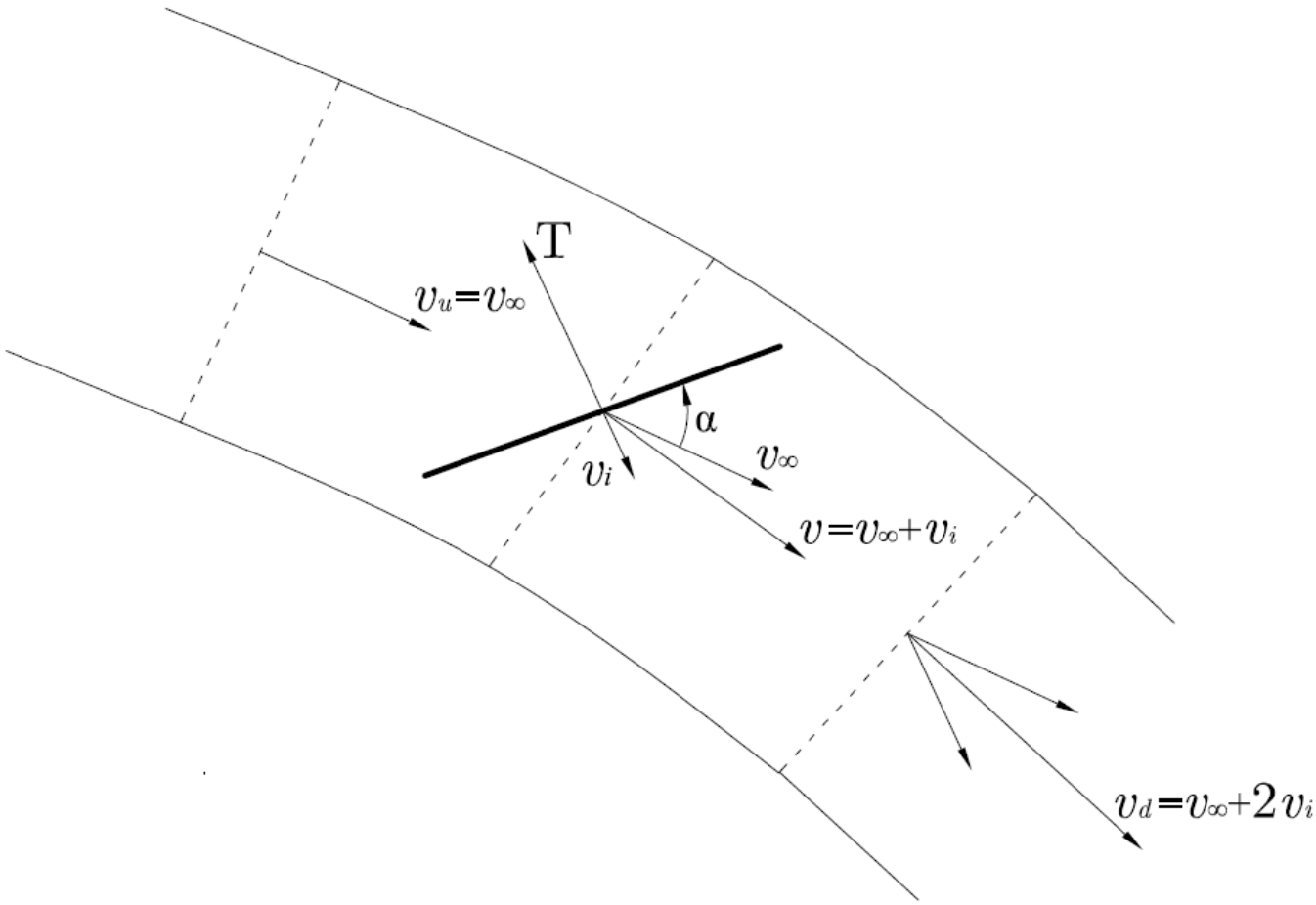

Figure 19: Flow Through a Rotor in Forward Flight

Between hover and μ values of about 0.1, the mean normal component of the rotor wake is still high, but now gives rise to fairly strong non-uniformities along the longitudinal, or more generally the flight axis, of the disc. Several approximations to this non-uniformity were derived in the early development of rotor aerodynamic theory, using the vortex form of the actuator disc theory. It was shown that a good approximation to the inflow could be achieved with a linear variation along the disc,

determined by the wake angle relative to the disc, given by:

$$\lambda_i = \lambda_0 + \frac{r_b}{R}\lambda_{1cw}\cos\psi_w \tag{2.48}$$

where

$$\lambda_{1cw} = \begin{cases} \lambda_0 \tan\left(\frac{\chi}{2}\right), & \chi < \frac{\pi}{2} \\ \lambda_0 \cot\left(\frac{\chi}{2}\right), & \chi > \frac{\pi}{2} \end{cases} \tag{2.49}$$

and the wake skew angle, χ is given by

$$\chi = \tan^{-1}\left(\frac{\mu}{\lambda_0 - \mu_z}\right) \tag{2.50}$$

where λ_0 is the uniform component of the inflow as given by the equation 2.46. Figure 20[3] shows the definition of the rotor angle of attack and the wake skew angle.

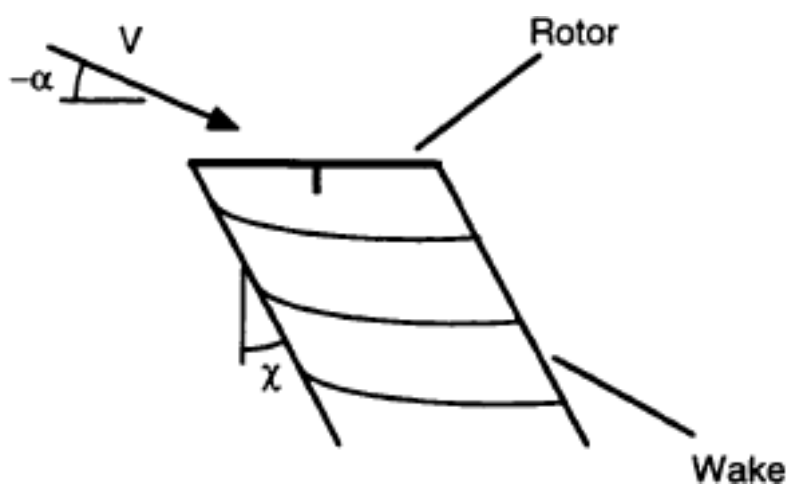

Figure 20: Definition of Rotor Angle of Attack and Wake Skew Angle

The momentum theory used to formulate the expressions for the rotor inflow is strictly applicable only in steady flight when the rotor is trimmed and the conditions are slowly varying. The effect of the inflow on the rotor thrust during maneuvers can be subsumed using the lift deficiency function as discussed in Ref. 20. When the rotor thrust changes, the inflow changes, increasing for increasing thrust and decreasing for decreasing thrust. Considering the thrust changes as perturbations on the mean component, we can write

$$\delta C_T = \delta C_{T_{QS}} + \left(\frac{\partial C_T}{\partial \lambda_i}\right)_{QS} \delta\lambda_i \tag{2.51}$$

where

$$\left(\frac{\partial C_T}{\partial \lambda_i}\right)_{QS} = -\frac{a\sigma}{4} \tag{2.52}$$

where the quasi-static thrust coefficient changes without a change in the inflow. Assuming that the inflow changes are due entirely to the thrust changes, we can write

$$\delta\lambda_i = \frac{\partial \lambda_i}{\partial C_T} \delta C_T \tag{2.53}$$

The derivatives of the inflow with the thrust have simple approximate forms at hover and forward flight as given below:

$$\frac{\partial \lambda_i}{\partial C_T} = \frac{1}{4\lambda} \quad \mu = 0 \tag{2.54}$$

$$\frac{\partial \lambda_i}{\partial C_T} \approx \frac{1}{2\lambda} \quad \mu > 0.2 \tag{2.55}$$

Combining these relationships, we can write the thrust changes as the product of a deficiency function and the quasi-steady thrust change, i.e.,

$$\delta C_T = C' \delta C_{T_{QS}} \tag{2.56}$$

where

$$C' = \begin{cases} \dfrac{1}{1+\dfrac{a\sigma}{16\lambda_i}}, & \mu = 0 \\ \\ \dfrac{1}{1+\dfrac{a\sigma}{8\mu}}, & \mu > 0.2 \end{cases} \tag{2.57}$$

Rotor thrust changes are, therefore, reduced to about 60-70% in hover and 80% in the mid-speed range due to the effects of the inflow.

The inflow derived using momentum theory is effective in predicting the gross and the slowly varying uniform and rectangular inflow components. In reality, the inflow distribution varies with the flight condition and the unsteady rotor loading in a much more complex manner. The inflow varies around the disc and along the blades, continuously satisfying the local flow balance conditions and conservation principles. Locally, the flow responds to the local changes in the blade loading. If there are one-per-rev rotor forces and moments, the inflow variation will be one-per-rev. The inflow also takes finite time to develop as the air mass is accelerated to its new velocity. Also, the rotor wake is far more complex and discrete than the uniform flow in a streamtube assumption of the momentum theory. The local blade-vortex

interactions can cause very large local perturbations in the blade inflow and hence the incidence. These can be sufficient to stall the blade in certain conditions and are important for predicting the rotor stall boundaries and the resulting flight dynamics at the flight envelope limits.

2.2.4.1 Dynamic Inflow

Figure 21[3] shows a rotor disc element. Assuming that the relationship between the change in the momentum and the work done by the load across the element applies locally as well as globally, the equations for the mass flow through the element and the thrust differential are given as below:

$$d\dot{m} = \rho V r_b dr_b d\psi \tag{2.58}$$

$$dT = d\dot{m} 2 v_i \tag{2.59}$$

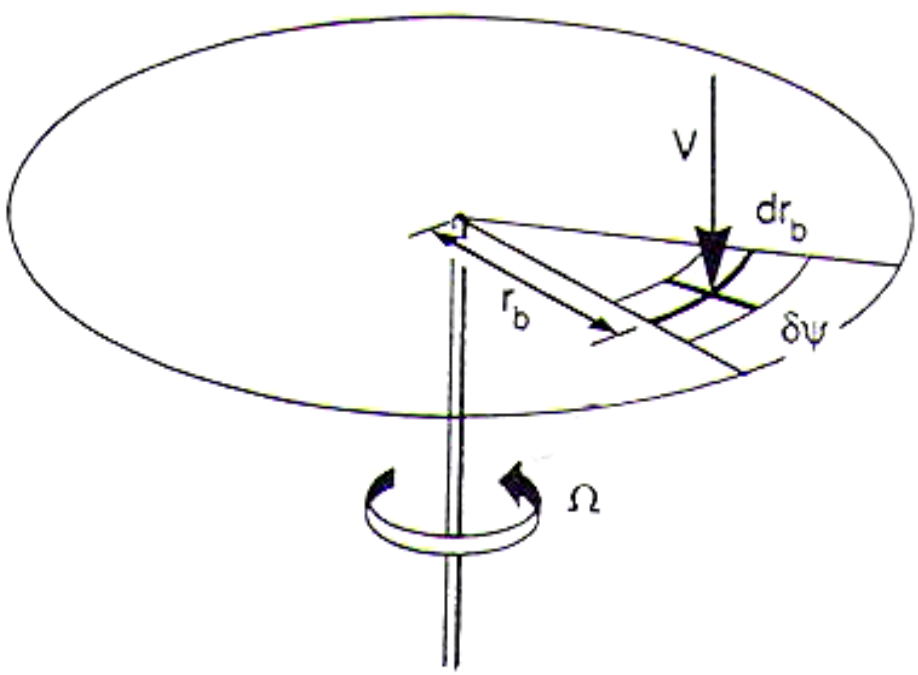

Figure 21: Local Momentum Theory Applied to a Rotor Disk

Using the two-dimensional blade element theory, these can be combined into the form[3]:

$$\frac{N_b}{2\pi}\left(\frac{1}{2}\rho ac\left(\theta\bar{U}_T{}^2+\bar{U}_T\bar{U}_P\right)dr_b d\psi\right)=2\rho r_b\left(\mu^2+\left(\lambda_i-\mu_z\right)^2\right)^{1/2}\lambda_i dr_b d\psi \quad (2.60)$$

Integrating around the disc and along the blades leads to the solution for the mean uniform component of the inflow. If the momentum balance is applied to the one-per-revolution components of the load and inflow, then the expressions for the non-uniform inflow can be derived. If first harmonic inflow is written in the form:

$$\lambda_i(r,\psi)=\lambda_o+\bar{r}_b\left(\lambda_{1c}\cos\psi+\lambda_{1s}\sin\psi\right) \quad (2.61)$$

then equation 2.60 can be expanded to give a first harmonic balance as

$$\lambda_{1c}=\frac{3a\sigma}{16}\frac{1}{\bar{V}}F_{1c} \quad (2.62)$$

and

$$\lambda_{1s}=\frac{3a\sigma}{16}\frac{1}{\bar{V}}F_{1s} \quad (2.63)$$

where

$$F_{1c}=\frac{\alpha_{1cw}}{3}-\mu\frac{\beta_0}{2} \quad (2.64)$$

and

$$F_{1s}=\frac{\alpha_{1sw}}{3}+\mu\left(\theta_0+\mu_z-\lambda_0+\frac{2}{3}\theta_{tw}\right) \quad (2.65)$$

are the normal or lift force components. These one-per-revolution lift forces are

closely related to the rolling and pitching moment at the hub in the non-rotating fuselage frame as given below:

$$F_{1s} = \frac{2C_{Ma}}{a\sigma} \tag{2.66}$$

$$F_{1c} = \frac{2C_{La}}{a\sigma} \tag{2.67}$$

These moments at the hub are functions of the non-uniform inflow distributions. Therefore, just as with the rotor thrust and the uniform inflow, these moments are reduced by a similar moment deficiency factor:

$$C_{La} = C_1' C_{LaQS} \tag{2.68}$$

$$C_{Ma} = C_1' C_{MaQS} \tag{2.69}$$

In hover, the first harmonic inflow components given by equations 2.62 and 2.63 are expanded as:

$$\lambda_{1c} = C_1' \frac{a\sigma}{16\lambda_0}\left(\theta_{1c} - \beta_{1s} + \overline{q}\right) \tag{2.70}$$

$$\lambda_{1s} = C_1' \frac{a\sigma}{16\lambda_0}\left(\theta_{1s} + \beta_{1c} + \overline{p}\right) \tag{2.71}$$

The inflow analysis outlined above has ignored any time dependency other than the quasi-steady effects and harmonic variations. In reality, there will always be a transient lag in the build-up or decay of the inflow field; in effect, the flow is a dynamic element. An extension of the momentum theory includes the dynamics of an

apparent mass[65]. The authors in the Ref. 65 suggested that the transient inflow could be taken into account by including an accelerated mass of air occupying 63.7% of the air mass of the circumscribed sphere of the rotor. The equation for the thrust including an apparent mass term is:

$$T = 0.637\rho\frac{4}{3}\pi R^3\dot{v}_i + 2A_d\rho v_i\left(V_c + v_i\right) \tag{2.72}$$

If we linearize the above equation about steady hover trim, we get

$$\lambda_i = \lambda_{itrim} + \delta\lambda_i \tag{2.73}$$

and

$$C_T = C_{T_{trim}} + \delta C_T \tag{2.74}$$

The perturbation equation takes the form:

$$\tau_\lambda\dot{\lambda}_i + \delta\lambda_i = \lambda C_T\delta C_T \tag{2.75}$$

where the time constant and steady-state inflow gain are given by

$$\tau_\lambda = \frac{0.849}{4\lambda_{i_{trim}}\Omega},\ \lambda C_T = \frac{1}{4\lambda_{i_{trim}}} \tag{2.76}$$

For typical rotors, moderately loaded in the hover, the time constant for the uniform inflow works out at about 0.1 second.

For the flight dynamics application, several dynamic inflow models have been tried. The inflow dynamics model that has been most widely used and has attracted the most attention within the flight dynamics community is the Pitt-Peters dynamic inflow model[66]. The Pitt-Peters dynamic inflow model expands the induced velocity

into a three term series as given below:

$$\lambda_i(r,\psi) = \lambda_o + \lambda_c \frac{r}{R}\cos\psi + \lambda_s \frac{r}{R}\sin\psi \tag{2.77}$$

The inflow states are related to the rotor thrust and moment coefficients through the following equations[67, 68]:

$$M_i \begin{bmatrix} \dot{\lambda}_o \\ \dot{\lambda}_c \\ \dot{\lambda}_s \end{bmatrix} + \left[L_i\right]^{-1} \begin{bmatrix} \lambda_o \\ \lambda_c \\ \lambda_s \end{bmatrix} = \begin{bmatrix} C_T \\ C_M \\ C_L \end{bmatrix} \tag{2.78}$$

where C_T, C_M, and C_L are the rotor thrust, pitching, and rolling moment coefficients and are discussed in chapter 3. L_i and M_i are the dynamic inflow static gain and apparent mass matrices and are given below for the hovering flight condition.

$$L_i = \frac{1}{v_h} \begin{bmatrix} \frac{1}{2} & 0 & 0 \\ 0 & -1 & 0 \\ 0 & 0 & -1 \end{bmatrix} \tag{2.79}$$

$$M_i = \frac{1}{v_h} \begin{bmatrix} \frac{8}{3\pi} & 0 & 0 \\ 0 & -\frac{16}{45\pi} & 0 \\ 0 & 0 & \frac{-16}{45\pi} \end{bmatrix} \tag{2.80}$$

2.2.4.2 Dynamic Wake Correction

As discussed earlier, traditional 6-DoF models predicted the off-axes responses in

the wrong direction. This has been a topic of research for the past three decades. Much effort has been expended in this area in order to correct the predicted off-axes responses. For a long time, the cause of this discrepancy was not understood. In Ref. 69, Takahashi developed a high-order nonlinear flight dynamics model for a UH-60 helicopter that included the flap and the lag degrees-of-freedom. The simulation showed a high correlation with the flight data for on-axes responses, but the model predicted an off-axis response in the wrong direction. Other works have shown similar results (Ref. 25, 70).

As discussed earlier, J. D. Keller introduced a dynamic wake correction factor to account for the effect of rotor pitching and rolling motion on the induced velocity distribution[49, 50]. He showed that due to steady pitching and rolling motion, there was a distortion in the wake as shown in Figure 22[49], and that neglecting this distortion was the source of the error in the off-axis response. With the introduction of dynamic wake correction factor into the induced velocity model, there was a significant improvement in the off-axis response. The inclusion of the dynamic wake correction factor in the induced velocity model is shown in the following equations:

$$M_i \begin{bmatrix} \dot{\lambda}_o \\ \dot{\lambda}_c \\ \dot{\lambda}_s \end{bmatrix} + \left[L_i\right]^{-1} \begin{bmatrix} \lambda_o \\ \lambda_c \\ \lambda_s \end{bmatrix} = \begin{bmatrix} C_T \\ C_M \\ C_L \end{bmatrix} + K_R \begin{bmatrix} 0 \\ \left(\dfrac{q}{\Omega}\right) \\ \left(\dfrac{p}{\Omega}\right) \end{bmatrix} \tag{2.81}$$

where K_R is the dynamic wake correction factor. The experimentally found value of

K_R is 1.5.

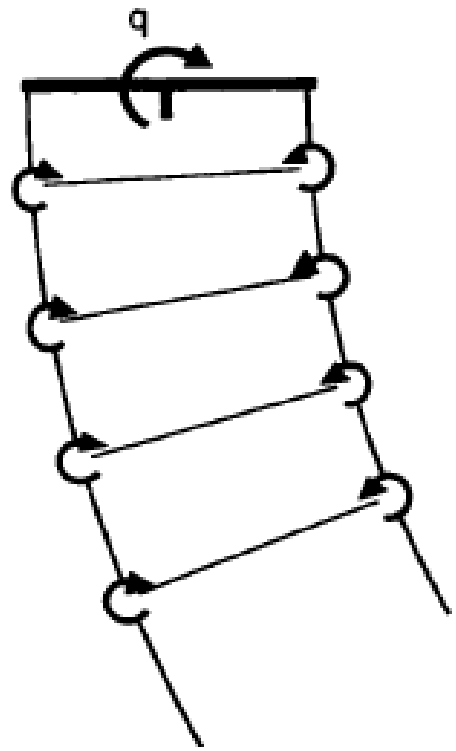

Figure 22: Wake Distortion Due to Steady Pitch Rate

2.3 Tail Rotor

The tail rotor of a single main rotor helicopter is a small diameter rotary wing with the function of balancing the main rotor torque and providing yaw control, which is achieved through the action of the tail rotor thrust on a longitudinal arm (usually longer than the main rotor radius) about the rotor shaft. The tail rotor is usually a flapping rotor with a low disk loading. An analysis similar to the main rotor analysis is applicable. However, the tail rotor has no cyclic pitch control, just collective to

control the thrust magnitude. Also, the tail rotor shaft angle is fixed by the geometry of the tail rotor installation and the helicopter yaw angle, instead of being determined by the conditions for force equilibrium of the rotor. The tail rotor drag or propulsive force is included in the airframe drag and is balanced by the main rotor.

The tail rotor operates within a complex flowfield, particularly in low speed flight, within ground effects, in sideways flight, and in the transition to forward flight. The wake of the main rotor, together with the disturbed air shed from the main rotor hub, rear fuselage, and vertical stabilizer, interact with the tail rotor to create a strongly non-uniform flowfield that can dominate the tail rotor and the control requirements. The current research neglects non-uniform effects and uses tail rotor forces and moments developed from simple physical considerations.

Figure 23[3] shows a tail rotor arrangement. The tail rotor side-force can be written in the form:

$$Y_T = \rho\left(\Omega_T R_T\right)^2 \sigma_T a_T \left(\pi R_T\right)^2 \left(\frac{C_{T_T}}{a_T \sigma_T}\right) \tag{2.82}$$

where

$$C_{T_T} = \frac{T_T}{\rho\left(\Omega_T R_T\right)^2 \left(\pi R_T\right)^2} \tag{2.83}$$

Apart from the effect of the tail rotor on the yaw dynamics, it has some effect on the lateral and vertical dynamics. The present work neglects the effect of the tail rotor on the vertical dynamics. However, the effect of the tail rotor on the lateral

dynamics is considered.

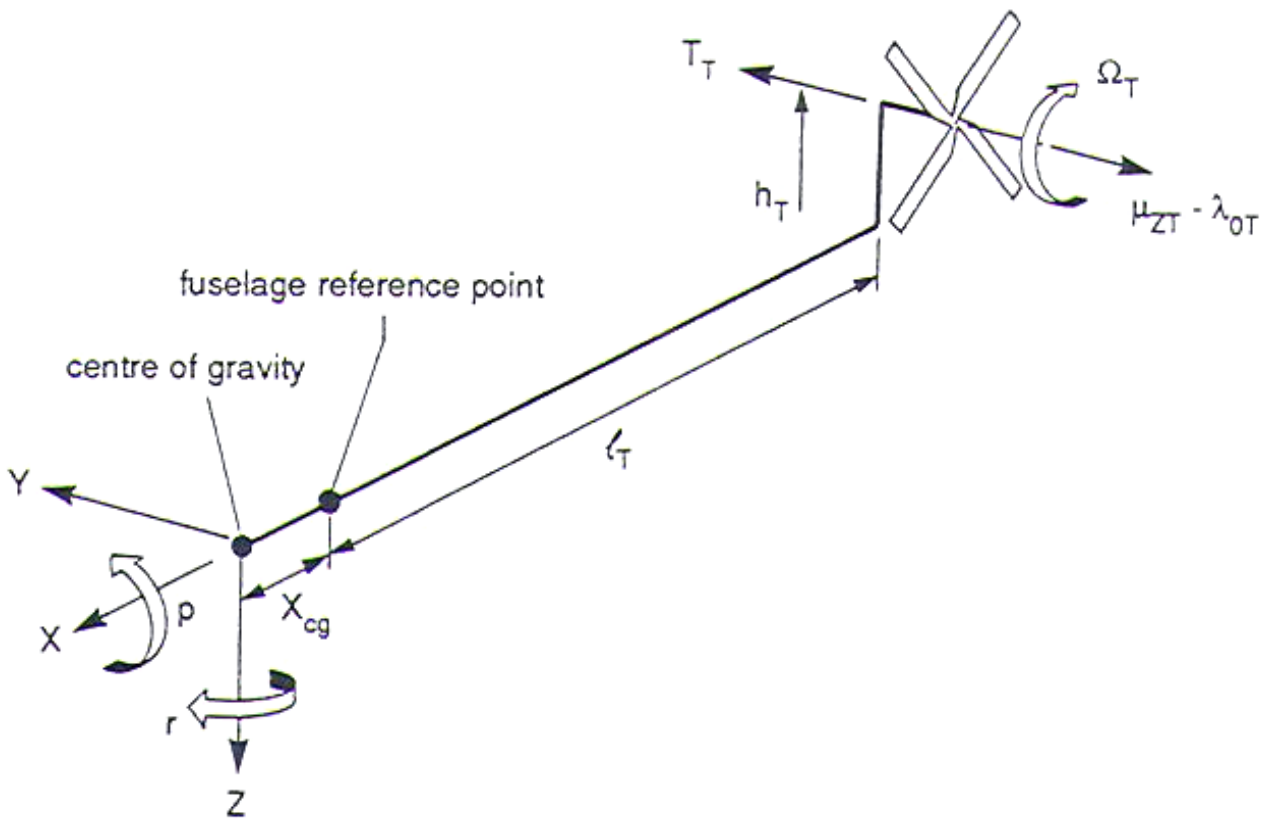

Figure 23: Sketch of the Tail Rotor Subsystem

2.4 Stabilizer Bar

The stabilizer bar is an essential part of small-scale UAV helicopters. These vehicles have higher sensitivity to control inputs than their full-scale counterparts. Without some form of stability augmentation, it is almost impossible for human pilots to control these vehicles. Various methods have been used to increase the stability of these model-scale helicopters. The stabilizer bar is one of the most widely used devices for the stability augmentation of these helicopters. The system consists of

flybars and paddles placed at 90° to the main rotor blades as shown in Figure 24. The bars are attached to the rotor shaft above the main rotor through an unrestrained teetering hinge.

Figure 24: Instrumented Raptor 50 Helicopter Showing Stabilizer Bar

The stabilizer bar acts as a lagged rate feedback in the pitch and roll axes. This reduces the bandwidth and control sensitivity to longitudinal inputs.

Using stabilizer bars, the cyclic commands do not go directly to the blades. Instead, the cyclic commands are applied to the flybar whose flapping motion determines the blade pitch angles [54, 55, 56]. The stabilizer bar receives cyclic inputs from the swashplate in a manner similar to that of the main rotor blades. The stabilizer bars do not receive any collective input, because the bars are not designed

to produce any thrust.

Figure 25[56] shows the schematic drawing in the plane of the Bell-Hiller mixing lever.

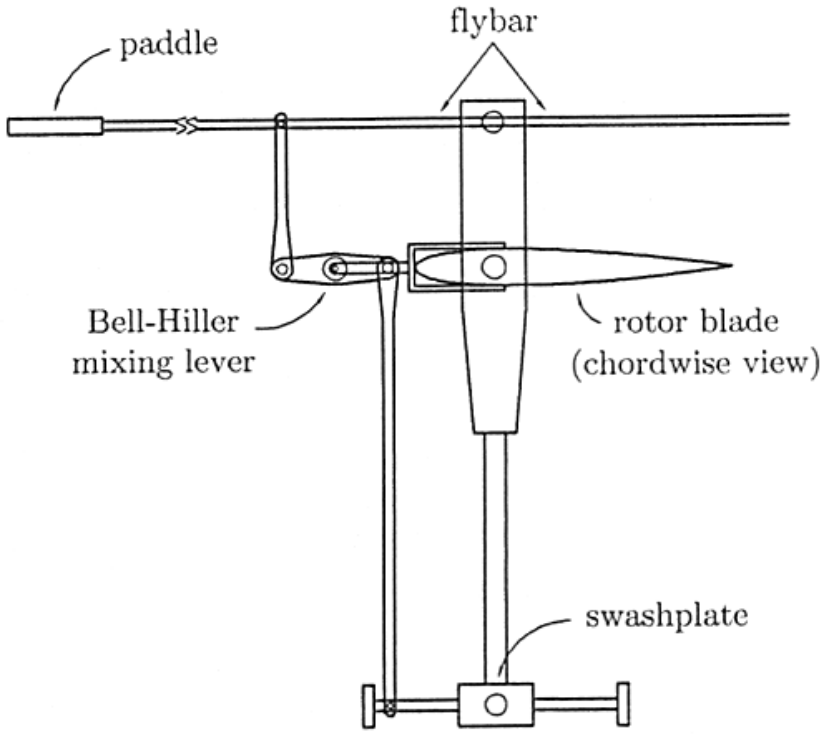

Figure 25: 2D View in the Plane of the Mixing Lever

The flapping motion of the stabilizer bar is periodic and is similar to that of the main rotor. The solution can again be expressed as a Fourier series as given in equation 2.28 for the main rotor. However, since it is a teetering rotor, it does not exhibit any coning mode as seen in the following equation:

$$\beta_s(\psi) = a_{1_s} \cos\psi + b_{1_s} \sin\psi \tag{2.84}$$

With this solution, the flapping equation of motion for the stabilizer bar is similar

to the main rotor flapping equation (Eq. 2.29) as given below:

$$\ddot{\beta}_s + D_s\dot{\beta}_s + K_s\beta_s = f_s \tag{2.85}$$

where the coefficients D_s, K_s, and f_s are similar to those for the main rotor and are taken from Ref. 62. Again, first order approximations to the flapping equations are used in this thesis, a simplified version of which are given below:

$$\dot{a}_{1_s} = \frac{1}{\tau_s}\left(-a_{1_s} - \tau_s q + M_{s_{\delta_{lon}}}\delta_{lon}\right) \tag{2.86}$$

$$\dot{b}_{1s} = \frac{1}{\tau_s}\left(-b_{1s} - \tau_s p + L_{s_{\delta_{lat}}}\delta_{lat}\right) \tag{2.87}$$

The stabilizer bar has a larger flapping time constant than the main rotor because the Lock number for the stabilizer bar is significantly less than that for the main rotor as given by the following equation:

$$\tau_s = \frac{16}{\gamma_s \Omega} \tag{2.88}$$

The Lock number represents the ratio of aerodynamic to centrifugal forces. It is given by the following expression:

$$\gamma = \frac{\rho a c R^4}{I_b} \tag{2.89}$$

The stabilizer bar is smaller in diameter than the main rotor. This results in lower Lock number for the stabilizer bar than for the main rotor.

The higher time constant of stabilizer bar results in slower response, which provides the stabilizing effect. With the stabilizer bar, the inputs to the main rotor are

augmented as follows:

$$\bar{\delta}_{lon} = \delta_{lon} + K_{a_{1_s}} a_{1_s} \tag{2.90}$$

$$\bar{\delta}_{lat} = \delta_{lat} + K_{b_{1_s}} b_{1_s} \tag{2.91}$$

The terms $K_{a_{1_s}}$ and $K_{b_{1_s}}$ represent the gearing of the stabilizer bar Bell-Hiller mixer.

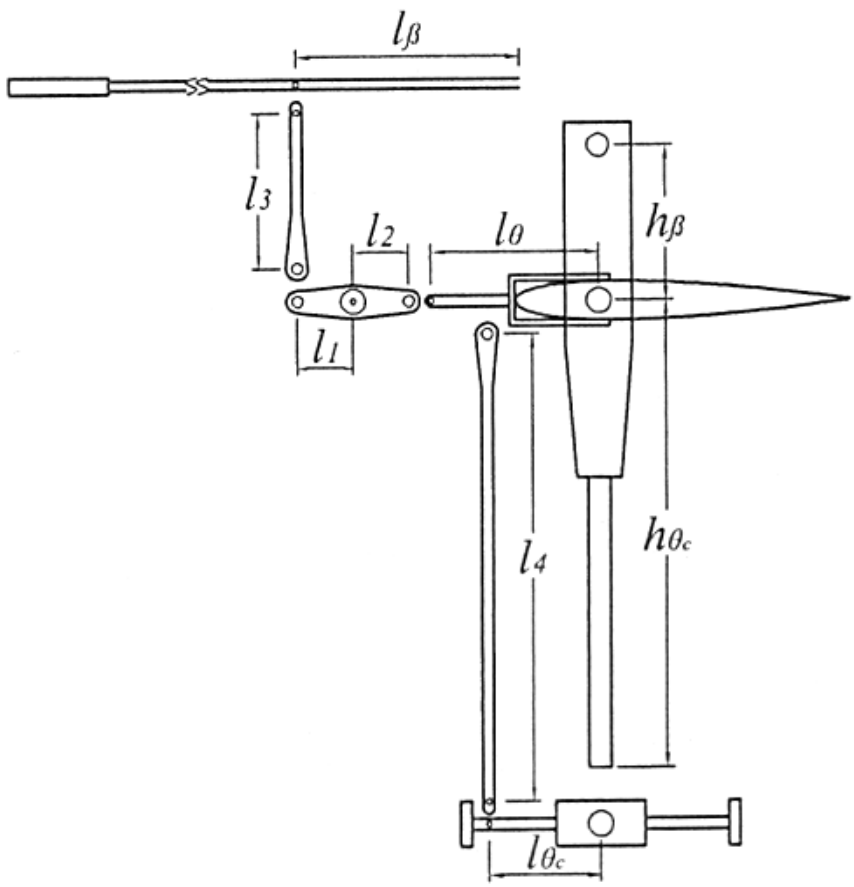

Figure 26: Expanded Drawing with Dimension Information

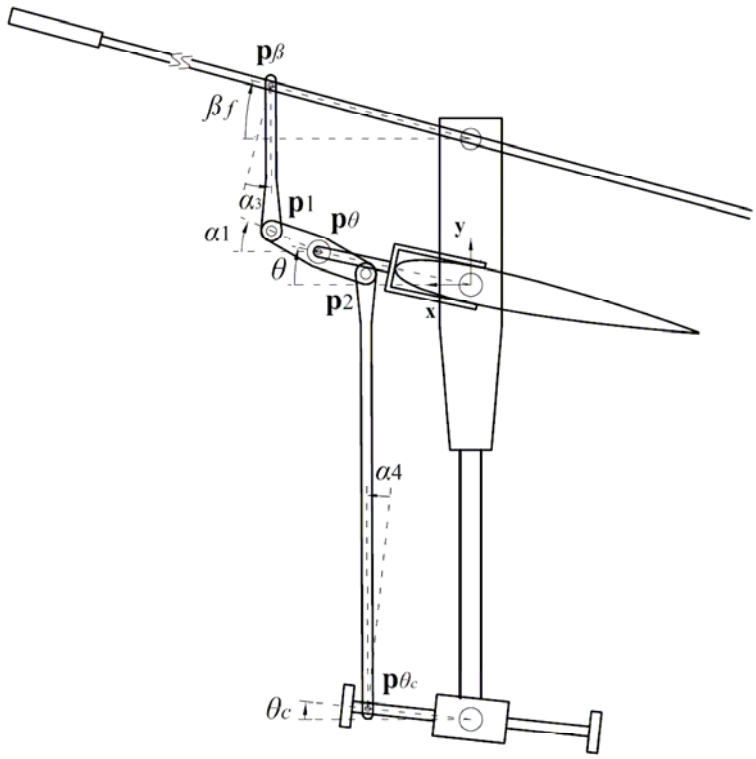

Figure 27: Bell-Hiller System with Angular Displacement

Table 3: Notation for the Bell-Hiller System

Variable	Description
θ	Blade pitch angle
β_f	Flybar flapping angle
θ_c	Pitch angle command from the swashplate
α_1, α_2, α_3	Auxiliary angles
h_{β_f}	Distance between the flybar pitching axis and blade pitching axis
h_{θ_c}	Distance between the swashplate and the blade pitching axis (follows swashplate)
l_θ	Arm length between p_θ and the blade pitching axis
l_{β_f}	Arm length between p_{β_f} and the flybar flapping axis
l_{θ_c}	Arm length between p_{θ_c} and the swashplate tilting axis
l_1	Arm length between p_1 and p_θ
l_2	Arm length between p_2 and p_{θ_1}

3 High-Order LPV Model

This section talks about the approach taken to develop the high-order LPV model. Specifically, this chapter focuses on the rotor-body coupling, which leads to the development of a high-order model. The hybrid model formulation, which combines the low frequency rigid body dynamics and the high frequency rotor dynamics, is discussed.

3.1 Rotor-Body Coupling

As discussed earlier, for the design of a high-bandwidth control system, the model should be able to capture the dynamics of the helicopter at all frequencies of interest. The quasi-steady formulation is able to predict the dynamics in the low- and mid-frequency ranges. For the model to give accurate results at higher frequencies, the rotor flap, lead-lag, and inflow dynamics must be modeled. However, the lead-lag dynamics are not considered in this research.

The rotor flapping dynamics couple with the body through the 1/rev flap moments (Figure 28[20]) that result from the rotor aerodynamic forces. The rotor aerodynamic forces are the thrust T acting normal to the rotor disk, the rotor drag force H, and the rotor side force Y. The rotor forces are obtained by integrating the blade section forces along the span. The rotor thrust is due to the normal force F_z while the drag and side forces are due to the in-plane forces F_x and F_r resolved in the non-rotating

frame. The torque is due to the in-plane force F_x. These rotor forces in coefficient form averaged over the azimuth are as given in the following equations:

$$\frac{C_T}{\sigma a} = \int_0^1 \frac{F_z}{ac} dr \tag{3.1}$$

$$\frac{C_H}{\sigma a} = \int_0^1 \left(\frac{F_x}{ac} \sin\psi + \frac{F_r}{ac} \cos\psi \right) dr \tag{3.2}$$

$$\frac{C_Y}{\sigma a} = \int_0^1 \left(-\frac{F_x}{ac} \cos\psi + \frac{F_r}{ac} \sin\psi \right) dr \tag{3.3}$$

$$\frac{C_Q}{\sigma a} = \int_0^1 r \frac{F_x}{ac} dr \tag{3.4}$$

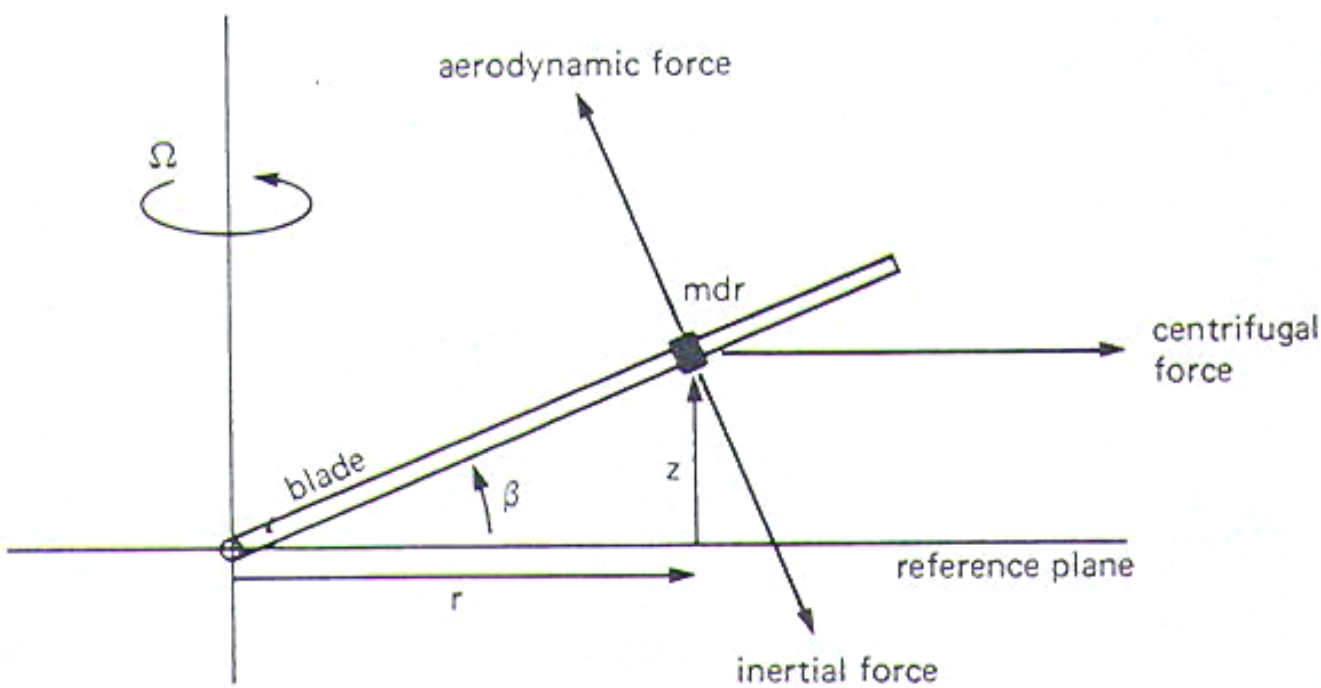

Figure 28: Rotor Blade Flapping Moments

The pitching and rolling moments on the rotor hub are given by the following equations:

$$M_y = -N\int_0^R \cos\psi r F_z dr \tag{3.5}$$

$$M_x = -N\int_0^R \sin\psi r F_z dr \tag{3.6}$$

The root flapping moment on a single blade in the rotating frame is:

$$M_F = \int_0^R r F_z dr \tag{3.7}$$

From writing M_F as a Fourier series and averaging the rotor moments over the azimuth, the pitching and the rolling moments are given as below:

$$M_y = -\frac{N}{2} M_{F_{1c}} \tag{3.8}$$

$$M_x = \frac{N}{2} M_{F_{1s}} \tag{3.9}$$

Hence, the 1/rev flapping moments at the center of rotation lead to the steady pitching and rolling moments on the helicopter. In general, the pitching and rolling moments can be related to the rotor tip-path-plane tilt, which is a measure of the 1/rev flapping moments. The following equations show the relation between the rotor thrust, pitching, and rolling moments and the rotor coning and flapping dynamics[71].

$$C_T = \frac{0.543}{\Omega}\dot{v}_0 + 2\left(v_0 - \frac{w}{\Omega R} + \frac{2}{3}\frac{\dot{\beta}_0}{\Omega}\right) \tag{3.10}$$

$$C_M = \frac{a\sigma}{16} M_{F_{1c}} \tag{3.11}$$

$$C_L = \frac{a\sigma}{16} M_{F_{1s}} \tag{3.12}$$

where

$$M_{F_{1c}} = A_1 - a_1' - b_1 - \frac{q}{\Omega} + \lambda_{1c} \tag{3.13}$$

$$M_{F_{1s}} = B_1 - b_1' + a_1 - \frac{p}{\Omega} + \lambda_{1s} \tag{3.14}$$

In order to develop a coupled body/rotor dynamics model, a hybrid formulation[19] is used in which both the rotor and fuselage dynamics are combined. In this approach, the equations of motion for rotor dynamics are first simplified as in Ref. 62, in which the rotor forces and moments are expressed as functions of the rotor states. The rotor dynamics are then coupled into the rigid body dynamics. The coupling is done through the flapping derivatives (or the rotor spring terms) X_{a_1}, Y_{b_1}, M_{a_1}, L_{b_1} [10]. All the quasi-steady derivatives are retained except for M_q, L_p, $L_{\delta_{lat}}$, $M_{\delta_{lon}}$, etc. The pitch and roll damping are captured by the rotor damping. The inputs are directly included in the rotor dynamics as discussed in the rotor flapping equations. The lateral and longitudinal inflow dynamics are also included in the rotor equations.

3.2 Rotor-Stabilizer Bar Coupling

As discussed earlier, the stabilizer bar does not produce any thrust. It has no collective blade pitch setting and the paddles are free to teeter (no restraint) about the

rotor shaft. Hence, the stabilizer bar does not produce any significant force or moment on the hub. The stabilizer bar affects the vehicle dynamics solely by augmenting the cyclic pitch command to the main rotor via the Bell-Hiller mixer. The stabilizer bar couples to the main rotor by augmenting the cyclic input to the main rotor as given in equation 2.89-90 and reproduced here.

$$\bar{\delta}_{lon} = \delta_{lon} + K_{a_{1_s}} a_{1_s} \tag{3.15}$$

$$\bar{\delta}_{lat} = \delta_{lat} + K_{b_{1_s}} b_{1_s} \tag{3.16}$$

The cyclic inputs to the main rotor are augmented by an amount that is proportional to the stabilizer bar flapping angles.

3.3 Heave-Inflow-Coning Dynamics

Also considered in this research are the coupled heave-coning-inflow dynamics. The vertical motion of the helicopter is influenced by the rotor coning and inflow dynamics. In Ref. 72, Chen and Hindson developed a model that included the influence of rotor coning and inflow dynamics on the helicopter's vertical response. Recently, Mark Tischler et al have used a similar model of the heave-coning-inflow dynamics for the AFDD R-MAX helicopter[5]. The present work uses the same approach on the heave-inflow-coning dynamics.

For the low frequency collective inputs, the quasi-steady model is able to predict the helicopter vertical dynamics very well. But, at moderate to high frequencies, the quasi-steady model cannot predict the transient thrust peaks to sharp collective inputs.

Carpenter and Fridovitch first examined the effect of the sharp and large collective inputs on the rotor thrust[65]. The measured rotor thrust was compared with the results predicted by a dynamic rotor coning/inflow nonlinear simulation model. In the model, the thrust changes, T, were modeled by the momentum theory, extended to include the unsteady effects on an apparent mass of air, defined by the circumscribed sphere of the rotor as given below:

$$T = m_{am}\frac{dv_i}{dt} + 2\pi R^2 \rho v_i \left(v_i - w + \frac{2}{3} R \frac{da_0}{dt} \right) \tag{3.17}$$

where

$$m_{am} = 0.637\rho \frac{4}{3}\pi R^3 \tag{3.18}$$

An extensive analysis of the flight dynamics of the helicopter's vertical motion, including the effects of the helicopter motion, rotor flapping and inflow, was conducted by Chen and Hindson (Ref. 72). Chen and Hindson predicted the behavior of the integrated 3-DoF system and presented comparisons with flight test data measured on a CH-47 helicopter. The linearized 3-DoF model presented by Chen and Hindson which can readily be incorporated into the dynamics model is as given below:

$$\frac{d}{dt}\begin{bmatrix} v_i \\ a_0 \\ \dot{a}_0 \\ w \end{bmatrix} - \begin{bmatrix} I_{v_i} & 0 & I_{\dot{a}_0} & I_w \\ 0 & 0 & 1 & 0 \\ F_{v_i} & F_{a_0} & F_{\dot{a}_0} & F_w \\ Z_{v_i} & Z_{a_0} & Z_{\dot{a}_0} & Z_w \end{bmatrix} = \begin{bmatrix} I_{\theta_0} \\ 0 \\ F_{\theta_0} \\ Z_{\theta_0} \end{bmatrix} \left[\theta_0 \right] \tag{3.19}$$

where

$$I_{v_i} = -4k_1\left(\lambda_0 + \frac{a\sigma}{16}\right) \tag{3.20}$$

$$I_{\dot{a}_0} = -\frac{4}{3}Rk_1\left(\lambda_0 + \frac{a\sigma}{16}\right) = -\frac{2R}{3}I_w \tag{3.21}$$

$$-F_{v_i} = F_w = -\frac{\Omega\gamma}{k_2 R}\left(\frac{1}{6} - \frac{N_b M_\beta}{4mR}\right) \tag{3.22}$$

$$F_{a_0} = -\frac{\Omega^2}{k_2} \tag{3.23}$$

$$F_{\dot{a}_0} = -\frac{\Omega\gamma}{k_2}\left(\frac{1}{8} - \frac{N_b M_\beta}{6mR}\right) \tag{3.24}$$

$$Z_{v_i} = -Z_w = \frac{N_b\Omega\gamma}{k_2 Rm}\left(\frac{I_\beta}{4R} - \frac{M_\beta}{6}\right) \tag{3.25}$$

$$Z_{a_0} = -\frac{N_b M_\beta \Omega^2}{k_2 m} \tag{3.26}$$

$$Z_{\dot{a}_0} = -\frac{N_b\Omega\gamma}{k_2 m}\left(\frac{I_\beta}{6R} - \frac{M_\beta}{8}\right) \tag{3.27}$$

$$I_{\theta_0} = \frac{25\pi\Omega^2 Ras}{256} \tag{3.28}$$

$$F_{\theta_0} = \frac{\Omega^2\gamma}{k_2}\left(\frac{1}{8} - \frac{N_b M_\beta}{6mR}\right),\ Z_{\theta_0} = -\frac{N_b\Omega^2\gamma}{k_2 m}\left(\frac{I_\beta}{6R} - \frac{M_\beta}{8}\right) \tag{3.29}$$

In the above equations,

$$k_1 = \frac{75\pi\Omega}{128} \text{ and } k_2 = 1 - \frac{N_b {M_\beta}^2}{mI_\beta} \tag{3.30}$$

where

$$M_\beta = \frac{4I_b}{3R} \tag{3.31}$$

The validation of the above vertical flight model is discussed extensively in Refs. 73-76. The authors in the references show the validation of the above models by comparing the model prediction with the flight data.

3.4 14-DoF LPV Model

Finally, with all the couplings discussed above, we get the coupled rotor/fuselage equations of motion. As discussed earlier, the coupling is done through the rotor states. The coupled rotor/fuselage equations, which are based on hybrid model formulation, are given below:

$$\dot{u} = X_u u + X_w w - W_0 q - g\theta + X_v v + X_{a_1} a_1 + X_{col}\delta_{col} \tag{3.32}$$

$$\dot{v} = Y_u u + Y_w w + Y_v v + g\phi + \left(Y_r - U_0\right) r + Y_{b_1} b_1 + Y_{\delta_{col}}\delta_{col} + Y_{\delta_{ped}}\delta_{ped} \tag{3.33}$$

$$\begin{aligned}\dot{w} = {} & Z_u u + Z_w w + \left(U_0 + Z_q\right) q - g\theta_0 + Z_r r + Z_{\lambda_0}\lambda_0 + Z_{a_0} a_0 + \\ & Z_{\dot{a}_0}\dot{a}_0 + Z_{lon}\delta_{lon} + Z_{col}\delta_{col}\end{aligned} \tag{3.34}$$

$$\dot{p} = L_u u + L_w w + L_v v + L_r r + L_{b_1} b_1 + L_{\delta_{col}}\delta_{col} + L_{\delta_{ped}}\delta_{ped} \tag{3.35}$$

$$\dot{q} = M_u u + M_w w + M_v v + M_{a_1} a_1 + M_{\delta_{col}}\delta_{col} \tag{3.36}$$

$$\dot{r} = N_u u + N_w w + N_v v + N_p p + N_r r + N_{col}\delta_{col} + N_{ped}\delta_{ped} \tag{3.37}$$

The above equations, when combined with the rotor flapping equations (2.34-2.35), the inflow equation (2.81), the stabilizer bar equations (2.86-2.87), and the

heave-coning-inflow equations (3.29) result in a 14-DoF 17 state model. The A and B matrices for this model are given in the equations 3.38 and 3.399 respectively.

$$A=\begin{bmatrix}
X_u & 0 & 0 & -g & X_v & 0 & 0 & 0 & X_{a_1} & 0 & 0 & 0 & 0 & 0 & 0 & 0 & 0 \\
Z_u & Z_w & 0 & 0 & 0 & 0 & 0 & 0 & 0 & 0 & 0 & 0 & 0 & 0 & Z_{a_0} & Z_{\dot{a}_0} & Z_{v_i} \\
M_u & M_w & 0 & 0 & M_v & 0 & 0 & 0 & M_{a_1} & 0 & 0 & 0 & 0 & 0 & 0 & 0 & 0 \\
0 & 0 & 1 & 0 & 0 & 0 & 0 & 0 & 0 & 0 & 0 & 0 & 0 & 0 & 0 & 0 & 0 \\
Y_u & 0 & 0 & 0 & Y_v & 0 & g & Y_r & 0 & Y_{b_1} & 0 & 0 & 0 & 0 & 0 & 0 & 0 \\
L_u & 0 & 0 & 0 & L_v & 0 & 0 & L_r & 0 & L_{b_1} & 0 & 0 & 0 & 0 & 0 & 0 & 0 \\
0 & 0 & 0 & 0 & 0 & 1 & 0 & 0 & 0 & 0 & 0 & 0 & 0 & 0 & 0 & 0 & 0 \\
0 & N_w & 0 & 0 & N_v & N_p & 0 & N_r & 0 & 0 & 0 & 0 & 0 & 0 & 0 & 0 & 0 \\
0 & 0 & -1 & 0 & 0 & \frac{1}{\Omega\tau_f} & 0 & 0 & \frac{-1}{\tau_f} & \frac{A_b}{\tau_f} & \frac{A_c}{\tau_f} & 0 & \frac{-1}{\tau_f} & 0 & 0 & 0 & 0 \\
0 & 0 & \frac{-1}{\Omega\tau_f} & 0 & 0 & -1 & 0 & 0 & \frac{-B_a}{\tau_f} & \frac{-1}{\tau_f} & 0 & \frac{B_d}{\tau_f} & 0 & \frac{1}{\tau_f} & 0 & 0 & 0 \\
0 & 0 & -1 & 0 & 0 & 0 & 0 & 0 & 0 & 0 & \frac{-1}{\tau_s} & 0 & 0 & 0 & 0 & 0 & 0 \\
0 & 0 & 0 & 0 & 0 & -1 & 0 & 0 & 0 & 0 & 0 & \frac{-1}{\tau_s} & 0 & 0 & 0 & 0 & 0 \\
0 & 0 & \frac{KR-\sigma 1}{\tau_i\Omega} & 0 & 0 & 0 & 0 & 0 & 0 & \frac{-\sigma 1}{\tau_i} & 0 & \frac{\sigma 1 B_d}{\tau_i} & \frac{\sigma 1-1}{\tau_i} & 0 & 0 & 0 & 0 \\
0 & 0 & 0 & 0 & 0 & \frac{KR-\sigma 1}{\tau_i\Omega} & 0 & 0 & \frac{\sigma 1}{\tau_i} & 0 & \frac{\sigma 1 A_c}{\tau_i} & 0 & 0 & \frac{\sigma 1-1}{\tau_i} & 0 & 0 & 0 \\
0 & 0 & 0 & 0 & 0 & 0 & 0 & 0 & 0 & 0 & 0 & 0 & 0 & 0 & 0 & 1 & 0 \\
0 & F_w & 0 & 0 & 0 & 0 & 0 & 0 & 0 & 0 & 0 & 0 & 0 & 0 & F_{a_o} & F_{\dot{a}_0} & F_{v_i} \\
0 & I_w & 0 & 0 & 0 & 0 & 0 & 0 & 0 & 0 & 0 & 0 & 0 & 0 & 0 & I_{\dot{a}_0} & I_{v_i}
\end{bmatrix} \tag{3.38}$$

$$
B = \begin{bmatrix}
0 & 0 & 0 & 0 \\
Z_{\delta_{col}} & Z_{\delta_{lon}} & 0 & 0 \\
M_{\delta_{col}} & 0 & 0 & 0 \\
0 & 0 & 0 & 0 \\
0 & 0 & 0 & Y_{ped} \\
0 & 0 & 0 & L_{ped} \\
0 & 0 & 0 & 0 \\
0 & 0 & 0 & N_{ped} \\
0 & \frac{A_{lon}}{\tau_f} & \frac{A_{lat}}{\tau_f} & 0 \\
-\ 0 & \frac{B_{lon}}{\tau_f} & \frac{Blat}{\tau_f} & 0 \\
0 & C_{lon} & 0 & 0 \\
0 & 0 & D_{lat} & 0 \\
0 & 0 & \frac{\sigma 1 B_{lat}}{\tau_i} & 0 \\
0 & \frac{\sigma 1 A_{lon}}{\tau_i} & 0 & 0 \\
0 & 0 & 0 & 0 \\
F_{\delta_{col}} & 0 & 0 & 0 \\
I_{\delta_{col}} & 0 & 0 & 0
\end{bmatrix} \tag{3.39}
$$

The state vector for the above model is given below:

$$
x = \begin{bmatrix} u & w & q & \theta & v & p & \phi & r & a_1 & b_1 & a_{1_s} & b_{1_s} & a_0 & \dot{a}_0 & \lambda_0 & \lambda_{1_c} & \lambda_{1s} \end{bmatrix}'
$$

It is seen in the equations 2.34 and 2.35 that the longitudinal and lateral flapping are functions of μ. Similarly, in equations 3.32 to 3.37, the derivatives such as X_u, Z_w, M_u, et cetera, are functions of μ. For example, the formula for Z_w is:

$$Z_w = -\frac{\rho a \mu \Omega R A b}{2m}\left(\frac{4}{8\mu + a\sigma}\right) \tag{3.40}$$

However, the value of μ depends on the forward speed. Due to the pilot input, there is a change in the forward speed and in the other parameters. The present work feeds those changes back into the model, calculating the new value of μ at each simulation time step. Also calculated are the new trim values. Thus, we have a linear parameter-varying model. Unlike linear parameter invariant models, in which the derivatives are held fixed throughout the simulation, this technique gives us a simulation model which results in a more representative prediction of actual flight dynamics. Figure 29 shows the LPV model implemented within Simulink.

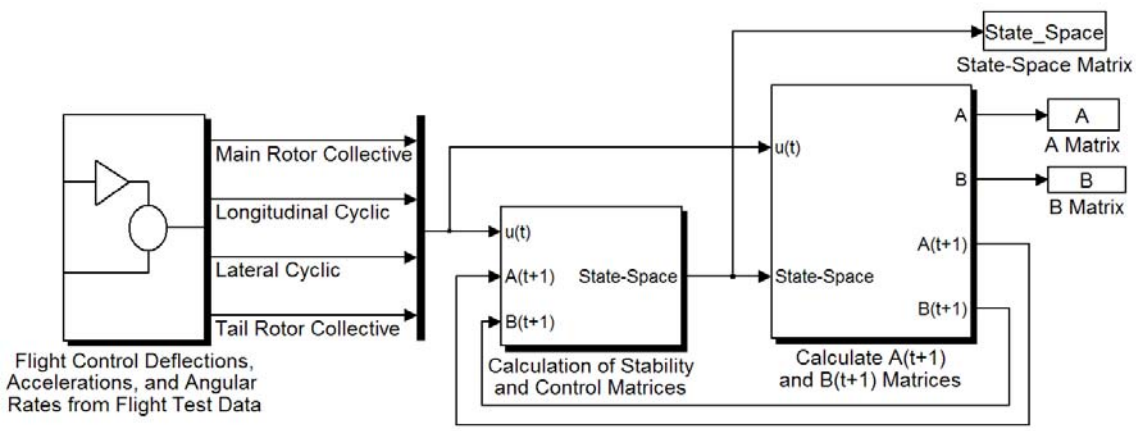

Figure 29: Linear Parameter Varying Simulation Diagram

4 Identification of the Dynamics Model using Flight Test Data

Since helicopter dynamics are very complex, the development of a dynamics model using analytical techniques alone is not sufficient. Also, modeling using analytical techniques is very time consuming. To overcome these difficulties, the rotorcraft dynamics modeling community has resorted to parameter identification techniques to complement the analytic models. The development of helicopter dynamics models using parameter identification techniques are discussed in Refs. 18, 37, 38, and 39. These references discuss various approaches to parameter identification, mainly the time-domain approach.

This section presents the development of the high-order model using CIFER software[17]. This program is an interactive facility for system identification and verification based on a comprehensive frequency-response approach. One of the big advantages of this software is that no prior assumption is necessary to characterize the dynamics system. CIFER describes the dynamic behavior of a system with a mathematical procedure based on the Fourier transform by using extracted flight test data. As with any other parameter identification program, the first step in CIFER is to use the measured flight test data to develop a model that reflects the real system behavior as accurately as possible.

An advanced Chirp-Z-transform and optimal window techniques are used in CIFER. Both features significantly improve the frequency response quality when compared to conventional Fast Fourier Transforms (FFTs). Nonlinear search

algorithms are used in CIFER to derive a model, which matches the flight data as closely as possible. Rapid identification of the transfer function models, along with spectral signal analysis, is enabled by the modular concept used for the CIFER software package. The program has been used for handling qualities assessment, classical servo-loop analysis, and for time- and frequency-domain comparisons between the system identification and the simulation predictions. CIFER is a tool for the comprehensive analysis of the aircraft and component dynamics that has been used on rotary- and fixed-wing aircraft such as the XV-15[77], Bell-214ST, BO-105, AH-64, UH-60, V-22, AV-8B Harrier, and OH-58D. CIFER can run on both the Microsoft Windows and UNIX platforms. In the following, the theory of frequency response analysis is discussed followed by a discussion covering the CIFER tools that are used for the development of the high-order model.

4.1 Theory of Frequency Response Analysis

The general mathematical idea behind frequency response analysis is that the system response is characterized as having the same frequency as the commanded input by the pilot. However, the magnitude and phase relationship between the inputs and the outputs is a function of the system characteristics, which results in a change in the magnitude and phase from the input to the output, as shown in Figure 30. Selected input–output pairs of frequency sweeps are used in a frequency-domain approach to identify the system response with a spectral analysis method based on the change of the magnitude and the phase between the input and the output. The frequency

response analysis is a linear approximation of the nonlinear aircraft dynamics. The linear approximation is close enough to the actual response if the frequency response analysis is limited to small amplitudes about a trimmed flight condition. For example, a frequency sweep about a trimmed hover condition with lateral control as the measured input and the helicopter roll rate as the measured output can be used to identify the helicopter roll response[78].

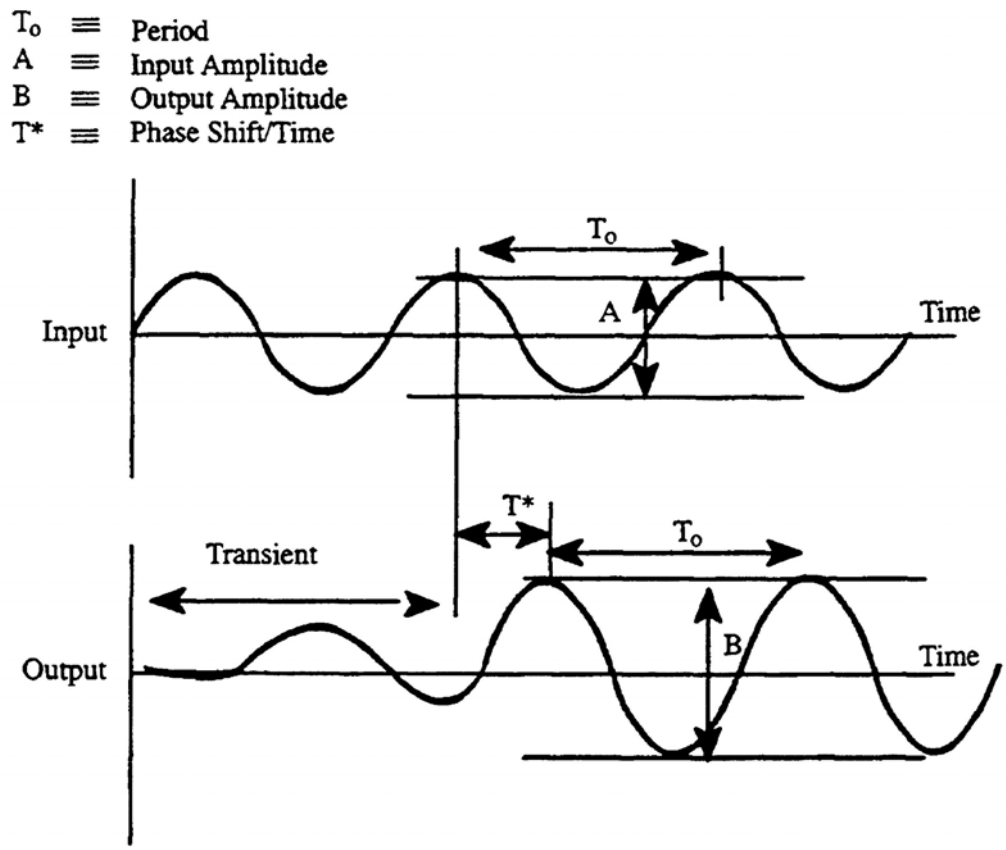

Figure 30: Sinusoidal Input-Output Time History

Frequency-domain analysis has some important advantages when compared to the time-domain approach, and provides a simpler and more precise analysis. In the time-

domain, the collected data is very sensitive to the changes in control input shape. The effects of these changes in the input shape cannot be neglected, especially if the response becomes more sensitive. This problem does not appear in the frequency-domain, particularly at the higher frequencies. At the mid- and high-frequency ranges, frequency-domain analysis results in a very good coherence between the model and the system. At low frequencies, the time-domain approach achieves better results. The analysis of unstable systems in the time-domain is more difficult because of integration errors, which occur as a result of instabilities. Frequency-domain analysis can be used for stable as well as unstable systems[78, 79].

4.1.1 Definition of the Frequency Response

Fourier transforms are used in frequency response analysis to develop a complex-valued function in order to relate the system outputs to the system inputs. The Fourier transform function is written as:

$$H_{(f)} = \frac{Y_{(f)}}{X_{(f)}} = \int h_{(\tau)} \cdot e^{(-j\omega\tau)} d\tau \tag{4.1}$$

where X and Y represent the input and the output respectively as a function of the frequency f in Hz. $H_{(f)}$ is a complex-valued function where $\left|H_{(f)}\right|$ is the gain factor and $\phi_{(f)}$ is the phase shift as given below:

$$\left|H_{(f)}\right| = \sqrt{H^2_{real(f)} + H^2_{imag(f)}} \tag{4.2}$$

$$\phi_{(f)} = \tan^{-1}\left[\frac{H_{imag(f)}}{H_{real(f)}}\right] \tag{4.3}$$

A stable and linear time invariant single-input-single-output (SISO) system with a well-defined sinusoidal input $x_{(t)}$ at a frequency ω will produce a sinusoidal output $y_{(t)}$ at the same frequency.

$$X_{(t)} = A_{(\omega)} \cdot \sin \omega_{(t)} \tag{4.4}$$

$$Y_{(t)} = B_{(\omega)} \cdot \sin \omega_{(t+\phi)} \tag{4.5}$$

However, the output amplitude and the output phase will differ from the input amplitude and the input phase. The ratio of the output amplitude $Y_{(\omega)}$ to the input amplitude $X_{(\omega)}$ is the system gain factor $\left|H_{(f)}\right|$. The phase factor $\phi_{(f)}$ is the ratio of the output phase to the input phase at the frequency ω. The output $Y_{(\omega)}$ to the input $X_{(\omega)}$ ratio is a complex quantity of the sinusoidal Fourier transform function. The magnitude and phase angles, with the frequency ω as a parameter, are used to represent the transform function. From this, it follows that a linear system can be completely described in the frequency-domain by determining the output to the input amplitude ratio and the phase shift angle as a function of the frequency. Figure 31 describes a SISO system for one frequency, and Figure 32 describes a SISO system for a range of frequencies.

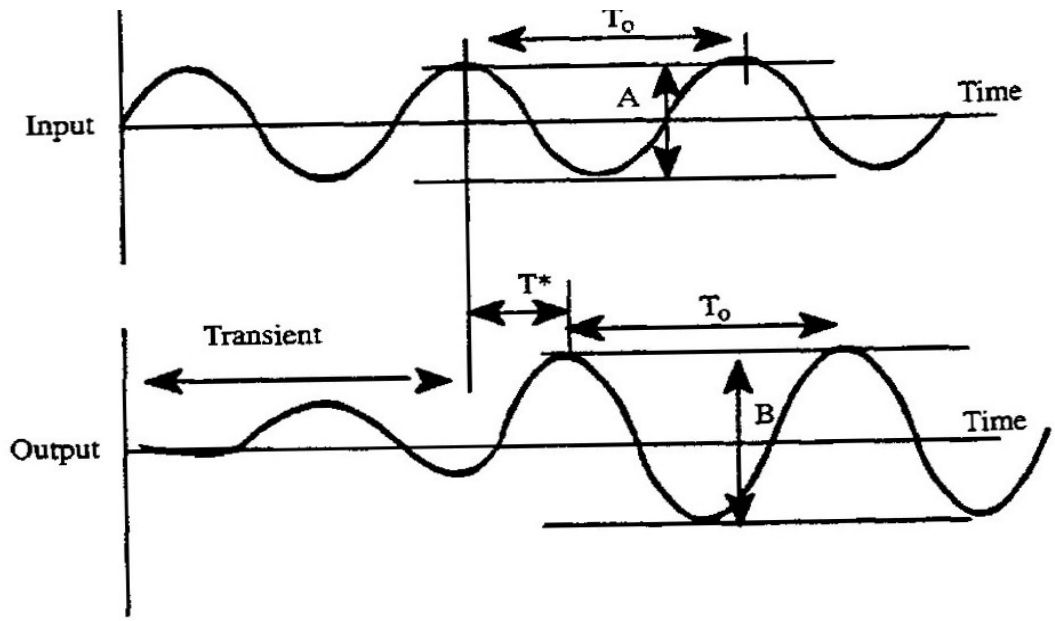

Figure 31: Single-Input Single-Output (SISO) System

The Fourier transforms for a stable or an unstable system's dynamics with an unknown input shape are defined as:

$$X_{(f)} = \int x_{(t)} \cdot e^{(-j\omega t)} dt \tag{4.6}$$

$$Y_{(f)} = H_{(f)} \cdot X_{(f)} \tag{4.7}$$

where $x_{(t)}$ is the system input and $y_{(t)}$ is the system output in the time-domain. $X_{(f)}$ and $Y_{(f)}$ are the system input and the system output, respectively, in the frequency-domain. The frequency response function will always exist if $x_{(t)}$ and $y_{(t)}$ are bounded and if the frequency sweep is started in a trimmed flight condition and returned to the trimmed flight condition after the sweep. More details about the

definition of the frequency response method are given in Refs. 78, 79, 80, and 81.

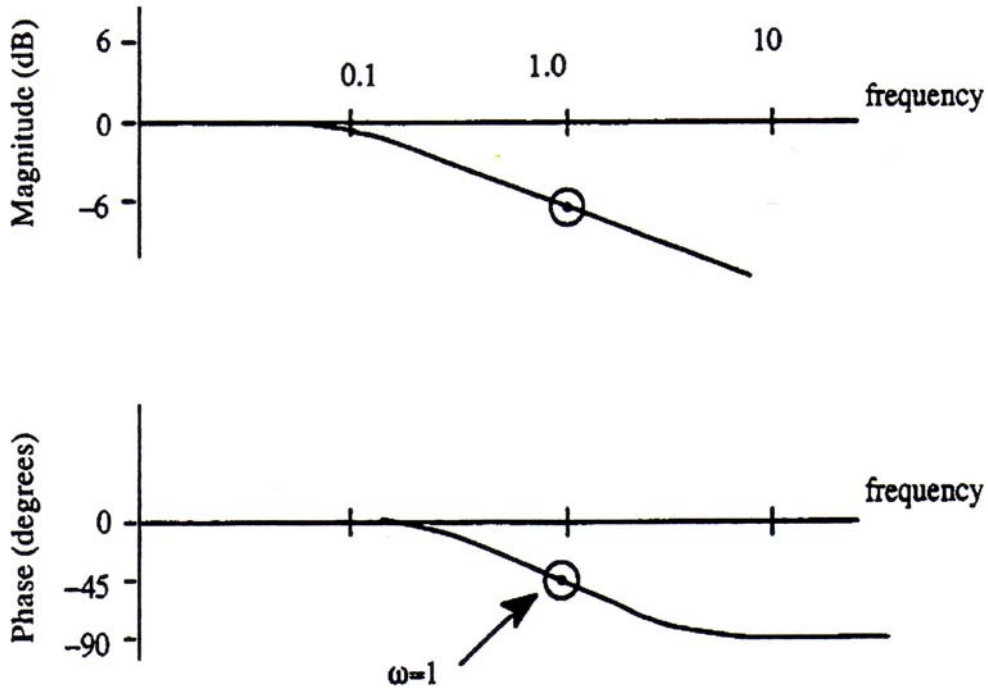

Figure 32: SISO Frequency Response

4.1.2 Frequency Response Calculation

Frequency response calculations are performed using the general Fourier transform of a continuous time system as follows:

$$X_{(f,T)} = \int x_{(t)} \cdot e^{(-j\pi ft)} dt \tag{4.8}$$

This Fourier transform can be approximated if the time-history data is from a discrete sequence, X_n, by the discrete Fourier transform (DFT) as given in the

following equation:

$$X_{(f_k)} = \Delta t \Sigma X_n e^{\frac{-j2\pi(kn)}{N}} \quad k = 0\ 1\ 2 \ldots N - 1 \tag{4.9}$$

where $X_{(f_k)}$ is the Fourier coefficient, Δt is the time increment, n is the number of frequency points, and $X_n = x(n\Delta t)$. The number of time-history points (L) and the number of frequency points (N) have to be the same for the DFT, so that the window size (discussed later) is $L\Delta t$ with a minimum frequency resolution of $1/(L \cdot \Delta t)$.

CIFER uses a special algorithm called the CHIRP-Z transform (CZT) for high-order systems like helicopters. The CZT is a highly flexible FFT, which is valid for $N \leq L$. The advantages are that this results in a finer frequency resolution for a given window size. The number of the time history points are arbitrary. More details on the CZT can be found in Ref. 82.

In Fourier analysis, a phenomenon called leakage occurs. This is a frequency content error that appears as side lobes to the Fourier frequency of interest. To reduce this error, a method called "windowing" is used in CIFER. The windowing technique refers to subrecords of the FFT total time history in which the window is sized to optimize the quality of the identification. Random errors in the results can be reduced by increasing the number of windows in which the time history is divided. This results in a higher averaging rate. The smaller windows also result in a lower spectral variance for a given data length. This leads to a compromise in the selection of

window length between a high number of averages and adequate low-frequency content.

A good control mechanism for the accuracy of the approximation of a system for a particular input-output dynamics is the coherence function γ_{xy}^2. The coherence function is defined by:

$$\gamma_{xy}^2 = \frac{\left|G_{xy}\right|^2}{\left|G_{xx}\right| \cdot \left|G_{yy}\right|} \tag{4.10}$$

In the above equation, G_{xx} and G_{yy} are the one-side input (x) and output (y) auto-spectral density estimates. G_{xy} is the one-side cross-spectral density estimate of X and Y containing information about the magnitude and phase relationship between X and Y[83]. The coherence function is the ratio of that part of the output data, which can be approximated with a linear relationship to the input data. In the ideal case, where the system is perfectly linear and there is no noise in the system, the coherence function would be unity over the entire frequency range. A coherence function of less than unity results from three basic causes:

- Nonlinearities in the system may produce remnants which are not accounted for by the first harmonic approximation
- Input and output noise
- Secondary inputs like gusts and turbulence

As shown in Figure 33, if a coherence function of 0.6 or greater is achieved, the

model can be seen as sufficiently accurate.

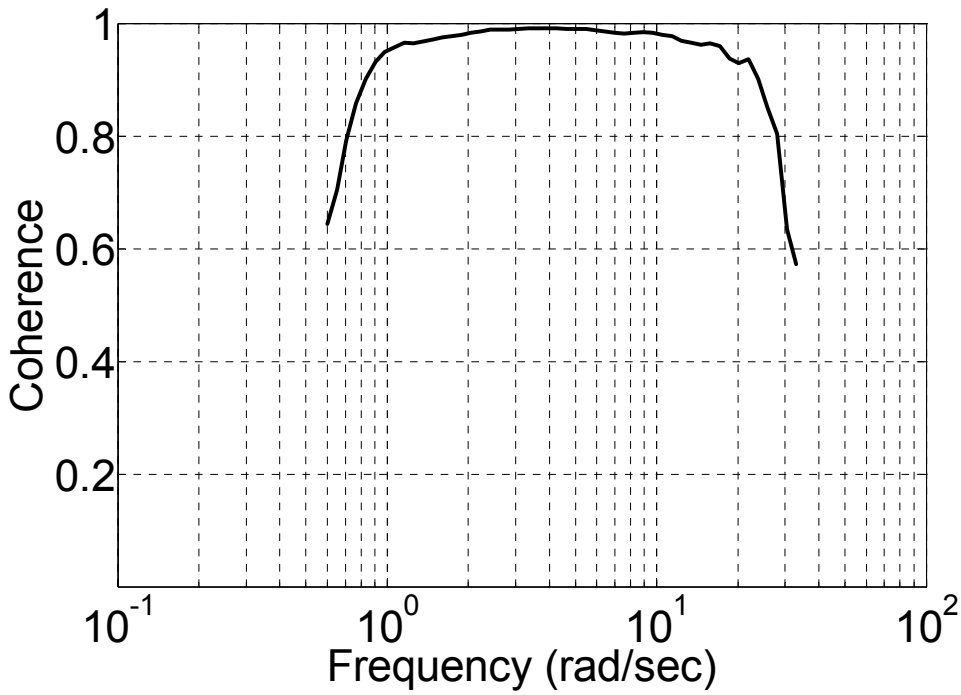

Figure 33: Coherence Plot

The frequency response analysis by CIFER results in a linearmodel which minimizes the mean square difference of the actual output signal and its approximation by the first harmonic component of the Fourier series. Frequency–domain analysis is described in great detail in Ref. 83.

4.2 CIFER Tools

CIFER is comprised of a set of tools to perform frequency-domain identification[17]. The tools were originally developed for rotorcraft identification but can also be used for other systems for which a frequency-response approach is indicated, such as for

the modeling of structural dynamics. All the tools are integrated around a database that conveniently organizes the large quantity of data generated throughout the identification process. The main tools included in the CIFER system are discussed in the following sections.

4.2.1 Frequency-Response Estimation (FRESPID)

This tool computes the frequency response for each input-output pair using a special FFT algorithm, Chirp-Z. Different window lengths are used in this process. At the same time, it computes the associated coherence function. These frequency responses are then stored in the database to be processed by the other tools.

4.2.2 Multivariable Frequency-Response Conditioning (MISOSA)

This tool conditions the SISO frequency responses from FRESPID. This program removes the effects of secondary inputs. At the same time, it computes partial coherences, which only reflect the effect of the primary input.

4.2.3 Optimal Window Combination (COMPOSIT)

This tool combines the frequency responses computed in FRESPID or in MISOSA using different window lengths to improve the accuracy of the low, middle, and high frequency ends. This process is solved through an optimization, which finds the weighted sum of the individual frequency response that maximizes the coherence across the entire frequency range.

4.2.4 Transfer Function Identification (NAVFIT)

This utility allows one to identify the parameters of a transfer function using a specified frequency response. The user can specify the order of the numerator and denominator, and whether a time delay should be included.

4.2.5 State-Space Identification (DERIVID)

This tool identifies the parameters of a user specified state-space model using the selected frequency responses.

4.2.6 Time-Domain Verification (VERIFY)

This utility performs a time-domain verification of the model. The time responses predicted by the identified model are compared with the actual vehicle responses collected from flight experiments. Usually, responses that are different from the ones used for the estimation of the frequency responses are used.

4.3 Advantages of CIFER

The CIFER system is a high-performance interactive software package using robust algorithms, valid for a wide range of control, optimization, identification, simulation, and validation applications. It allows for the simple and rapid development of an accurate mathematical model, reflecting the complex dynamic behaviors of airborne or ground-based systems. In fact, CIFER is the only low cost commercially available code which can handle a wide range of airborne and ground-

based cases. The key benefits of CIFER are as follows:

- Rapidly specifies, creates, optimizes, and validates dynamic features
- Extracts dynamic response without prior assumptions of the system
- Measures and correlates distributed mathematical models and motions
- Characterizes and quantifies simulator versus live system equivalence
- Reduces cost and risk

4.4 Flight Tests and Data Collection

High quality flight data is needed for a successful identification. The quality of the data depends on the accuracy of the measurements, the information content of the flight data, and the compatibility of the data with the premises of the linear system identification. While the measurement accuracy depends on the instrumentation, the information content and compatibility depend mostly on the flight experiments used for the data collection.

4.4.1 General Flight Testing Rules

The flight-testing rules are derived from the theoretical and practical considerations. From the properties of coupled multi-input-multi-output (MIMO) systems with correlated inputs, it is possible to determine the experimental conditions that are most favorable to good frequency-response estimation[83]. These conditions cannot typically be implemented entirely; a proper trade-off must be found. For this research, the guidelines in Ref. 78 are followed. The principal considerations are

discussed in the following sections.

4.4.1.1 Excitation Throughout the Frequency Range of Interest

The dynamic modes within the frequency range of interest should be excited during flight test. This is achieved by using frequency-sweep inputs (sinusoidal inputs with monotonically increasing frequency) as shown in for a longitudinal sweep. The low-frequency excitations (0.1-2 rad/sec) are important for the identification of quasi-steady effects, such as the aerodynamic derivatives. The high-frequency excitations are important for the identification of the effects beyond the rigid-body dynamics, such as the coupled rotor-fuselage dynamics and the stabilizer bar dynamics as well as time delays.

4.4.1.2 Record Length and Sampling Rate

The length of each recorded data segment T_d determines the lowest-frequency component that can theoretically be estimated from the data. The sampling interval T_s determines the upper limit[78]. The lowest frequency is given by $\omega_{\min} = 2\pi/T_d$. For practical applications, however, a record length that is at least twice the period of the lowest desired frequency ($T_d = \dfrac{4\pi}{\omega_{\min}}$) is recommended[84]. The highest frequency is prescribed by the Nyquist cut-off frequency $\omega_{\max} = \pi/T_s$.

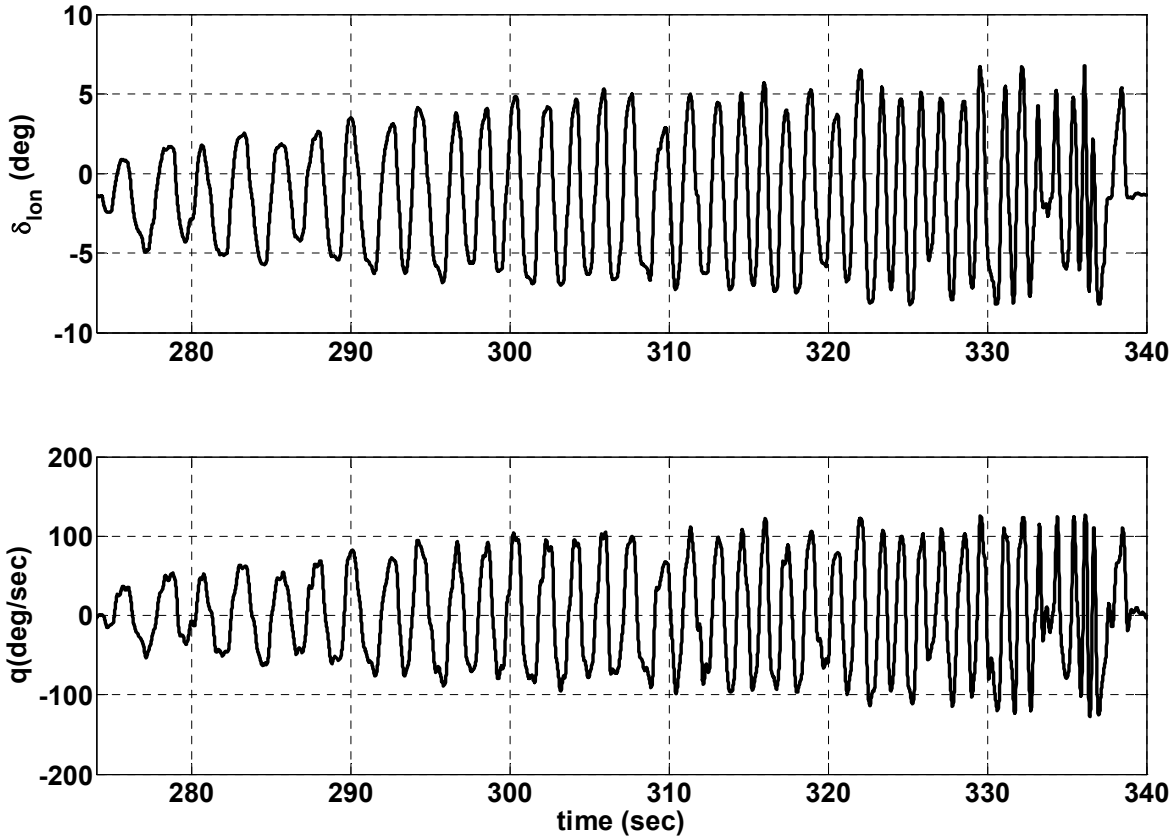

Figure 34: Time History of the Longitudinal Frequency Sweep

4.4.1.3 Operation within the Range of Linear Dynamics

The pilot should ensure that the magnitude of the vehicle's response remains within a region where its dynamics are mostly linear. This can be accomplished by adjusting the magnitude of the excitation. Small-scale rotorcraft, because of their high maneuverability, should tolerate higher control inputs. It is important to choose calm weather conditions, because wind gusts act as unmeasured inputs that can

significantly degrade the quality of the frequency-response estimates.

4.4.1.4 Correlation among Inputs

Correlation among control inputs bias the frequency-response estimates[83]. A possible source of correlation is pilot decoupling compensation, e.g. simultaneous compensation of the sweep input on the secondary axes. To minimize this effect, it is necessary to let the helicopter respond freely to the sweep excitation as much as possible. The low-frequency range of the test, where the helicopter can easily undergo large speed deviations, is the most challenging. In this situation, it is better to reduce the amplitude of the excitation than to try to compensate for its effect.

4.5 Order of the Identification Model

Initially, a 6-DoF model based on the quasi-steady assumption was identified using CIFER. In the next step, the order of the model was increased to include the rotor flapping dynamics, the stabilizer bar dynamics, and the coning and inflow dynamics. However, the longitudinal and the lateral inflow dynamics were not included in the identification process. Thus, for identification purposes, a reduced order model is used. This is a 12-DoF 15 states model. The A and B matrices of the identification model are given in equations 4.11 and 4.12 respectively.

The unknown model parameters are identified through an optimization process in which the frequency-response fitting error is minimized[78]. For this process, a cost function that measures how well the frequency responses calculated from the

parameterized model fit the estimated frequency response is built.

$$A = \begin{bmatrix} X_u & X_w & 0 & -g & X_v & 0 & 0 & 0 & X_{a_1} & 0 & 0 & 0 \\ 0 & Z_w & 0 & 0 & 0 & 0 & 0 & 0 & 0 & 0 & 0 & 0 \\ M_u & M_w & 0 & 0 & M_v & 0 & 0 & 0 & M_{a_1} & 0 & 0 & 0 \\ 0 & 0 & 1 & 0 & 0 & 0 & 0 & 0 & 0 & 0 & 0 & 0 \\ Y_u & 0 & 0 & 0 & Y_v & 0 & g & Y_r & 0 & Y_{b_1} & 0 & 0 \\ L_u & 0 & 0 & 0 & L_v & 0 & 0 & L_r & 0 & L_{b_1} & 0 & 0 \\ 0 & 0 & 0 & 0 & 0 & 1 & 0 & 0 & 0 & 0 & 0 & 0 \\ 0 & N_w & 0 & 0 & N_v & N_p & 0 & N_r & 0 & 0 & 0 & 0 \\ 0 & 0 & -\tau_f & 0 & 0 & 0 & 0 & 0 & -1 & M_{f_{b_1}} & M_{f_{a_{1_s}}} & 0 \\ 0 & 0 & 0 & 0 & 0 & -\tau_f & 0 & 0 & L_{f_{a_1}} & -1 & 0 & L_{f_{b_{1_s}}} \\ 0 & 0 & -1 & 0 & 0 & 0 & 0 & 0 & 0 & 0 & -\tau_s & 0 \\ 0 & 0 & 0 & 0 & 0 & -1 & 0 & 0 & 0 & 0 & 0 & -\tau_s \end{bmatrix} \quad (4.11)$$

$$B = \begin{bmatrix} 0 & 0 & 0 & 0 \\ Z_{col} & 0 & 0 & 0 \\ M_{col} & 0 & 0 & 0 \\ 0 & 0 & 0 & 0 \\ 0 & 0 & 0 & Y_{ped} \\ 0 & 0 & 0 & 0 \\ 0 & 0 & 0 & 0 \\ N_{col} & 0 & 0 & N_{ped} \\ 0 & M_{f_{\delta_{lon}}} & M_{f_{\delta_{lat}}} & 0 \\ 0 & L_{f_{\delta_{lon}}} & L_{f_{\delta_{lat}}} & 0 \\ 0 & M_{s_{\delta_{lon}}} & 0 & 0 \\ 0 & 0 & L_{s_{\delta_{lat}}} & 0 \end{bmatrix} \quad (4.12)$$

The cost function depends on the unknown parameters Θ, and is calculated as the

sum of the magnitude and phase errors evaluated over n_ω frequency points $\omega_1, \omega_2, ..., \omega_{n_\omega}$. In CIFER, the default number for n_ω is 50. The cost function has the general form:

$$J(\Theta) = \sum_{i=1}^{n_\omega} \varepsilon(\omega_i, \Theta)^T W(\omega_i) \varepsilon(\omega_i, \Theta) \tag{4.13}$$

where $\varepsilon(\omega_i, \Theta)$ is the vector of the magnitude and phase errors. $W(\omega_i)$ is the frequency dependent weighting function that emphasizes the frequency points at which the response is most accurate. It is usually determined by the coherence function.

4.6 Accuracy of the Identified Model Parameters

The final model structure is obtained by adding and removing derivatives depending on the following observations:

- The level of the frequency-response agreement (frequency error costs)
- Statistical metrics from the model parameters (insensitivity and Cramér-Rao percent)
- The level of agreement with the system's time responses (time-domain verification)
- The level of agreement of the parameter with its theoretical value

The useful statistics are:

- The insensitivity of the cost function to each derivative

- The Cramér-Rao (CR) bound, which gives a lower bound on the achievable standard deviation (indicating how accurately a parameter can be identified)
- The correlation among the derivatives

Insensitive parameters do not affect the value of the cost function (i.e. they can take any value without it being reflected in the fitting cost). Hence, they should be dropped. Parameters with high CR bounds cannot be identified accurately. Hence, if possible, they should be fixed at a known value or dropped from the parameterized model[79, 85, 87, 88]. With regard to the correlated parameters, those derivatives should be dropped or, when possible, fixed to a value determined theoretically.

The statistics used for the model refinement, including the insensitivity, CR bound, and correlation, are derived from the Hessian matrix H as given below[85]:

$$H = \frac{\partial^2 J(\Theta)}{\partial \Theta^2} \tag{4.14}$$

As discussed in Refs. 79 and 85, CR bounds are given by the following relationship:

$$CR_i = 2\sqrt{\left(H^{-1}\right)_{ii}} \tag{4.15}$$

The CR bounds are usually expressed as a percentage of the converged identification values as given below:

$$\overline{CR}_i = \left|\frac{CR_i}{\theta_i}\right| \times 100\% \tag{4.16}$$

A general guideline for a successful identification is to achieve the following:

$$\overline{CR}_i \leq 20\% \tag{4.17}$$

However, in the identification, several of the CR bounds can be in the range of 20%-40%, without loss of reliability or cause for concern.

Similarly, the parameter insensitivities are determined from the diagonal elements of the Hessian matrix as given below[85]:

$$I_i = \frac{1}{\sqrt{(H)_{ii}}} \tag{4.18}$$

The parameter insensitivities are also best expressed as the normalized percentages of the converged parameter values as given below:

$$\overline{I}_i = \left| \frac{I_i}{\theta_i} \right| \times 100\% \tag{4.19}$$

A general guideline for a reliable identification is to achieve the insensitivities as obtained from the frequency-response method as follows:

$$\overline{I}_i \leq 10\% \tag{4.20}$$

5 Results and Discussion

This chapter first discusses the data collection process and the post processing of the data. In the second section, results obtained from the analytical modeling are discussed. The results obtained from CIFER are covered in section three. Section four compares the analytical and the identified models with the flight data.

5.1 Data Collection and Post Processing

A number of flight tests were carried out to collect the flight data for both the hovering and the forward flight conditions. The collected data were filtered to remove the effect of noise using a second order Butterworth filter as shown in Figure 35 and post processing was done in MATLAB/Simulink to convert the data into appropriate engineering units as discussed in Ref. 61.

When the accelerometers are placed at the vehicle center of gravity, the sensors measure the accelerations the vehicle experiences as a result of the various forces acting on it. The corresponding mathematical expression is:

$$a_{meas} = a_{cg} = \frac{d^I mv}{dt} = \begin{bmatrix} a_x \\ a_y \\ a_z \end{bmatrix}_{meas} \tag{5.1}$$

The inertial accelerations expressed in terms of the time rate of change of body velocities are:

$$\frac{d^I mv}{dt} = \frac{d^B mv}{dt} + \omega \times v = \frac{F_{ext}}{m} = \frac{F_{grav}}{m} + \frac{F_{aero}}{m} \tag{5.2}$$

where F_{ext} is a vector of total forces acting on the vehicle and are made up of the sum of the aerodynamic and gravitational forces.

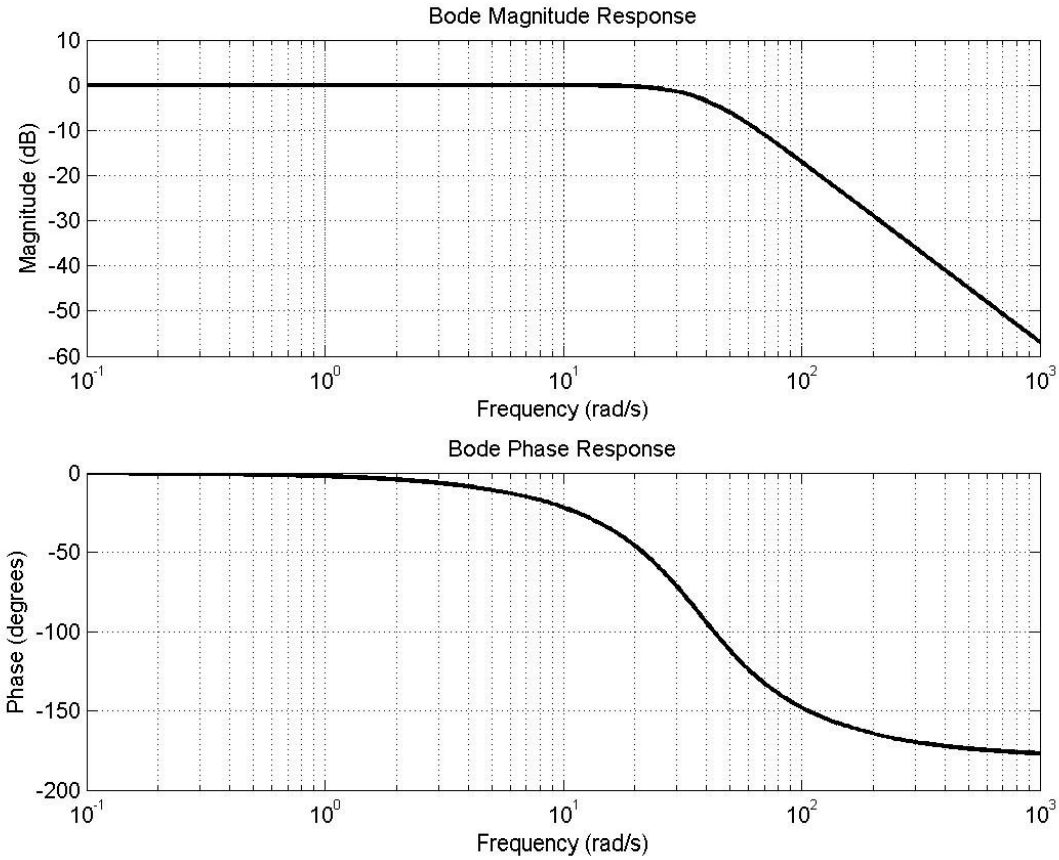

Figure 35: Bode Plot for the Second Order Butterworth Filter

The measured accelerations and the time rate of change of the vehicle body velocities can be related as given below:

$$a_{meas} = \begin{bmatrix} a_x \\ a_y \\ a_z \end{bmatrix}_{meas} = \dot{v} + \omega \times v - \frac{F_{grav}}{m} \tag{5.3}$$

The state-space model for the aircraft predicts body axis velocities. Thus, when fitting the frequency responses estimated from the acceleration measurements with

the transfer function derived from the state-space model, the centripetal effects $\omega \times v$ and gravitational forces must be accounted for.

Equation 5.3 assumes that the DMU is placed at the c.g. location. However, the DMU that houses the three accelerometers has a slight offset from the vehicle center of gravity. Therefore, the accelerations sensed are those of the attachment point on the helicopter fuselage. The accelerations measured at the sensor location offset from the c.g. location is given by the following equation:

$$a_{meas} = a_{cg} + \omega \times (\omega \times r_s) + \dot{\omega} \times r_s \tag{5.4}$$

where r_s is the position vector from the c.g. to the sensor location. The first term in the equation 5.4 is the acceleration at the c.g. location; the second and the third terms are centripetal and tangential biases, respectively.

The DMU installed on the Raptor 50 is offset from the c.g. location by $r_s = [0 \quad 0 \quad 0.5]^T \; ft$. The measured acceleration was corrected for this offset.

The corrected data were used to calculate the frequency responses for each input-output pair using the FRESPID program in CIFER. The MISOSA tool was used as required to remove the effect of the secondary inputs on the responses. The frequency responses obtained from FRESPID or MISOSA were then used in the COMPOSIT program of CIFER to maximize the coherence across the entire frequency range. The COMPOSIT responses were then used to identify the stability and control derivatives for the helicopter.

Analytically developed and parameter identified models were simulated using the

inputs collected during the flight tests. The model predictions were compared with the flight data as discussed in the following sections.

5.2 Low-Order Models

At first, it was thought that a 6-DoF model, with the couplings between the longitudinal and the lateral dynamics included, would produce satisfactory results, and would suffice for the design of the control system for the helicopter. Much of the early efforts concentrated on the development of the 6-DoF dynamics model for the Raptor 50.

Figure 36 shows a frequency domain comparison between the flight data and the 6-DoF model prediction. It is seen that the 6-DoF model is able to predict the on-axes roll and pitch rate only up to a frequency of 8 rad/sec. Above that frequency, the model response departs significantly from the flight data. The model is unable to capture the second order effects seen in the flight data. Similarly, the off-axis roll rate to longitudinal cyclic response clearly shows a 180° phase error. There are discrepancies in the magnitude also, especially at the higher frequencies. Also seen in the figure is a magnitude discrepancy between the flight data and the model prediction for the vertical acceleration to the collective input.

The inability of 6-DoF models to predict helicopter dynamics at higher frequencies has resulted in the design of control systems that produced significant vibration when implemented on the helicopters[31].

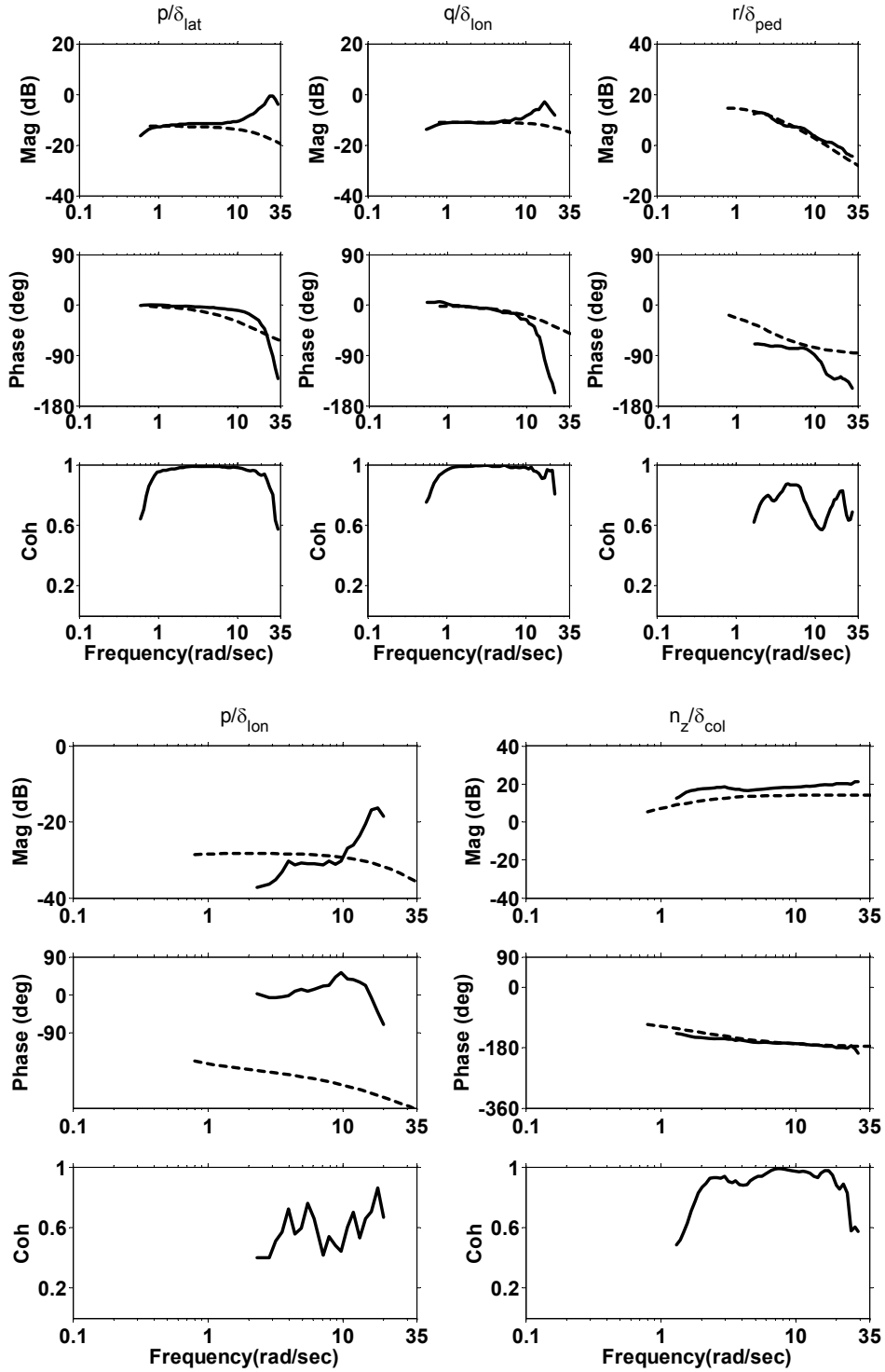

Figure 36: Frequency Domain Comparison of the 6-DoF Model Prediction (Dashed) with Flight Data (Solid) for Hovering Flight

Figure 37 and Figure 38 show the prediction of SISO transfer function models obtained from CIFER, compared with the flight data, for the cases of longitudinal and lateral frequency sweeps, respectively. The SISO models obtained from CIFER in the form of gain and time delay is given in the following equations.

$$\frac{pitch\_rate}{longitudinal\_cyclic\_input} = 0.31e^{-0.0637s} + 0.44 \tag{5.5}$$

$$\frac{roll\_rate}{lateral\_cyclic\_input} = 0.29e^{-0.0245s} - 0.35 \tag{5.6}$$

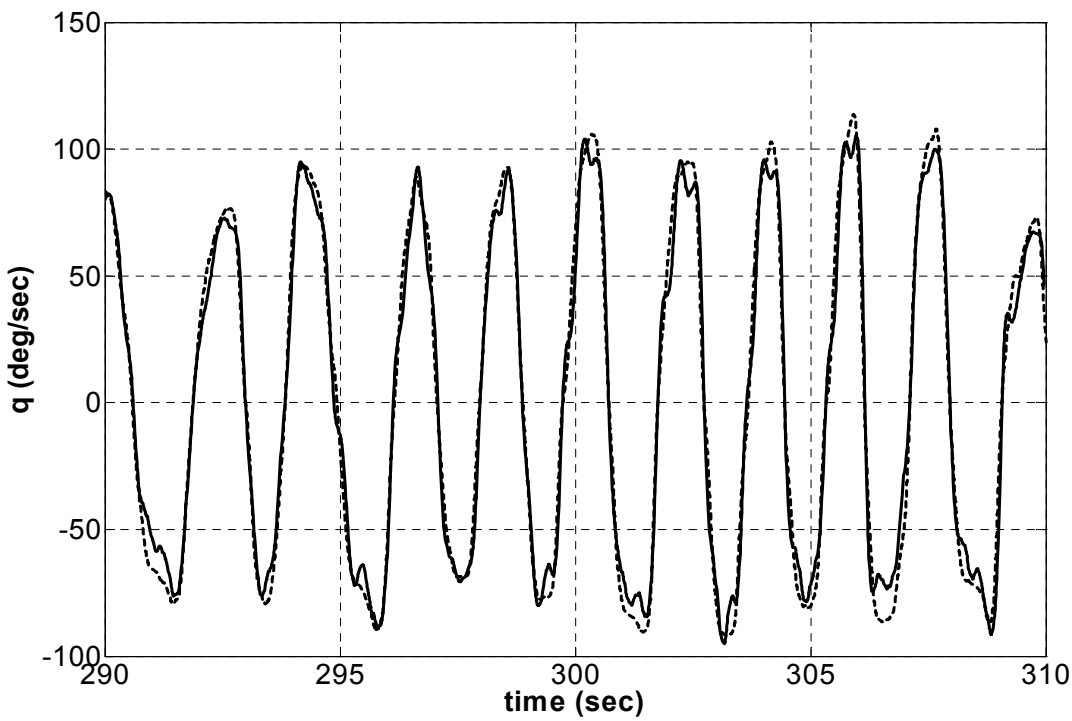

Figure 37: Flight Data (Solid) and SISO CIFER Model Prediction for Pitch Rate

Also obtained were transfer functions in the standard form as given below:

$$\frac{pitch\_rate}{longitudinal\_cyclic\_input} = \frac{92.2}{s + 293.86} \tag{5.7}$$

$$\frac{roll\_rate}{lateral\_cyclic\_input} = \frac{100.72}{s + 347.69} \tag{5.8}$$

However, there are some discrepancies in these responses as well. The SISO CIFER models are unable to predict some of the second or higher order modes present in the flight data. This implies that even when using a parameter identification technique, a model structure has to be defined to capture all the dynamics effects as discussed in Chapter 3.

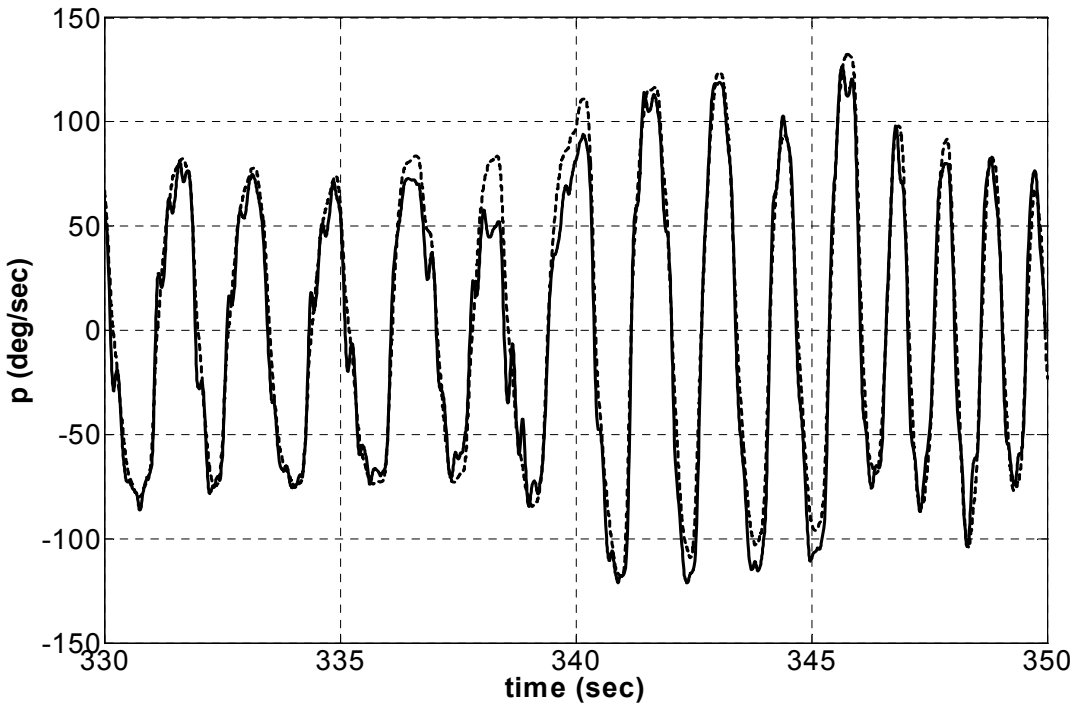

Figure 38: Flight Data (Solid) and SISO CIFER Model Prediction for Roll Rate

5.3 High-Order Models

Initially, a high-order model was developed theoretically. This provided much insight into the dynamics of UAV helicopters. As discussed in Chapter 3, the

analytical model is a 14-DoF 17 state model. Shown in Table 4 are the parameters from the analytically developed models for the hovering and forward flight conditions.

Theoretical calculation of the S&C derivatives for the Raptor 50 provided much information concerning the magnitudes and signs of the derivatives. This information was useful in identifying the derivatives using CIFER.

The frequency responses, especially the COMPOSIT responses, were used for the identification of the high-order model. The identification was done in different stages as discussed in Ref. 10. Initially, identification was done only for the attitude dynamics, with rotor degrees-of-freedom added to the identification structure to determine time constants and rotor spring derivatives. Then the stabilizer dynamics were added to the identification structure. This allowed the determination of the stabilizer bar derivatives. Finally, the other degrees-of-freedom were added to the identification model structure.

The above approach worked well for the hovering flight condition and all the derivatives were identified successfully. However, for the forward flight condition, when the stabilizer bar dynamics was added, a converging solution was not found. The main rotor time constant, τ_f, was obtained with high insensitivity. To rectify this problem, τ_f was held fixed to its theoretical value during identification. With this, the identification was completed successfully.

Table 4: **Theoretically Calculated Derivatives for the Raptor 50**

	Parameter Value	
Derivatives	**Hover**	**Forward Flight**
τ_f	0.0274	0.0274
τ_s	0.107	0.107
X_u	-0.009	-0.399
X_v	-0.0013	0.0785
X_{a_1}	-32.170	-32.170
Y_u	0.0013	0.0027
Y_v	-0.125	-0.6263
Y_{b_1}	32.170	32.170
Z_w	-0.890	-1.324
L_u	0.00438	0.000[b]
L_v	-0.157	-1.891
L_{b_1}	602.09	602.9
$L_{f_{b_{1_s}}}$	0.870	0.870
M_u	0.012	0.535
M_w	0.000	0.0679
M_v	0.0017	-0.1026
M_{a_1}	238.640	238.640
$M_{f_{a_{1_s}}}$	0.870	0.870
N_v	0.000	0.000
N_p	0.133	0.18058
N_r	-1.356	-1.8357
$Z_{\delta_{col}}$	-13.039	-13.039
$L_{f_{\delta lat}}$	0.011	0.0278
$L_{f_{\delta_{lon}}}$	0.000	0.000
$L_{s_{\delta_{lat}}}$	0.0118	0.0118
$M_{f_{\delta_{lon}}}$	0.011	0.011
$M_{f_{\delta_{lat}}}$	0.000	0.000
$M_{s_{\delta_{lon}}}$	0.0118	0.00118
$N_{\delta_{ped}}$	7.528	8.0634

Table 5 shows the identified parameters. Also shown are the Cramer Rao bounds (C. R.) and the insensitivities that are the measurement of the accuracy of the identified parameters[79].

With the identified parameters in Table 5, all the rates and vertical accelerations compared well with the flight data. However, there were some discrepancies in the longitudinal and lateral accelerations. This was due to the fact that the derivatives X_u, Y_v, M_u, and L_v were not identified correctly because of degraded coherence at low frequencies. To correct this problem, those parameters were identified separately as discussed in Ref. 79. For this purpose, the following transfer functions were used for the identification[79, 86]:

$$\frac{\dot{v}}{p}(s) = \frac{g}{s - Y_v} \tag{5.9}$$

$$\frac{\dot{u}}{q}(s) = \frac{-g}{s - X_u} \tag{5.10}$$

With this approach, the derivatives X_u and Y_v were identified directly. However, the values that were identified are relatively higher than the usual values for these derivatives as shown in Table 6. Also shown in Table 6 are values for M_u and L_v when $\dot{u}$ and $\dot{v}$ were used in the overall identification instead of N_x and N_y.

An average cost function of 35 was achieved for both forward and hovering flight conditions, which falls within the guideline of $J \leq 100$. The cost functions achieved are better than the cost functions usually achieved for full-scale helicopters.

Table 5: Identified Parameters for the Raptor 50

Derivatives	Hover			Forward-Flight		
	Parameter Value	C.R.%	Insens. %	Parameter Value	C. R. %	Insens.%
τ_f	0.046	23.2	2.176	0.027[c]	-	-
τ_s	0.084	14.86	1.494	0.076	17.76	1.457
X_u	-0.154	9.395	2.981	-0.120	7.646	3.230
X_v	-0.0009[c]	-	-	0.000[b]	-	-
X_{a_1}	-32.170[a]	-	-	-32.170[a]	-	
Y_u	0.0009[c]	-		0.000[b]	-	-
Y_v	-0.115	10.840	3.341	-0.116	7.832	3.348
Y_{b_1}	32.170[a]	-	-	32.170[a]	-	-
Z_w	-1.406	14.180	6.604	-1.324	36.46	17.98
L_u	0.003[c]	-	-	0.000[b]	-	-
L_v	-0.1579[c]	-	-	-1.489[c]	-	-
L_{b_1}	735.500	5.174	2.066	652.6	9.386	4.335
$L_{f_{b_{1_s}}}$	0.870[a]	-	-	0.87[a]	-	-
M_u	0.012[c]	106.2	39.34	0.535[c]	-	-
M_v	0.0012[c]	-	-	0.304	34.21	10.27
M_{a_1}	228.000	8.698	2.551	324.9	8.319	3.448
$M_{f_{a_{1_s}}}$	0.870[a]	-	-	0.87[a]	-	-
N_v	0.000[b]	-	-	0.000[b]	-	-
N_p	-0.133[c]	-	-	0.000[b]	-	-
N_r	-1.070	17.330	8.209	-10.230	14.500	3.448
$Z_{\delta_{col}}$	-8.611	4.255	1.982	-9.015	4.585	2.262
$L_{f_{\delta lat}}$	0.009	29.76	5.160	0.0066	45.82	6.849
$L_{f_{\delta_{lon}}}$	0.0032	8.998	2.398	0.000[b]	-	-
$L_{s_{\delta_{lat}}}$	0.0331	14.330	1.849	0.0281	25.67	2.0799
$M_{f_{\delta_{lon}}}$	0.0173	28.340	2.802	0.01	68.42	4.473
$M_{f_{\delta_{lat}}}$	0.00258	9.709	2.864	0.000[b]	-	-
$M_{s_{\delta_{lon}}}$	0.0188	36.29	3.291	0.02918	36.83	1.879
$N_{\delta_{ped}}$	11.780	4.525	2.075	41.10	12.79	2.497

[a]Fixed value in the model. [b]Eliminated during model structutre determination. [c]Theoretical Values.

Table 6: Speed Derivatives Identified using $\dot{u}$ and $\dot{v}$ Equations

Derivative	Hover	Forward Flight
X_u	-3.263	-3.437
Y_v	-6.089	-3.799
M_u	1.390	0.639
L_v	-1.473	-0.610

In Figure 39, a frequency response comparison between the identification results and flight data are presented for the hovering flight condition. It is seen that there is a good agreement between the flight data and the identification results for both the on- and off-axes responses.

During model development and simulation, it was observed that the addition of the rotor flapping and the stabilizer dynamics resulted in predicted responses that showed a high correlation with the flight data. The discrepancies that were observed in the prediction by the 6-DoF model[29] have disappeared. One of the major discrepancies in the 6-DoF model prediction was in the off-axes responses both in the roll and the pitch axes. The present model predicts the off-axes responses in the same direction as the flight data. The discrepancy seen in the roll rate-to-longitudinal cyclic response in Figure 39 is due to the low coherence data available for that frequency response pair.

The model has also captured the lightly damped rotor-fuselage mode that the 6-DoF model was unable to predict. The lightly damped rotor-fuselage mode in small-scale helicopters is due to the presence of the stabilizer bar. Explicit modeling of the stabilizer bar dynamics has increased the overall fidelity of the model.

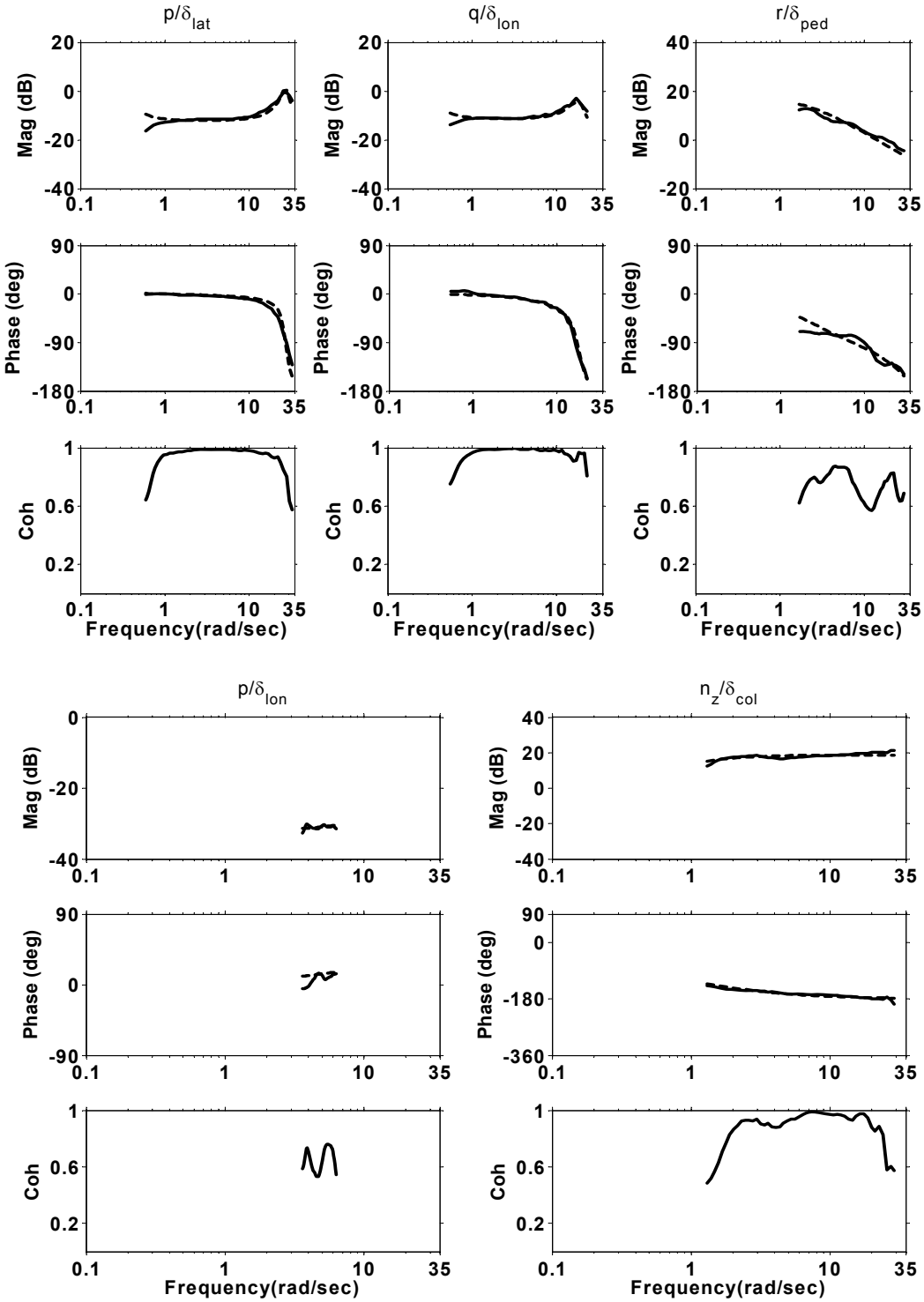

Figure 39: Frequency Domain Comparison of the Identified Model (Dashed) with Flight Data (Solid) for Hovering Flight

Figure 40 presents a frequency-domain comparison between the flight data and the identification results for a forward flight condition. Again, the model predictions compare very well with the flight data.

The derivatives in Table 6 resulted in a better match with the flight data both in the time and frequency domain. However, the derivatives have higher values than are usually expected and do not compare closely with the theoretical values. This discrepancy is partly due to the use of accelerations in the identification. This discrepancy will disappear when velocities are measured directly and used for the identification. This requires the use of GPS or air data sensors in the sensor package. This is left for future work.

A time domain comparison of the identification results with the flight data is presented in Figure 41 for the hovering flight condition. It is seen that both the on- and off-axes responses show a high degree of correlation with the flight data. The speed derivatives used for this comparison were taken from Table 6. Figure 42 presents the time domain verification of the identified model for a forward flight at a velocity of 30 ft/sec. Again, it is seen that the model response matches very well with the flight data.

Figure 41 and Figure 42 show the time domain verification of the model with frequency sweep flight data. However, for the verification purpose, the usual practice is to compare the model response and the flight data with inputs that are of different shapes from the inputs used for the model identification.

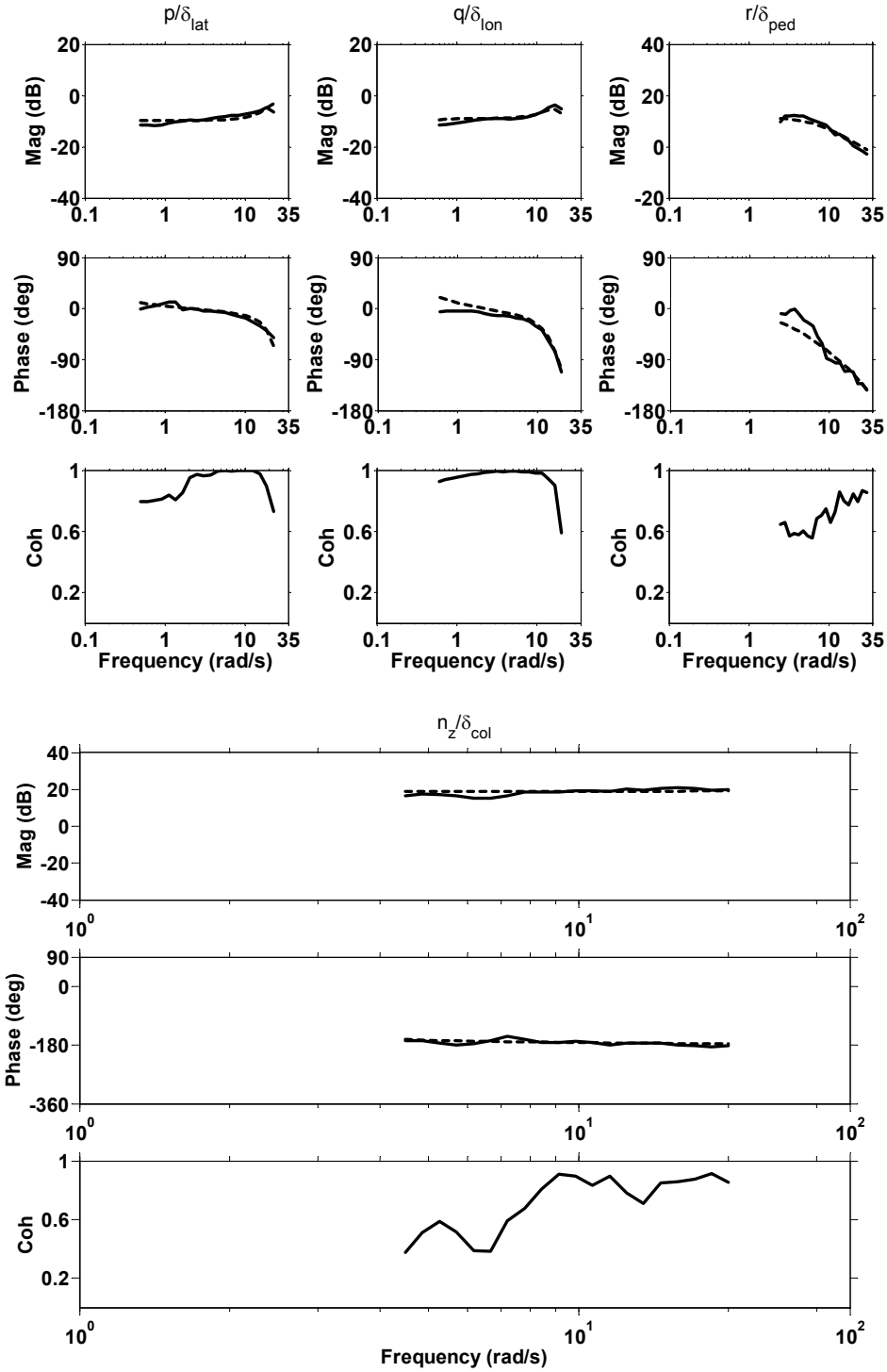

Figure 40: Frequency Domain Comparison of the Identified Model (Dashed) with Flight Data (Solid) for Forward Flight (30 ft/sec)

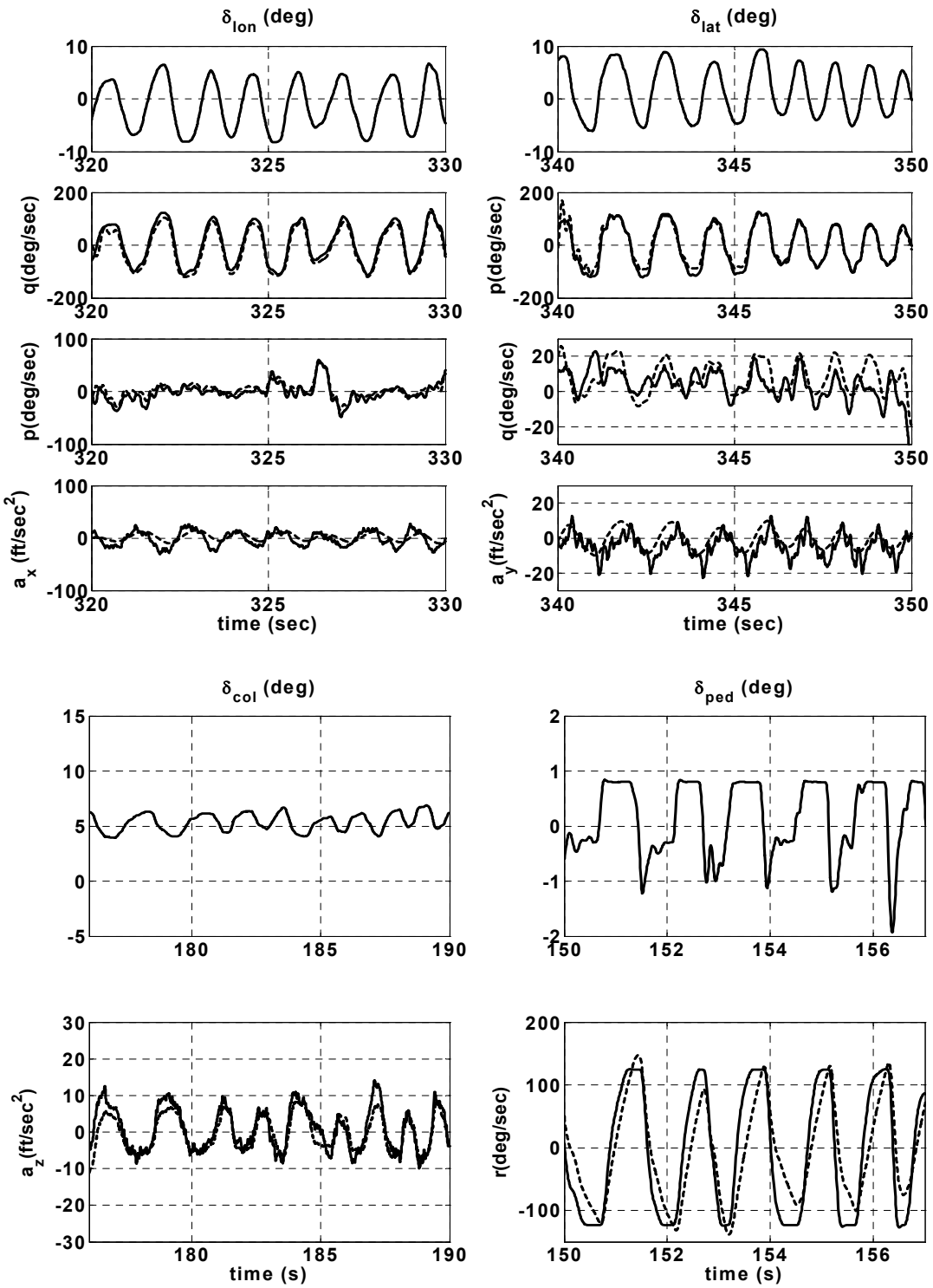

Figure 41: Time Domain Comparison of the Identified Model (Dashed) with Flight Data (Solid) for Hovering Flight

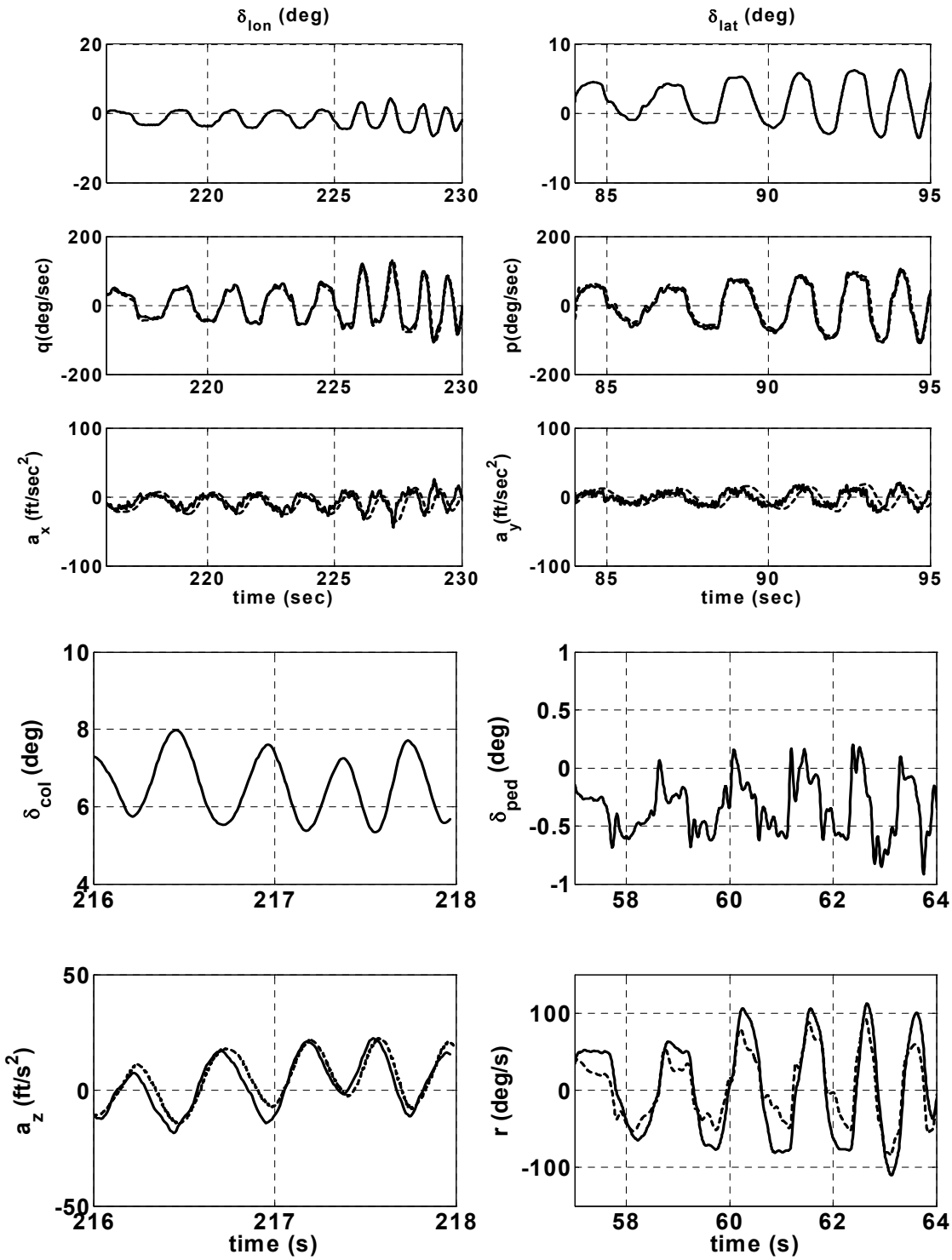

Figure 42: Time Domain Comparison of the Identified Model (Dashed) with Flight Data (Solid) for Forward Flight (30 ft/sec)

Figure 43 and Figure 44 and show the time-domain comparison of the model prediction with the flight data for hovering and forward flight conditions with input shapes other than the sweep inputs.

For the time-domain verification, a number of flight tests were carried out. In Figure 41 and Figure 42, the data used for the verification are the frequency sweep test data. The similar data were used for the model identification. The data used in Figure 43 and Figure 44 came from verification flight tests in which doublet inputs were used. Appendix E lists all the flight data files that were used for the model verification.

5.4 Analytical vs. Identified Models

Table 7 lists the identified and the theoretically calculated derivatives. A close look at Table 7 shows that most of the identified derivatives agree closely with the theoretical values.

The identified rotor and stabilizer bar time constants, τ_f and τ_s, agree very well with the theoretical values for hovering flight. However, for forward flight, τ_f was held fixed to its theoretical value during identification. This value must be held fixed or the identification algorithm does not converge.

The identified roll and pitch rotor spring derivatives, M_{a_1} and L_{b_1}, compare well with the theoretical values. The theoretical values are slightly under-predicted. However, the simulation shows that both the models capture the key rotor dynamics.

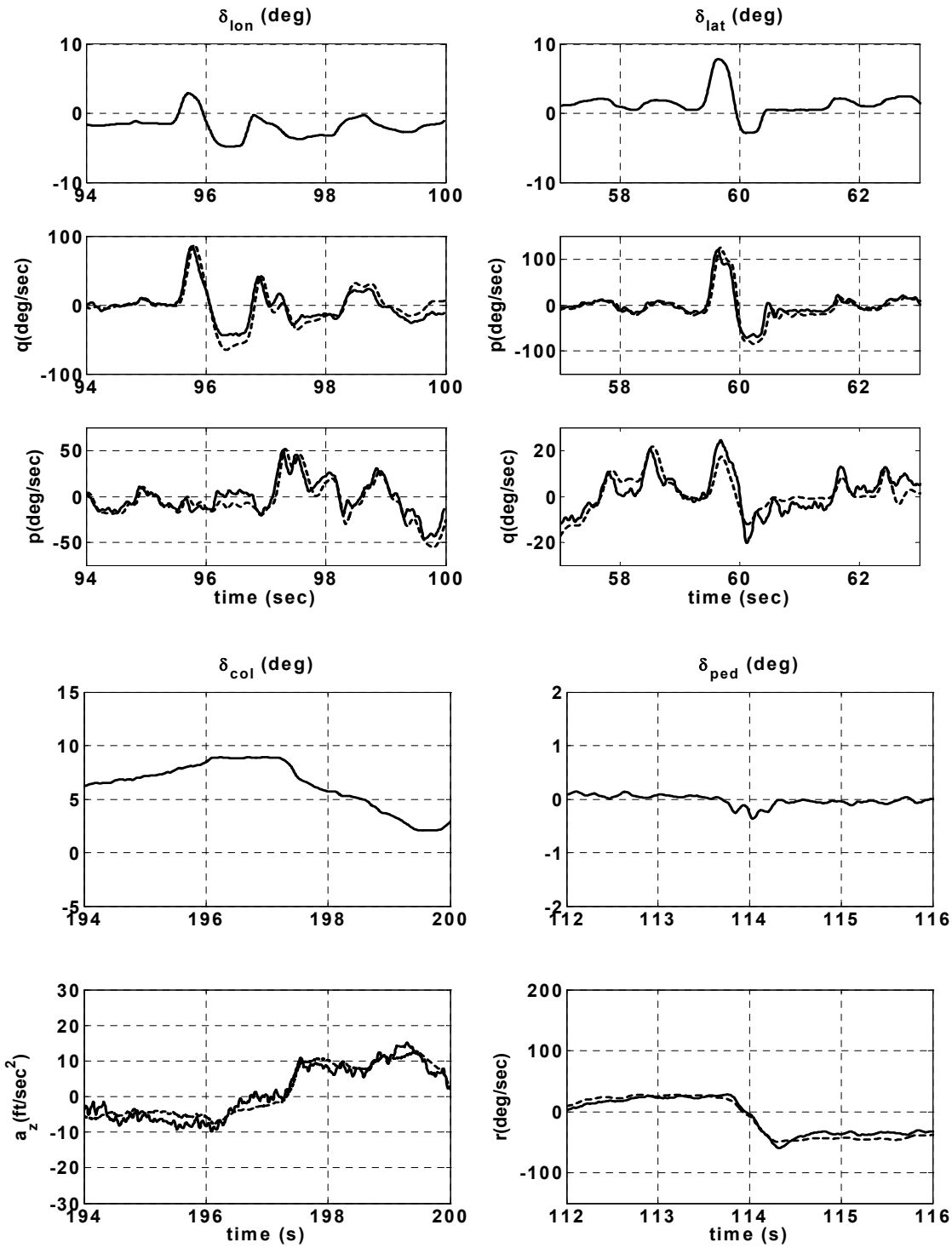

Figure 43: Time-Domain Verification of the Identified Model (Dashed) with Flight Data for Hovering Flight (Different Input Shapes)

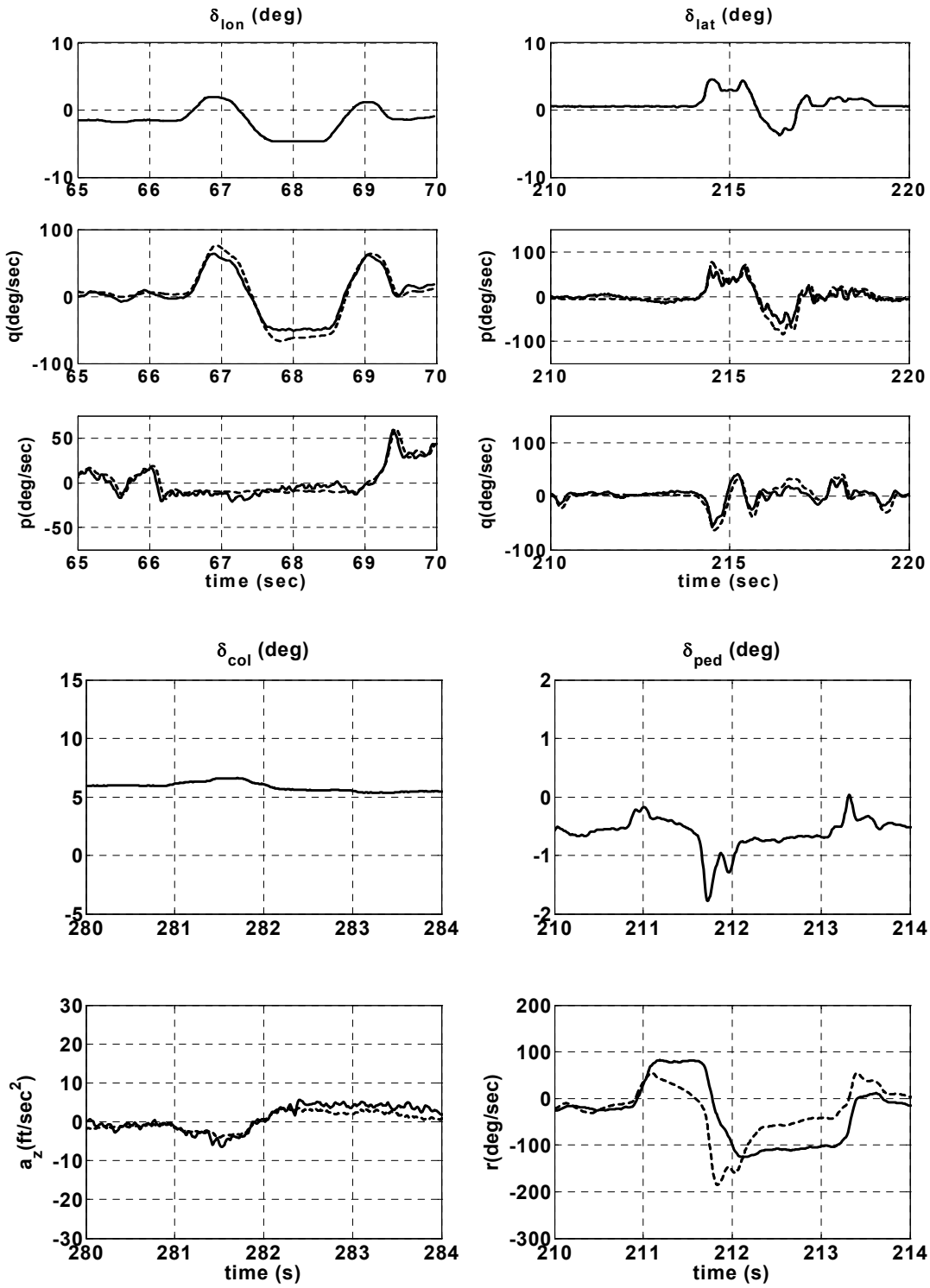

Figure 44: Time-Domain Verification of the Identified Model (Dashed) wit Flight Data for Forward Flight at 30 ft/sec (Different Input Shapes)

Table 7: Identified and Theoretical Parameters for the Raptor 50

	Hover		Forward-Flight	
Derivatives	**Identified**	**Theoretical**	**Identified**	**Theoretical**
τ_f	0.046	0.0274	0.0270	0.0274
τ_s	0.084	0.107	0.076	0.107
X_u	-0.154	-0.009	-0.120	-0.399
X_v	-0.0009	-0.0013	0.000	0.0785
X_{a_1}	-32.170	-32.170	-32.170	-32.170
Y_u	0.0009	0.0013	0.000	0.0027
Y_v	-0.115	-0.125	-0.116	-0.6263
Y_{b_1}	32.170	32.170	32.170	32.170
Z_w	-1.406	-0.890	-1.324	-1.324
L_u	0.003	0.00438	0.000	0.000[b]
L_v	-0.1579	-0.157	-1.489	-1.891
L_{b_1}	735.500	602.09	652.6	602.9
$L_{f_{b_{1_s}}}$	0.870	0.870	0.87	0.870
M_u	0.012	0.012	0.535	0.535
M_w	0.000	0.000	0.000	0.0679
M_v	0.0012	0.0017	0.304	-0.1026
M_{a_1}	228.000	238.640	324.9	238.640
$M_{f_{a_{1_s}}}$	0.870	0.870	0.000	0.870
N_v	0.000	0.000	0.000	0.000
N_p	-0.133	-0.133	0.000	-0.18058
N_r	-1.070	-1.356	-10.230	-1.8357
$Z_{\delta_{col}}$	-8.611	-13.039	-9.015	-13.039
$L_{f_{\delta lat}}$	0.009	0.011	0.0066	0.011
$L_{f_{\delta_{lon}}}$	0.0032	0.000	0.000	0.000
$L_{s_{\delta_{lat}}}$	0.0331	0.0118	0.0281	0.0118
$M_{f_{\delta_{lon}}}$	0.0173	0.011	0.01	0.011
$M_{f_{\delta_{lat}}}$	0.00258	0.000	0.000	0.000
$M_{s_{\delta_{lon}}}$	0.0188	0.0118	0.02918	0.00118
$N_{\delta_{ped}}$	11.780	7.528	41.10	8.0634

The identified speed damping derivatives (X_u and Y_v) have the same sign as the theoretical values. However, the theoretical values are somewhat under-predicted. When compared with the flight data, both the theoretical and the identified models showed reduced speed damping, while the flight data showed well-damped speed characteristics. To correct this problem, the speed damping derivatives were identified separately using the hover trim conditions as discussed earlier in section 5.3. The identified derivatives resulted in good correlation with the flight data.

The identified speed stability derivatives (M_u and L_v) have higher values than the theoretical values, particularly for hovering flight. This is due to the fact that the available data has low coherence at lower frequencies. This problem can be solved by using trim data collected during static stability tests as discussed in Refs. 79 and 89 in which the control gradients $\Delta\delta_{lon}/\Delta u$ and $\Delta\delta_{lat}/\Delta v$ are determined using trim data. The control gradients can later be used for the calculation of M_u and L_v using the following formulas[79, 89]:

$$M_u = -M_{\delta_{lon}}\left(\frac{\Delta\delta_{lon}}{\Delta u}\right) + M_w \frac{Z_u}{Z_w} \tag{5.11}$$

$$L_v = -L_{\delta_{lat}}\left(\frac{\Delta\delta_{lat}}{\Delta v}\right) + L_{\delta_{ped}}\left(\frac{\Delta\delta_{ped}}{\Delta v}\right) \tag{5.12}$$

For the forward flight, the identified derivatives are identical to the theoretical values.

The off-axes speed derivatives X_v, Y_u, M_v, L_u, and M_w could not be identified accurately because of the low coherence in the off-axes response data. During the

identification of the model, theoretical values were used for these parameters and held fixed.

The identified heave-damping derivative (Z_w) and the heave control sensitivity (Z_{col}) compare very well with the flight data. The simulation comparison with the flight data shows that both the identified and theoretical models are able to predict the helicopter vertical dynamics very well.

The identified yaw dynamics derivatives (N_r and N_{ped}) have similar magnitudes to the theoretical values in hover. However, for the forward flight, the theoretical values are under-predicted. Both the identified and theoretical models showed good correlation with the flight data in both the time- and frequency-domains.

The directional stability derivative (N_v) could not be identified because of low coherence data. When the theoretically calculated value was used, the yaw rate prediction departed significantly from the flight data. To correctly identify this parameter, flight tests should be carried out by maintaining a constant sideslip as discussed in Ref. 89. This would allow measurement of the control gradient $\Delta\delta_{ped}/\Delta v$, which can be used for the calculation of N_v using the following formula:

$$N_v = -N_{\delta_{ped}}\left(\frac{\Delta\delta_{ped}}{\Delta v}\right) \tag{5.13}$$

However, as discussed in Ref. 79, the control gradients $\Delta\delta_{lon}/\Delta u$, $\Delta\delta_{lat}/\Delta v$, and $\Delta\delta_{ped}/\Delta v$ are very difficult to obtain with high precision. This is particularly true for

UAV helicopters. Furthermore, the current sensor package measures accelerations, which are then integrated to calculate the velocities. This will pose problems when calculating Δu and Δv precisely.

Overall, the identified parameters compare very well with the theoretically calculated parameters. Some of the parameters (X_u, Y_v, M_u, L_v, N_v, et cetera) could not be identified accurately. This is because of the low coherence data available for these parameters. This provides an indication that the analytical and parameter identification techniques complement each other.

5.4.1 Eigenvalues and Modes

Eigenvalues carry important information about the stability of the modes present within a dynamic system. Not only do they provide information on the absolute stability of a system, they can also provide information on the relative stability of the system.

Table 8 compares the theoretical and identified eigenvlaues of the different modes for the hovering and forward flight conditions.

It is seen that both flight conditions have similar pole locations. However, the eigenvalues for the directional dynamics in hover and forward flight conditions are somewhat separated in scale. The table shows the eigenvalues in $[\zeta \quad \omega]$ form for the second-order modes and in (σ) form for the first-order modes, where σ corresponds to the denominator $(s+\sigma)$. The pole locations for the pitch-flap-stabilizer modes for

both flight conditions agree with the frequency values that are seen in the frequency response plots.

Table 8: Eigenvalues of the Raptor 50 for Key Modes in Hover and Forward Flight Conditions

	Hover		Forward-Flight	
Modes	**Identified**	**Theoretical**	**Identified**	**Theoretical**
Pitch	[0.641, 0.119]	[0.16, 0.12]	(0.24)	[0.212, 0.76]
Roll	[0.235, 0.241]	[0.24, 0.263]	(0.116)	(0.259)
Heave	(1.406)	(0.89)	(1.324)	(1.89)
Pitch/Flap/Stab	[0.249, 16.6]	[0.244, 16.0]	[0.337, 18.0]	[0.245, 15.9]
Roll/Flap/Stab	[0.107, 28.7]	[0.186, 26.2]	[0.263, 25.9]	[0.187, 26.2]
Yaw	(1.07)	(1.36)	(10.2)	(1.84)
Uniform Inflow	(62.2)	(63.1)	(67.5)	(40.4)
Coning	[0.195, 187]	[0.195, 187]	[0.195, 187]	[0.195, 187]

5.5 Raptor 50 vs. X-Cell Helicopters

As discussed earlier, no work exists in the open literature on the high-order dynamics modeling of a helicopter of the size of the Raptor 50. However, some work has been done on the X-Cell helicopter that is closest to the Raptor 50 in and weight and size. The X-Cell helicopter was used by MIT for its research on autonomous and acrobatic helicopters. Though, a complete list of derivatives was not found in the literature, some of the derivatives representing the attitude dynamics of the X-Cell helicopter were found.

Table 9 shows a comparison of key identified parameters for the Raptor 50 with those of the X-Cell helicopter for a hovering flight condition. It is clear from the table that the Raptor 50's roll- and pitch-flap dynamics are at higher frequencies than those of the X-Cell. The natural frequencies of the coupled rotor fuselage modes are given

by the following expressions:

$$\omega_{roll-flap} = \sqrt{L_{b_1}} \tag{5.14}$$

$$\omega_{pitch-flap} = \sqrt{M_{a_1}} \tag{5.15}$$

This is an indication that the Raptor 50 is more agile than the X-Cell helicopter.

Table 9: Comparison of Key Parameters with the X-Cell Helicopter

Derivative	Raptor 50	X-Cell
τ_f	0.046	0.052
τ_s	0.084	0.220
L_{b_1}	735.500	320.000
$L_{f_{a_1}}$	0.000	0.000
$L_{f_{b_{1_s}}}$	0.870	1.150
M_{a_1}	228.800	204.000
$M_{f_{b_1}}$	0.000	0.000
$M_{f_{a_{1_s}}}$	0.870	1.150
$L_{f_{\delta_{lat}}}$	0.2609	0.420
$L_{f_{\delta_{lon}}}$	0.0585	0.000
$L_{s_{\delta_{lat}}}$	0.3133	0.110
$M_{f_{\delta_{lon}}}$	0.1978	0.53
$M_{f_{\delta_{lat}}}$	0.0557	0
$M_{s_{\delta_{lon}}}$	0.3393	0.11

6 Summary and Conclusions

A 14-DoF, 17 state simulation model of the Raptor 50 helicopter has been developed from the first-principles for hovering and forward flight conditions. The model includes the fuselage, rotor flapping, rotor inflow, and stabilizer bar degrees-of-freedom. The fuselage and the rotor dynamics were coupled using the hybrid model formulation, in which the coupling was achieved through the flapping derivatives (or the rotor spring terms) X_{a_1}, Y_{b_1}, M_{a_1}, L_{b_1}. Also considered are the coupled heave-coning-inflow dynamics.

The theoretically developed model gave helpful insight into the magnitude and sign of the stability and control derivatives. This assisted the model development process by providing initial values for the derivatives within the CIFER parameter identification process. A 12-DoF, 15-state simulation model was developed using CIFER for the hovering and forward flight conditions. The lateral and longitudinal inflow dynamics were not included within the identified model structure as the inflow velocities cannot be measured using existing techniques. The theoretically developed and the identified models compared very well except for the speed stability derivatives (M_u, L_v). Also, the directional stability derivative (N_v) could not be identified because of low coherence data. When the theoretically calculated value of N_v was used, the simulated yaw rate did not compare well with the flight data. Those derivatives (M_u, L_v, and N_v) should be identified separately using trim data as discussed in Ref. 79 and 89. As discussed in Ref. 89, static stability flight tests have

to be carried out to measure the trim data, which will allow the determination of the control gradients ($\Delta\delta_{lon}/\Delta u$, $\Delta\delta_{lat}/\Delta v$, and $\Delta\delta_{ped}/\Delta v$) required for the calculation of the speed stability derivatives. However, due to difficulty in correctly measuring trim data, especially for UAV helicopters, these derivatives cannot be determined with high precision. Moreover, the current sensor package measures only accelerations. The velocities are obtained by integrating these accelerations, which results in error. In order to determine the control gradients accurately, the velocities must be measured directly using either GPS or air data sensors. This is left for future work. If the velocities are measured directly, high-order models for UAV helicopters can be developed rapidly using parameter identification techniques. This dissertation has laid a foundation for rapid identification of these models.

The simulation results showed a high degree of correlation with the flight data in both the frequency and time-domains for on-axis pitch and roll rate responses. These were seen to compare very well with the flight data up to frequencies of 20 and 30 rad/sec, respectively. The models were able to capture the second order effects due to rotor-fuselage coupling seen in the flight data. The time domain comparison showed that the models, which included the stabilizer bar, were able to capture the lightly damped modes, which are due to the presence of the stabilizer bar.

The model prediction for the on-axis yaw response compares very well with the flight data in the frequency-domain. In the time-domain, there is a slight disagreement between the model prediction and the flight data. However, this disagreement is

insignificant.

The frequency domain comparison for the vertical acceleration due to the collective input gave a very good correlation with the flight data for a wide range of frequencies (1-30 rad/sec). This is considered important because the inflow dynamics come into effect within this frequency range. The model prediction was also seen to compare very well with the flight data in the time-domain. However, the off-axes responses in the frequency domain have a limited range of accuracy. This is because of the low coherence for these responses over most of the frequency range.

The theoretical model included the three-state rotor inflow dynamics. Also considered was the dynamic wake correction factor. However, when the inflow dynamics were added to the model, there were no significant differences in the model predictions. This leads to the conclusion that the inflow dynamics do not have a pronounced effect on small-scale helicopter dynamics and can be neglected.

Overall, the high-order model compared very well with the flight data. This research provides the tools required for the design of high-bandwidth control systems for helicopters using various control system design techniques.

This work presents the theoretically calculated and the parameter identified models for the Raptor 50 helicopter. The models can readily be used by anyone working on the Raptor 50 V2 helicopter for simulation and control system design purposes without further model development.

7 Future Work and Recommendations

The high-order model developed within this dissertation included the rotor flapping and inflow dynamics and resulted in a very good match with the flight data. However, the present work has neglected the lag degrees-of-freedom. In the future, the effect of lead-lag dynamics should be investigated and the order of the model increased to include lead-lag dynamics.

The flight envelope for the helicopter includes different operating conditions. Helicopters can hover and possess the capability for slow and fast forward speeds. Small-scale helicopters, on the other hand, are more agile and can attain higher attitude rates and angles than their full-scale counterparts. These vehicles can easily be operated to exceed flight conditions where the small-perturbation assumption is valid. Therefore, a nonlinear model is needed to describe their full operating envelope including nap-of-the-earth missions.

This work has made it possible to fully understand the complexities of helicopter dynamics modeling. Also, a very accurate dynamics model for a UAV helicopter has been developed. This model, and the knowledge gained during this study, will be used in the design of control systems using various control system design techniques. Specifically, future work should focus on the following:

- Implementation of linear and nonlinear robust control systems using H_∞ and $\mu - synthesis$ techniques
- Research on intelligent controllers using Neural Networks and Fuzzy

Logic techniques

- Research on vision guidance systems for obstacle avoidance

In order to have more accurate identification, the weight of the sensor package needs to be as low as possible. The current sensor package should be replaced with newer MEMS (Micro Electro Mechanical Sensors) based sensors. Also, the current battery package should be replaced with lighter lithium polymer batteries.

To estimate the speed damping and stability derivatives, the present work used measured accelerations. The accelerations were integrated to obtain the velocities. If the velocities could be measured directly, the identification would be more accurate. The author suggests the use of GPS sensors for this purpose in future projects. The possibility of using optical or air data sensors should also be investigated. Once the velocities are measured directly, the methods discussed in Refs. 79 and 89 for the calculation of these derivatives should be followed.

References

1. Nelson, Robert C. *Flight Stability and Automatic Control,* McGraw Hill, Boston, Massachusetts, 1998.
2. Bramwell, Balman, and Done. *Bramwell's Helicopter Dynamics,* Washington DC: American Institute of Aeronautics and Astronautics, 2001.
3. Padfield, Gareth. *Helicopter Flight Dynamics: The Theory and Application of Flying Qualities and Simulation Modeling*, American Institute of Aeronautics and Astronautics, Washington D.C., 1996.
4. Kim, F. D., Roberto Celi, and Tischler, M. B. *High-Order State Space Simulation Models of Helicopter Flight Mechanics*. Journal of American Helicopter Society, October 1993.
5. Bhandari, Subodh., Kowalchuk, Scott., Lederbogen, P., and Colgren, Richard. *Six-DoF Dynamic Modeling and Flight Testing of a UAV Helicopter,* AIAA Modeling and Simulation Technologies Conference and Exhibit, 15-18 August., 2005, San Francisco, California.
6. Miller, R. H., *A Method for Improving the Inherent Stability and Control Characteristics of Helicopters,* Journal of Aeronautical Sciences, June 1950.
7. Ellis, C. W., *Effects of Articulated Rotor Dynamics on Helicopter Automatic Control System Requirements,* Aeronautical Engineering Review, July 1953.
8. Hall, W. E. Jr. and Bryson, A. E. Jr., *Inclusion of Rotor Dynamics in Controller Design,* Journal of Aircraft, Vol. 10, April 1973.

9. Chen, R. T. N. and Hindson, W. S., *Analytical and Flight Investigation of the Influence of Rotor and Other High-Order Dynamics on Helicopter Flight Control System Bandwidth,* NASA TM 85596, 1985.

10. Mettler, Bernard. *Identification Modeling and Characteristics of Miniature Rotorcraft,* Kluer Academic Publisher, Norwell, Massachusetts, 2003.

11. Prouty, Raymond W., *Helicopter Performance, Stability and Control*, Krieger Publishing Company, Malabar, Florida, 1995.

12. E. Johnson and S. Kannan, *Adaptive Flight Control for an Autonomous Unmanned Helicopter,* AIAA Guidance, Navigation, and Control Conference and Exhibit, Monterey, California, August 5-8, 2002.

13. Mettler, B., Tischler, M. B., and Kanade, T. *System Identification Modeling of a Small-Scale Unmanned Rotorcraft for Flight Control Design,* Journal of the American Helicopter Society, January 2002.

14. Gavrilets, Mettler, and Feron, *Non-Linear Model for a Small-Size Aerobatic Helicopter,* AIAA Guidance, Navigation, and Control Conference and Exhibit, Montreal, Canada, August 6-9, 2001.

15. V. Gavrilets, I. Martinos, B. Mettler and E. Feron. *Control Logic for Automated Aerobatic Flight of a Miniature Helicopter,* AIAA Guidance, Navigation, and Control Conference and Exhibit, Monterey, California, August 5-8, 2002.

16. Cheng, Rendy P., Tischler, M. B., and Schulein, Greg J. *R-MAX Helicopter State-Space Model Identification for Hover and Forward Flight,* Journal of American

Helicopter Society, April 2006.

17. CIFER-*Comprehensive Identification from FrEquency Responses*, Army/NASA Flight Control and Cockpit Integration Branch, January 25, 2004. http://uarc.ucsc.edu/flight%2Dcontrol/cifer/.
18. Jategaonkar, R. and Plaetschke, E. *Maximum Likelihood Parameter Estimation from Flight Test Results for General Nonlinear Systems,* DFVLR-FB 83-14, 1983.
19. Tischler, M. B. and Cauffman, Mavis G. *Frequency-Response Method for Rotorcraft System Identification: Flight Applications to BO 105 Coupled Rotor/Fuselage Dynamics,* Journal of American Helicopter Society, July 1992.
20. Johnson, Wayne. *Helicopter Theory*, New York, Dover Publications, 1980.
21. Howlett, J. J. *UH-60A Black Hawk Engineering Program: Volume I-Mathematical Model,* NASA CR-166309, 1981.
22. Kapilta, T. T., Driscoll, J. T., Diftler, M. A., and Wong, S. W. *Helicopter Simulation Development by Correlation with Frequency Sweep Flight Test Data,* American Helicopter Society, 45th Annual Forum, Boston, Massachusetts, May 1989.
23. Kim, F. D. *Formulation and Validation of High-Order Mathematical Model of Helicopter Flight Dynamics,* Ph. D. Dissertation, Department of Aerospace Engineering, University of Maryland, College Park, MD, September 1991.
24. Diftler, M. A., *UH-60A Helicopter Stability Augmentation Study,* Fourteenth European Rotorcraft Forum, Milano, Italy, September 1988.

25. Ballin, M. G. and Dalang-Secretan, Marie-Alix. *Validation of the Dynamic Response of a Blade-Element UH-60 Simulation Model in Hovering Flight.* Journal of American Helicopter Society, October, 1991.

26. Ballin, M. G. *Validation of a Real-Time Engineering Simulation of the UH-60A Helicopter,* NASA TM-100991, 1988.

27. Talbot, Peter. D. et al. *A Mathematical Model of a Single Main Rotor Helicopter for Piloted Simulation,* NASA TM 84281, 1982.

28. Scharge, D. P et al. *Helicopter Stability and Control Modeling Improvements and Verification on Two Helicopters,* Fourteenth European Rotorcraft Forum, Milano, Italy, Sept 1988.

29. Zhao, Xin and Curtiss, H. C. *A Linearized Model of Helicopter Dynamics Including Correlation with Flight Test,* Second International Conference on Rotorcraft Basic Research, University of Maryland, College Park, MD, February 1988.

30. *MACSYMA Reference Manual*, The Mathlab Group Laboratory for Computer Science, MIT, January 1983.

31. Curtiss, H. C. Jr. *Stability and Control Modeling,* Vertica, Vol. 12, No. 4, 1988.

32. Curtiss, H. C. Jr. and Shupe, N. K. *A Stability and Control Theory for Hingeless Rotors,* American Helicopter Society, 27th Annual Forum, May 1971.

33. Hansen, R. S. *Towards a Better Understanding of Helicopter Stability Derivatives,* Journal of American Helicopter Society, January 1984.

34. McKillip, Robert Jr. and Curtiss, H. C. *Approximations for Inclusion of Rotor Lag Dynamics in Helicopter Flight Dynamics Models,* Seventeenth European Rotorcraft Forum, Berilin, Germany, September 1991.

35. Chen, R. T. N. et al. *Application of Conjugate Gradient Method to the Estimation of VTOL Aircraft Parameter and State,* JACC Preprint, 1970.

36. Gilyard, G. B. *Flight Determined Derivatives and Dynamic Characteristics of the CV-990 Airplane,* NASA TN D-6777, May 1972.

37. Molousis, J. A. *Helicopter Stability Derivative Extraction and Data Processing using Kalman Filtering Techniques,* American Helicopter Society, 28th Annual National Forum, Washington D. C., May 1972.

38. Molusis, J. A. *Helicopter Stability Derivative Extraction from Flight Data Using the Baysian Approach to Estimation,* Journal of American Helicopter Society, April 1973.

39. Duval, Ronald W. and Mackie, David B. *Identification of a Linear Model of Rotor-Fuselage Dynamics from Nonlinear Simulation Data,* Vertica, Vol. 5, 1981.

40. Fu, Kuang-Hua and Kaletka, Juergen. *Frequency-Domain Identification of BO 105 Derivative Models with Rotor Degrees of Freedom,* Journal of American Helicopter Society, January 1993.

41. Aponso, Bimal L. et al. *Identification of High-Order Helicopter Dynamics Using Linear Modeling Methods,* Journal of American Helicopter Society, July 1994.

42. Fletcher, J. W. *Identification of UH-60 Stability Derivative Models in Hover from*

Flight Test Data, Journal of the American Helicopter Society, January 1995.

43. Tischler, Mark B. and Tomashofski, Chris A. *Flight Test Identification of SH-2G Flapped-Rotor Helicopter Flight Mechanics Models,* Journal of American Helicopter Society, January 2002.
44. Kaletka, J. and von Grunhagen, W. *Identification of Mathematical Derivative Models for the Design of a Model Following Control System,* 45th Annual National Forum of the American Helicopter Society, Boston, May 1989.
45. Tischler, Mark B. *System Identification Requirements for High-Bandwidth Rotorcraft Flight Control System Design,* Journal of Guidance, Vol. 13, No. 5, September-October 1990.
46. Schroeder, Jeffery A. et al. *Identification and Simulation Evaluation of a Combat Helicopter in Hover,* Journal of Guidance, Control, and Dynamics, Vol. 18, No. 1, Janaury-February 1995.
47. Tischler, M. B. *Identification of Bearingless Main Rotor Dynamic Characteristics from Frequency-Response Wind-Tunnel Test Data,* Journal of the American Helicopter Society, January 1999.
48. Rosen, A. and Isser, A. *A New Model of Rotor Dynamics During Pitch and Roll of a Hovering Helicopter,* Journal of the American Helicopter Society, July 1995.
49. Keller, J. D. *An Investigation of Helicopter Dynamic Coupling Using Analytical Model,* Journal of the American Helicopter Society, October 1996.
50. Keller, J. D. and Curtiss, H. C. *A Critical Examination of the Methods to Improve*

the Off-Axis Response Prediction of Helicopters, American Helicopter Society 54th Annual Forum, Washington D. C., May 20-22, 1998.

51. Mansur, M. Hossein and Tischler, Mark. B. *An Empirical Correction for Improving Off-Axis Response in Flight Mechanics Helicopter Models,* Journal of the American Helicopter Society, April 1998.
52. Schulein, Creg J., Tischeler, Mark B., Mansur, M. Hossein, and Rosen, Aviv. *Validation of Cross-Coupling Modeling Improvements for UH-60 Flight Mechanics Simulations,* Technical Note, Journal of the American Helicopter Society, July 2002.
53. Leishman, J. G. *Modeling of Subsonic Unsteady Aerodynamics for Rotary Wing Applications,* Journal of the American Helicopter Society, January 1990.
54. Civita, Marco La, Messner, William C., and Kanade, Takeo. *Modeling of Small-Scale Helicopters with Integrated First-Principles and System-Identification Techniques,* American Helicopter Society, 58th Annual Forum, Montreal, Canada, June 2001.
55. Kim, S. M. and Tilbury, D. M. *Mathematical Modeling and Experimental Identification of a Model Helicopter,* AIAA Modeling and Simulation Technologies Conference and Exhibit, Boston, MA, August 1998.
56. Cunha, R. and Silvestre, C. *Dynamic Modeling and Stability Analysis of Model-Scale Helicopters With Bell-Hiller Stabilizing Bar,* AIAA Guidance, Navigation, and Control Conference and Exhibit, Austin, Texas, August 2003.

57. Using MATLAB/Simulink. The MathWorks Company, Inc., Natick, Massachusetts, Version 7, 2006.

58. Gadewadikar, J., Lewis, F. L., et al. *H-Infinity Static Output-Feedback Control for Rotorcraft,* AIAA Guidance, Navigation, and Control Conference and Exhibit, August 21-24, 2006, Keystone, Colorado.

59. Chung, Wang-Wen. *Flight Attitude Simulation Model for a Helicopter,* Master's Thesis, Department of Mechanical Engineering, Yuan Ze University, July 2006.

60. Pritchard, John. *Flight Test Weight and Balance*, Department of Aerospace Engineering, The University of Kansas, 2004.

61. Kowalchuk, Scott A. *UAV Longitudinal Dynamics and Flight Testing of a Raptor 50 V2 Helicopter,* Master's Thesis, The University of Kansas, August 2004.

62. Chen, R. T. N. *Effect of Primary Rotor Parameters on Flapping Dynamics,* NASA TP-1431, January 1980.

63. Gaonkar, G. H., and Peters, D. A. *Review of Dynamic Inflow Modeling for Rotorcraft Flight Dynamics,* Vertica, Vol 12, No 3, 1988.

64. Chen, R. T. N. *A Survey of Nonuniform Inflow Models for Rotorcraft Flight Dynamics and Control Applications,* 15th European Rotorcraft Forum, Amsterdam, September, 1989.

65. Carpenter, P. J. and Fridovitch, B. *Effect of Rapid Blade Pitch Increase on the Thrust and Induced Velocity Response of a Full Scale Helicopter Rotor,* NACA TN 3044, 1953.

66. Pitt, Dale. M. and Peters, David A. *Theoretical Prediction of Dynamic-Inflow Derivatives,* Vertica, Vol. 5, 1981.

67. Peters, D. A., *Hingeless Rotor Frequency Response with Unsteady Inflow,* Rotorcraft Dynamics, NASA SP-352, 1974.

68. Crews, S. T., Hohenemser, K. H., and Ormiston, R. A., *An Unsteady Wake Model for a Hingeless Rotor,* Journal of Aircraft, November 1974.

69. Takahashi, M. D. *A Flight-Dynamic Helicopter Mathematical Model with a Single Flap-Lag-Torsion Main Rotor,* NASA TM 102267, 102267, February 1990.

70. Harding, J. W. and Bass S. M. *Validation of a Flight Simulation Model of the AH-64 Apache Attack Helicopter Against Flight Test Data,* American Helicopter Society, 46th Annual Forum, Washington D. C., May 1990.

71. Keller, J. D. *The Effect of Rotor Motion on the Induced Velocity in Predicting the Response of Rotorcraft,* Ph. D. Thesis, University of Maryland, College Park, MD, January 1980.

72. Chen, Robert T. N. and Hindson, William S. *Influence of Dynamic Inflow on the Helicopter Vertical Response,* NASA Technical Memorandum 888327, June 1986.

73. Houston, S. S. *Identification of Coupled Body/Coning/Inflow Model of Puma Vertical Response in Hover,* Vertica, Vol. 13, No. 3, 1989.

74. Houston, S. S. *Identification of Factors Influencing Heave Axis Damping and*

Control Sensitivity, RAE TR 88047, 1989.

75. Houston, S. S. and Tarttelin, P. C. *Validation of Mathematical Simulations of Helicopter Vertical Response Characteristics in Hover,* Journal of American Helicopter Society, January 1991.
76. Houston, S. S. and Black, C. G. *Identifiability of Helicopter Models Incorporating Higher Order Dynamics,* Journal of Guidance, Control, and Dynamics, Vol 14, No 4, 1991.
77. Tischler, M. B., Leung, Joseph H. M., and Dugan, Daniel C. *Frequency-Domain Identification of XV-15 Tilt-Rotor Aircraft Dynamics in Hovering Flight.* Journal of American Helicopter Society, April 1985.
78. Tischler, Mark B. *Flight Test Manual: Rotorcraft Frequency-Domain Flight Testing,* U.S. Army Aviation Technical Test Center, Edwards AFB, California, September 1995.
79. Tischler, M. B., and Remple, Robert. *Aircraft and Rotorcraft System Identification,* American Institute of Aeronautics and Astronautics, August 2006.
80. Tischler, Mark B. and Cauffman, M. G. *Comprehensive Identification from Frequency Responses (CIFER)*, Volume 1-Class Notes, USAATCOM TR-94-A-017, 1994.
81. Bloomfield, Peter. *Fourier Analysis of Time Series: An Introduction*, John Wiley & Sons, 1976.
82. Rabiner, Lawrence R., Schafer, Ronald W. and Rader, Charles M.*, The Chrip-Z*

Transform Algorithm and its Application, The Bell System Technical Journal, May-June 1969.

83. Bendat, J. S. and Piersol, A. G. *Engineering Applications of Correlation and Spectral Analysis,* John Wiley & Sons, New York, 1993.
84. Tischler, M. B. *Frequency-Response Identification of XV-15 Tilt-Rotor Aircraft Dynamics,* NASA Technical Report TM-89428, Moffett Field, CA, 1987.
85. Maine, R. E. and Iliff, K. W. *Theory and Practice of Estimating the Accuracy of Dynamic Flight-Determined Coefficients,* NASA RP 1077, 1981.
86. McRuer, Duane et al. *Aircraft Dynamics and Automatic Control,* Systems Technology Inc., Hawthorne, California, 1968.
87. Morelli, E. A. and Klein, V. *Accuracy of Aerodynamic Model Parameters Estimated from Flight Test Data,* Journal of Guidance, Control, and Dynamics, Vol. 20, No. 1, 1997.
88. Milne, G. W. *Identification of a Dynamics Model of a Helicopter from Flight Tests,* Ph. D. Dissertation, Stanford University, Department of Aeronautics and Astronautics, CA, December 1986.
89. Cookie, Alastair K. and Fitzpatrick, Eric W. H. *Helicopter Test and Evaluation,* American Institute of Aeronautics and Astronautics, Inc., Reston, VA, 2002.

Appendices

A MATLAB Code for the 14-DoF Model of the Raptor 50 (Hover)

```
function[A,B]=AB_Matrix_raptor_hover_4dof(u,v,w,theta,...

M_Collective_deg,Long_Cyclic_deg,Lat_Cyclic_deg,T_Collective_deg)

%===============
%Main Rotor
%===============
% clc
% clear
rpm=1790;%RPM of the main rotor
Rmr=(52.95/2)/12;%Radius the main blade (ft)
Nb=2;%Number of the blades
c=2.12/12;%Blade chord (ft)
a=4.93;%3-D lift curve slope (1/rad)
cd=0.019;%Profile drag coefficient
Ib=2.21447/144;%Main rotor blade flap inertia(slugs ft^2)
H_mr=9.1/12;%Height of hub above c.g. (ft)
L_mr=-0.25/12;%Distance forward of c.g. from hub (ft)
y_mr=0;%Lateral distance from the c.g to the main rotor hub (ft)
theta1=0/57.3;%Blade twist angle (rad)a
gamma_s=0;%Main rotor shaft angle (rad)
i_m=0;%Main rotor shaft incidence
x_cg=-0.25/12;%Center of gravity relative to heli nose (ft)
i_s=0;%Shaft incidence
H=H_mr/Rmr;
L=L_mr/Rmr;
omega=rpm*(2*pi/60);
omegaR=omega*Rmr;
Sb=0.22*3.33^2;%Fuselage side area (ft^2)
U0=0;
sigma=Nb*c/(pi*Rmr);%Main rotor solidity ratio
A=pi*Rmr^2;%Tail rotor disc area
Ab=Nb*c*Rmr;%Blade area (ft^2)
lambda_beta=1.05;%Flapping Frequency Ratio

%================
%Tail Rotor
%================
rpm_T=8.5*rpm;%Tail rotor rpm
c_t=1.06/12;%Tail rotor chord (ft)
Rtr=(9.26/2)/12;%Radius of the tail rotor (ft)
L_tr=30.92/12;%Tail rotor moment arm (ft)
H_tr=3.04/12;%Vertical distance of tail rotor hub from c.g(ft)
a_tr=4.7;%3-D lift curve slope of tail rotor (1/rad)
alfa_to=0*pi/180;%No lift setting with respect to fuselage
```

```
nw=0.9;%Nonideal wake contraction
f_j=0.6;%Convergence rate coefficient
S=0/144;%Vertical fin area (ft^2)
lamda_oT=0;%Tail rotor inflow (~)
Nb_t=2;%Number of tail rotor blades
omega_t=rpm_T*(2*pi/60);
omegaR_t=omega_t*Rtr;
H_t=H_tr/Rmr;
L_t=L_tr/Rmr;
sigma_t=Nb_t*c_t/(pi*Rtr);%Tail rotor solidity ratio
A_t=pi*Rtr^2;%Tail rotor disc area
Ab_t=Nb_t*c_t*Rtr;%Tail rotor blade area (ft^2)

%====================
%Mass and Intertia
%====================
m=0.34;%Mass of the helicopter (slugs)
m_blade=0.01145;%mass of blades (slugs)
Iyy=0.1973;%Moment of inertia about y axis (slugs-ft^2)
Izz=0.1926;%Moment of inertia about z axis (slugs-ft^2)
Ixx=0.0782;%Moment of inertia about x axis (slugs-ft^2)
Ixz=0;%Product of inertia about xz plane (slug ft^2)
Ic=Ixx*Izz-Ixz^2;
k1=Ixz*(Izz+Ixx-Iyy)/Ic;
k2=Izz*((Izz-Iyy)+Ixz^2)/Ic;
k3=(Ixx*(Iyy-Ixx)-Ixz^2)/Ic;
g=32.2;
T_max=m*g; % maximum rotor thrust (lbs)

%========================
%Atmospheric Constants
%========================
gamma1=1.4;%Ratio of Specific Heats
R=1718;%Gas constant  (ft^2/(s^2 deg R))
rho0=0.002378;%Density of air at sea level  (slug/ft^3)
T0=518.67;%Sea level temperature  (deg R)
LR=-0.003333;%Lapse rate [deg R/ft)
mu0=3.737*10^-7;%Absolute Viscosity (lb s/ft^2)
h=830;
T=T0+LR*h;%Temperature at altitude  (deg R)
rho=rho0*(T/T0)^-(1+g/(R*LR));%Density of air at altitude
(slug/ft^3)

gamma=rho*a*c*Rmr^4/Ib;%Lock Number
tau_f=16/(gamma*omega);%Main rotor time constant
A_b=8/gamma*(lambda_beta^2-1);

%============================
%Stabilizer Bar Parameters
%============================
gamma_s=0.8;
tau_s=16/(gamma_s*omega);
```

```
l_1=0.637;
l_2=1.39;
l_3=1.2135;
l_4=3.96;
l_theta_c=0.762;
h_theta_c=2.711;
h_beta=1.182;
l_theta=0.593;
c_f=1.956;
l_beta=1.871;
paddle_length=4.933;
R2=10.9372;
R1=R2-paddle_length;
Alon=l_theta_c*l_1/(l_theta*(l_1+l_2))*tau_f;
Blat=Alon;
Kc=l_beta*l_2/(l_theta*(l_1+l_2));
Kd=Kc;
Ac=Alon/tau_f*Kc;
Bd=Ac;Clon=0.0117;
Dlat=Clon;
Alat=0.0025;
Blon=0.0032;

%==================================
%Inputs
%==================================
theta0_M=M_Collective_deg/57.3;
M_Collective=theta0_M;
theta0_T=T_Collective_deg/57.3;
A1=Lat_Cyclic_deg/57.3;
B1=Long_Cyclic_deg/57.3;
Long_cyclic=B1;
phi_e=0;

%Wake distortion parameter due to angular rate
KR=1.5;
KT=0.736;

V=(u^2+v^2+w^2)^.5;%Helicopter Velocity ft/sec

mu=(u+U0)/(omegaR);%advance ratio (~)
mu_z = w/omegaR;

%Stiffness Number
lamda_beta=1.05;
S_beta=8*(lamda_beta^2-1)/gamma;
K_beta=(lamda_beta^2-1)*Ib*omega^2;
Kb=K_beta/(Ib*omega^2);

%Induced Velocity in Hover
v1_i=sqrt((m*g)/(2*rho*A));
v_h=v1_i;
```

```
v_o=v1_i;
if w<0
    v1_h=-w/2+sqrt((w/2)^2+v1_i^2);
else
    v1_h=w/2+sqrt((w/2)^2+v1_i^2);
end

%Reduced Lock Number
gamma_star=gamma/(1+a*sigma/(16*v_h));

%Thrust Coefficient
CT_h=(m*g)/(rho*A*omegaR^2);
theta_075R=(3*(2*CT_h/(a*sigma)+1/2*sqrt(CT_h/2)));
omega_a=0;

% Calculate Climb Inflow Ratio
if w<0 % helicopter moving vertically up
    lamda_c=-w/(omegaR); % (~)t
elseif w>0 % helicopter moving vertically down
    lamda_c=w/omegaR;
else
    lamda_c=0;
end

%==================================================================
%Iterative Process for Calculating Coefficient of Thrust, Inflow
%Ratio, and Induced Velocity on Main Rotor
%==================================================================
[lamda,T_c]=newton_iterative(mu,nw,lamda_c,f_j,M_Collective,g,m,omeg
a,...
Rmr,rho,a,T_max,sigma,v_o,V);
lamda_i=v_h/omegaR;
lamda_i=lamda;
T_c=a/4*(2*theta0_M/3-v_h/omegaR);

%Calculation of Longitudinal Trim
[U_e,W_e,theta_e,B_1c]=long_partial_trim(u,w,g,Iyy,Izz,...

Ixx,Ixz,T_c,m,omega,Rmr,Nb,c,rho,a,cd,Ib,H_mr,Rtr,lamda_i,lamda_c,mu
);
a1s_bar=B_1c;
theta_e=0;

%Inflow Parameters
sigma_1=-a*sigma/(16*lamda_i);
tau_i=16/(45*pi*lamda_i);
sigma1=-a*sigma/(16*lamda_i)/tau_i;
KR=KR/tau_i;
sigma2=(sigma_1-1)/tau_i;

A_b=8/gamma*(1.05^2-1);
Ba=A_b;
```

```
M=[128/(75*pi)    0   0;0 -16/(45*pi) 0;0 0 -16/(45*pi)];
L_i=1/v_h*[1/2 0 0;0 -2 0;0 0 -2];

% Calculate Velocity Vector
    if w<0
        tau_c=90/180*pi;
    else
        tau_c=-90/180*pi;
    end

% ----------------------------------------
alfa_D=-(theta+tau_c); % disc incidence angle (rad)
alfa_nf=(theta-Long_cyclic); % no feathering angle
alfa_1=0; % lag hinge angle (rad)
lamda=mu*sin(alfa_nf)-lamda_i; % (~)
v_i=v1_h; % (~)
vel_comp=v_i/v_o;
a_1=2*mu*(4*M_Collective/3+lamda)/...
         (1-mu^2/2);%longitudinal flapping coefficient (~)
a_0=gamma/8*(theta0_M*(1+mu^2)+4/3*lamda);
lamda_D=mu*a_1+lamda; % (~)
gamma=rho*a*c*Rmr^4/Ib; % Locks Number (~)
A_T=pi*Rtr^2; % tail plane area (ft^2)
l_T=L_tr/Rmr; % tail rotor arm as a fraction of Rmr (~)
CH_sigma=a*lamda_D/4*(1/2*a_1);
V_T=A_T*l_T/(sigma*pi*Rmr^2);  % tail volume ratio (~)
H=H_mr/Rmr; % height of hub above cg as fraction of R (~)
L=L_mr/Rmr; % distance forward of cg from shaft in terms of R (~)
lamda_=1.25^.5; % Calculated integral (~)
C_ms=(a*(lamda_^2-1)/(2*gamma)+m*g/(rho*sigma*pi*Rmr^2*...
      omega^2*Rmr^2)*H); % Coefficient of main rotor pitch
{hingeless}(~)
ratio_hingeless=C_ms/(m*g/(rho*sigma*pi*Rmr^2*omega^2*...
     Rmr^2)*H); % Ratio to be be multiplied to a_1 for hingeless
rotor (~)

%Lift Deficiency Factor
C1_d=1/(1+a_tr*sigma_t/(16*lamda_i));

% Calculations of Derivatives
dlamda_i_dmu=(2*mu*M_Collective+alfa_D-a_1-
4*T_c*(V/v_o)*(v_i/v_o)^3/...
    (a*lamda_i))/(1+(4*T_c*(1+(v_i/v_o)^4))/(a*lamda_i)); % (~)
dlamda_dmu=alfa_D-a_1-dlamda_i_dmu; % (~)
dlamdad_dmu=a_1+dlamda_dmu;
dCT_sigma_dw=(a/4)*1/(1+a*lamda_i/(4*T_c)+(v_i/v_o)^4); % (~)
dCH_sigma_dw=0;
dCT_sigma_dtheta0=(a/6*(1+3*mu^2/2)/(1+...
a*lamda_i/(4*T_c)*(1+(v_i/v_o)^4))); % (~)
dCT_sigma_dtheta0=(a/6*1/(1+a*lamda_i/(4*T_c)*(1+(v_i/v_o)^4))); %
(~)
dCT_sigma_dtheta0=8/3*a*lamda_i/(16*lamda_i+a*sigma);
```

```
da1_dtheta0=0;
da1_dw=0;
dCT_sigma_dmu=0;
da1_dmu=8/3*theta0_M-2*v_h/omegaR;
dCT_sigma_dB1=-mu*dCT_sigma_dw; % (~)
dCH_sigma_dB1=-mu*dCH_sigma_dw; % (~)
dlamda_i_dtheta0=lamda_i/T_c*dCT_sigma_dtheta0*(1/(1+(v_i/v_o)^4));
% (~)
dlamda_d_dtheta0=mu*da1_dtheta0-dlamda_i_dtheta0; % (~)
dCH_sigma_dtheta0=(a/8)*((a_1*dlamda_d_dtheta0+lamda_D*da1_dtheta0)-
...
    2*mu*(lamda_D+M_Collective*dlamda_d_dtheta0)); % (~)
dCH_sigma_dmu=cd/4; % (~)
dCQ_sigma_dtheta0=-(lamda_D*dCT_sigma_dtheta0+T_c*dlamda_d_dtheta0)-
...
    mu*dCH_sigma_dtheta0; % (~)
dCH_sigma_dlamdad=a/4*(1/2*a_1-mu*M_Collective);
dCT_sigma_dlamdad=(1-mu^2/2)/(1+3*mu^2/2);
dCT_sigma_dlamdad_Mh=1/(8/a+sqrt(sigma/2)/sqrt(CT_h/sigma));
dCQ_sigma_dlamdad=-(lamda_D*dCT_sigma_dlamdad+T_c);
dCH_sigma_da1=a/6*theta0_M+3*a/8*lamda;
dCH_sigma_da1=3/2*T_c*(1-a/18*theta0_M/T_c);
dCH_sigma_da1=3/2*T_c*(1-a/18*theta_075R/T_c);
dlamda_i_dtheta0=lamda_i/T_c*dCT_sigma_dtheta0*(1/(1+(v_i/v_o)^4));
% (~)
dlamda_d_dtheta0=mu*da1_dtheta0-dlamda_i_dtheta0; % (~)
dlamda_dtheta0=-dlamda_d_dtheta0;
dCQ_sigma_dtheta0=-(lamda*dCT_sigma_dtheta0+T_c*dlamda_dtheta0)-...
    mu*dCH_sigma_dtheta0;
T_cd=a/4*(2/3*theta0_M+lamda_D);
dCQ_sigma_dtheta0=-
(lamda_D*dCT_sigma_dtheta0+T_cd*dlamda_d_dtheta0);
db1_dA1=mu*da1_dw;
da1_dB1=-mu*da1_dw;

%==================================================
%Basic Rotor Derivatives Near Hover
%==================================================
a0_h=gamma/8*(theta0_M+4/3*lamda);%Coning angle at hover
%Change in main rotor tip speed ratio with change in forward speed
dmu_du_Mh=1/(omegaR);
dmu_du_Th=1/omegaR_t;
%Change in tail rotor inflow ratio with change in lateral speed
dlamdad_dv_Th=-1/omegaR_t;
%Change in main rotor inflow ratio with change in forward speed
dlamdad_dw_Mh=1/(omega*Rmr);
%Change in lateral flapping with change in tip speed ratio
db1s_dmu_Mh=4/3*a0_h;
%Change in Y-force due to change in lateral flapping
dCy_sigma_db1=dCH_sigma_da1;

%=====================================
%Main Rotor Derivatives Near Hover
```

```
%=====================================
Xu_M=-rho*Ab*omegaR^2*dCH_sigma_dmu*dmu_du_Mh/m;
Xu_M=-rho*Ab*omegaR^2*dCH_sigma_da1*da1_dmu*dmu_du_Mh/m;
Zu=-rho*Ab*omegaR^2*(dCT_sigma_dmu*dmu_du_Mh)/m;
Zw_M=-2*a*Ab*rho*omegaR*lamda_i/((16*lamda_i+a*sigma)*m);
Ztheta0_M=-rho*Ab*omegaR^2*dCT_sigma_dtheta0/m/57.3;
Yv_M=Xu_M;
Mu_M=-Xu_M/Iyy*m*H_mr;
Lv_M=-Mu_M/Ixx*Iyy;
Xtheta0_M=-rho*Ab*omegaR^2*a1s_bar*dCT_sigma_dtheta0;
Mtheta0_M=-Xtheta0_M*H_mr*(m/Iyy)+Ztheta0_M*L_mr*(m/Iyy);
Ytheta0_T=rho*Ab_t*omegaR_t^2*dCT_sigma_dtheta0/m/57.3;
Ltheta0_T=Ytheta0_T*H_tr*(m/Ixx);
Ntheta0_T=Ytheta0_T*L_tr*(m/Izz);

%==========================
%Vertical Velocity Model
%==========================
Co=1;
vo=lamda_i;
C=-(rho*pi*Rmr^2*(omega*Rmr)^2)/m;
CT1=C*0.543/(Co*omega^2*Rmr);
CT2=C*4*vo/(omega*Rmr);
CT3=C*4*vo/(3*omega);
V1=(-75*pi*omega/32)*(vo+a*sigma/16)*Co;
V2=0;
V3=(25*pi*omega^2*Rmr/32)*(a*sigma/8)*Co/57.3;
CT1A=CT1*V1;
CT1B=CT1*V2;
CT1C=CT1*V3;
V4=omega^2*gamma/8*1/57.3;

%==============================================
%Main Rotor Coupling Derivatives Near Hover
%==============================================
Xv=-rho*Ab*omegaR^2*dCH_sigma_da1*db1s_dmu_Mh*dmu_du_Mh/m;
Yu=-Xv;
Lu=(Yu*H_mr)*(m/Ixx);
Mv_M=(Yu*H_mr)*(m/Iyy);
Lu=(Yu*H_mr)*(m/Ixx);

%=====================================
%Tail Rotor Derivatives Near Hover
%=====================================
Yv_T=rho*Ab_t*omegaR_t^2*dCT_sigma_dlamdad_Mh*dlamdad_dv_Th/m;
Yp_T=Yv_T*H_tr;
Yr_T=-Yv_T*L_tr;
Lv_T=Yv_T*H_tr*(m/Ixx);
Lp_T=Yp_T*H_tr*(m/Ixx);
Lr_T=Yr_T*H_tr*(m/Ixx);
Mv_T=rho*Ab_t*omegaR_t^2*Rtr*dCQ_sigma_dlamdad*dlamdad_dv_Th/Iyy;
Nv_T=-Yv_T*L_tr*(m/Izz);
```

```
Np_T=-Yp_T*L_tr*(m/Izz);
Nr_T=-Yr_T*L_tr*(m/Izz);

%================================
%Total Derivatives
%================================
Xu=Xu_M;
Xa=-g;
Yb=g;
Ma=(K_beta-H_mr*m*g)/Iyy;
Lb=(K_beta-H_mr*m*g)/Ixx;
Zw=Zw_M;
Mu=Mu_M;
Mv=Mv_M;
Yv=Yv_M+Yv_T;
Yr=Yr_T;
Lv=Lv_M+Lv_T;
Lr=Lr_T;
Nv=Nv_T;
Np=Np_T;
Yp=Yp_T;
Nr=Nr_T;

%=================================
%14-DoF 17-State Model
%=================================
A =[Xu,0,0,-g,Xv,0,0,0,Xa,0,0,0,0,0,0,0,0;
0,Zw,0,0,0,0,0,0,0,0,0,0,0,0,0,CT3+CT1B,CT2+CT1A;
Mu,0,0,0,Mv,0,0,0,Ma,0,0,0,0,0,0,0,0;
0,0,1,0,0,0,0,0,0,0,0,0,0,0,0,0,0;
Yu,0,0,0,Yv,0,g,Yr,0,Yb,0,0,0,0,0,0,0;
Lu,0,0,0,Lv,0,0,Lr,0,Lb,0,0,0,0,0,0,0;
0,0,0,0,0,1,0,0,0,0,0,0,0,0,0,0,0;
0,0,0,0,0,0,0,Nr,0,0,0,0,0,0,0,0,0;
0,0,-1,0,0,1/(omega*tau_f),0,0,-
1/tau_f,A_b/tau_f,Ac/tau_f,0,0,0,0,0,0;
0,0,-1/(omega*tau_f),0,0,-1,0,0,-Ba/tau_f,-
1/tau_f,0,Bd/tau_f,0,0,0,0,0;
0,0,-1,0,0,0,0,0,0,0,-1/tau_s,0,0,0,0,0,0;
0,0,0,0,0,-1,0,0,0,0,0,-1/tau_s,0,0,0,0,0;
0,0,(KR-sigma1)/(omega),0,0,0,0,0,0,-
sigma1,0,sigma1*Bd,sigma2,0,0,0,0;
0,0,0,0,0,(KR-
sigma1)/(omega),0,0,sigma1,0,sigma1*Ac,0,0,sigma2,0,0,0;
0,0,0,0,0,0,0,0,0,0,0,0,0,0,0,1,0;
0,0,0,0,0,0,0,0,0,0,0,0,0,0,0,-omega^2,-omega*gamma/8,-
omega*gamma/(6*Rmr);
0,0,0,0,0,0,0,0,0,0,0,0,0,0,0,0,V1];

B=[0,0,0,0;
CT1C,0,0,0;
0,0,0,0;
```

```
0,0,0,0;
0,0,0,Ytheta0_T;
0,0,0,Ltheta0_T;
0,0,0,0;
0,0,0,14;
0,Alon/tau_f,Alat/tau_f,0;
0,Blon/tau_f,Blat/tau_f,0;
0,Clon/tau_s,0,0;
0,0,Dlat/tau_s,0;
0,0,sigma1*Blat/tau_f,0;
0,sigma1*Alon/tau_f,0,0;
0,0,0,0;
V4,0,0,0;
V3,0,0,0];
```

B MATLAB Code for the 14-DoF Model of the Raptor 50 (Forward Flight)

```
function[A,B]=AB_Matrix_raptor_forward_14dof(u,w,q,theta,v,p,a1,...
    b1,c_1,d_1,v0,M_Collective_deg,Long_Cyclic_deg,...
    Lat_Cyclic_deg,T_Collective_deg)

%===============
%Main Rotor
%===============
% clc
% clear
rpm=1790;%RPM of the main rotor
Rmr=(52.95/2)/12;%Radius the main blade (ft)
Nb=2;%Number of the blades
c=2.12/12;%Blade chord (ft)
a=4.93;%3-D lift curve slope (1/rad)
cd=0.019;%Profile drag coefficient
Ib=2.21447/144;%Main rotor blade flap inertia(slugs ft^2)
H_mr=9.1/12;%Height of hub above c.g. (ft)
L_mr=-0.25/12;%Distance forward of c.g. from hub (ft)
y_mr=0;%Lateral distance from the c.g to the main rotor hub (ft)
theta1=0/57.3;%Blade twist angle (rad)a
gamma_s=0;%Main rotor shaft angle (rad)
i_m=0;%Main rotor shaft incidence
x_cg=-0.25/12;%Center of gravity relative to heli nose (ft)
i_s=0;%Shaft incidence
H=H_mr/Rmr;
L=L_mr/Rmr;
omega=rpm*(2*pi/60);
omegaR=omega*Rmr;
Sb=0.22*3.33^2;%Fuselage side area (ft^2)
U0=30;
sigma=Nb*c/(pi*Rmr);%Main rotor solidity ratio
A=pi*Rmr^2;%Tail rotor disc area
Ab=Nb*c*Rmr;%Blade area (ft^2)

%================
%Tail Rotor
%===============
rpm_T=8.5*rpm;%Tail rotor rpm
c_t=1.06/12;%Tail rotor chord (ft)
Rtr=(9.26/2)/12;%Radius of the tail rotor (ft)
L_tr=30.92/12;%Tail rotor moment arm (ft)
H_tr=3.04/12;%Vertical distance of tail rotor hub from c.g(ft)
a_tr=4.7;%3-D lift curve slope of tail rotor (1/rad)
alfa_to=0*pi/180;%No lift setting with respect to fuselage
nw=0.9;%Nonideal wake contraction
f_j=0.6;%Convergence rate coefficient
S=0/144;%Vertical fin area (ft^2)
lamda_oT=0;%Tail rotor inflow (~)
```

```
Nb_t=2;%Number of tail rotor blades
omega_t=rpm_T*(2*pi/60);
omegaR_t=omega_t*Rtr;
H_t=H_tr/Rmr;
L_t=L_tr/Rmr;
sigma_t=Nb_t*c_t/(pi*Rtr);%Tail rotor solidity ratio
A_t=pi*Rtr^2;%Tail rotor disc area
Ab_t=Nb_t*c_t*Rtr;%Tail rotor blade area (ft^2)

%============================
%Fuselage
%============================
SFP=0.012;%Fuselage Equivalent Parasite Area

%====================
%Mass and Intertia
%====================
m=0.34;%Mass of the helicopter (slugs)
m_blade=0.01145;%mass of blades (slugs)
Iyy=0.1973;%Moment of inertia about y axis (slugs-ft^2)
Izz=0.1926;%Moment of inertia about z axis (slugs-ft^2)
Ixx=0.0782;%Moment of inertia about x axis (slugs-ft^2)
Ixz=0;%Product of inertia about xz plane (slug ft^2)
g=32.2;
T_max=m*g; % maximum rotor thrust (lbs)

%========================
%Atmospheric Constants
%========================
gamma1=1.4;%Ratio of Specific Heats
R=1718;%Gas constant  (ft^2/(s^2 deg R))
rho0=0.002378;%Density of air at sea level  (slug/ft^3)
T0=518.67;%Sea level temperature  (deg R)
LR=-0.003333;%Lapse rate [deg R/ft)
mu0=3.737*10^-7;%Absolute Viscosity (lb s/ft^2)
h=830;
T=T0+LR*h;%Temperature at altitude  (deg R)
rho=rho0*(T/T0)^-(1+g/(R*LR));%Density of air at altitude
(slug/ft^3)

gamma=rho*a*c*Rmr^4/Ib;%Lock Number
tau_f=16/(gamma*omega);%Main rotor time constant

%============================
%Stabilizer Bar Parameters
%============================
gamma_s=0.8;
tau_s=16/(gamma_s*omega);
l_1=0.637;
l_2=1.39;
l_3=1.2135;
l_4=3.96;
```

```
l_theta_c=0.762;
h_theta_c=2.711;
h_beta=1.182;
l_theta=0.593;
c_f=1.956;
l_beta=1.871;
paddle_length=4.933;
R2=10.9372;
R1=R2-paddle_length;
Alon=l_theta_c*l_1/(l_theta*(l_1+l_2))*tau_f;
Blat=Alon;
Kc=l_beta*l_2/(l_theta*(l_1+l_2));
Kd=Kc;
Ac=Alon/tau_f*Kc;
Bd=Ac;
Clon=0.0117;
Dlat=Clon;
Alat=0;
Blon=0;

%==================================
%Inputs
%==================================
theta0_M=M_Collective_deg/57.3;
M_Collective=theta0_M;
theta0_T=T_Collective_deg/57.3;
A1=Lat_Cyclic_deg/57.3;
B1=Long_Cyclic_deg/57.3;
Long_cyclic=B1;
phi_e=0;

%Wake distortion parameter due to angular rate
KR=1.5;
KT=0.736;

V=(u^2+v^2+w^2)^.5;%Helicopter Velocity ft/sec
mu=(U0)/(omegaR); % advance ratio (~)
mu_z=w/omegaR;
d0=SFP/(sigma*A);
CT_sigma=(m*g)/(rho*sigma*A*(omegaR)^2);
Tc_bar = CT_sigma;
Hc_bar=1/4*mu*cd;

%Stiffness Number
lamda_beta=1.05;
S_beta=8*(lamda_beta^2-1)/gamma;
K_beta=(lamda_beta^2-1)*Ib*omega^2;
Kb=K_beta/(Ib*omega^2);
A_b=8/gamma*(lamda_beta^2-1);
Ba=A_b;

%Induced Velocity in Hover (ft/sec)
```

```
v1_i=sqrt((m*g)/(2*rho*A));
v_h=v1_i;

% Induced velocity in Vertical Flight (ft/s)
if w<0
    v1_h=-w/2+sqrt((w/2)^2+v1_i^2);
elseif w>=0 && w>v_h
    v1_h=w/2-sqrt((w/2)^2-v1_i^2);
elseif w>=0 && w<=-1.5*v_h
    v1_h=v_h*(1+w/v_h);
elseif w>-1.5*v_h && w<-2*v_h
    v1_h=v_h*(7-3*w/v_h);
else
    v1_h=w/2+sqrt((w/2)^2+v1_i^2);
end
if w<0
    v1_h=-w/2+sqrt((w/2)^2+v1_i^2);
else
    v1_h=w/2+sqrt((w/2)^2+v1_i^2);
end

%Thrust Coefficient
CT_h=(m*g)/(rho*A*omegaR^2);
theta_075R=(3*(2*CT_h/(a*sigma)+1/2*sqrt(CT_h/2)));
omega_a=0;

% Calculate Climb Inflow Ratio
% ----------------------------------------
if w<0 % helicopter moving vertically up
    lamda_c=-w/(omegaR); % (~)
elseif w>0 % helicopter moving vertically down
    lamda_c=w/omegaR;
else
    lamda_c=0;
end
v_o=v1_i; % induced velocity at hover (ft/s)

%==================================================================
% Iterative Process for Calculating Coefficient of Thrust, Inflow
% Ratio, and Induced Velocity on Main Rotor
%==================================================================
[lamda,T_c]=newton_iterative(mu,nw,lamda_c,f_j,M_Collective,g,m,omeg
a,...
Rmr,rho,a,T_max,sigma,v_o,u);
lamda_i=lamda;
[U_e,W_e,theta_e,B_1c]=long_partial_trim(u,w,g,Iyy,Izz,Ixx,Ixz,T_c,m
,...
    omegaR,Rmr,Nb,c,rho,a,cd,Ib,H_mr,Rtr,lamda_i,lamda_c,mu);
b1s_bar=-1/57.3;
a1s_bar=B_1c;

%Inflow Parameters
```

```
sigma_1=-a*sigma/(16*lamda_i);
tau_i=16/(45*pi*lamda_i);
sigma1=-a*sigma/(16*lamda_i)/tau_i;
KR=KR/tau_i;
sigma2=(sigma_1-1)/tau_i;

M =[128/(75*pi)    0   0;0 -16/(45*pi) 0;0 0 -16/(45*pi)];
L_i = 1/v_h*[1/2 0 0;0 -2 0;0 0 -2];

%============================
% Calculate Velocity Vector
% ==========================
if mu<=0.08
    if w<0
        tau_c=90/180*pi;
    else
        tau_c=-90/180*pi;
    end
else
    tau_c=atan(-(w)/(u));
end

% theta = B1-a_1-CH_sigma/Tc_bar-1/2*mu^2*d0/Tc_bar;
theta=-2/57.3;
alfa_D=-(theta+tau_c); % disc incidence angle (rad)
alfa_nf=(theta-Long_cyclic);% no feathering angle
alfa_1=0;%lag hinge angle (rad)
lamda=mu*sin(alfa_nf)-lamda_i; % (~)
v_i=v1_h; % (~)
vel_comp=v_i/v_o;
a_1=2*mu*(4*M_Collective/3+lamda)/(1-mu^2/2);%longitudinal flapping
angle
a_0=gamma/8*(theta0_M*(1+mu^2)+4/3*lamda);
lamda_D=mu*a_1+lamda; % (~)
gamma=rho*a*c*Rmr^4/Ib; % Locks Number (~)
A_T=pi*Rtr^2; % tail plane area (ft^2)
l_T=L_tr/Rmr; % tail rotor arm as a fraction of Rmr (~)
CH_sigma=1/4*mu*cd*+a*mu*lamda_D/4*(theta0_M/3*(1-9*mu^2/2)+...
    lamda_D)/(1+3*mu^2/2);
CQ_sigma=cd*(1+3*mu^2)/8-lamda_D*T_c-mu*CH_sigma;
lamda_=1.25^.5;%Calculated integral (~)
C_ms=(a*(lamda_^2-1)/(2*gamma)+m*g/(rho*sigma*pi*Rmr^2*...
    omega^2*Rmr^2)*H); % Coefficient of main rotor pitch
{hingeless}(~)
ratio_hingeless=C_ms/(m*g/(rho*sigma*pi*Rmr^2*omega^2*...
    Rmr^2)*H); % Ratio to be be multiplied to a_1 for hingeless
rotor (~)

%=======================================
%Basic Derivatives in Forward Flight
%=======================================
dlamda_i_dmu=(2*mu*M_Collective+alfa_D-a_1-
```

```
4*T_c*(V/v_o)*(v_i/v_o)^3/...
    (a*lamda_i))/(1+(4*T_c*(1+(v_i/v_o)^4))/(a*lamda_i)); % (~)
dlamda_dmu=alfa_D-a_1-dlamda_i_dmu; % (~)
dCH_sigma_dq=-4*a/(gamma*(1-mu^2/2))*(lamda/2+mu*a_1-...
    mu^2*M_Collective); % (~)
dlamda_i_dw=(a*lamda_i/(4*T_c)+(v_i/v_o)^4)/(1+a*lamda_i/(4*T_c)+...
    (v_i/v_o)^4); % (~)
da1_dtheta0=8*mu/3*1/(1-mu^2/2)*(1-(.5*a*sigma*(1+...
    3*mu^2/2))/(8*mu+a*sigma)); % (~)
dCT_sigma_dmu=2*a*mu/(8*mu+a*sigma)*(2*mu*M_Collective+...
    alfa_nf+sigma*T_c/(2*mu^2));
dlamda_i_dmu=sigma/2*(dCT_sigma_dmu/mu-T_c/mu^2);
dlamda_dmu=alfa_nf-dlamda_i_dmu;
da1_dmu=(a_1/mu-(2*mu/(1-mu^2/2))*dlamda_dmu);
dCH_sigma_dmu=cd/4;% (~)
dCT_sigma_dw=2*mu/(8*mu+a*sigma); %(~)
da1_dw=16*mu^2/((1-mu^2/2)*(8*mu+a*sigma));
v_1=(1-sin(alfa_D))/(1+sin(alfa_D));
da0_dmu=gamma/8*(2*theta0_M*mu+4/3*dlamda_dmu);
db1_dmu=(a_0+mu*da0_dmu+1.1*v_1^0.5*dlamda_i_dmu)/(1+mu^2)-...
    2*(mu*a_0+1.1*v_1^0.5*lamda_i)*mu/(1+mu^2)^2;
dCH_sigma_da1=a/2*(theta0_M/3+3/4*lamda+1/2*mu*a_1);
dCY_sigma_db1=dCH_sigma_da1;
dlamdad_dmu=a_1+mu*da1_dmu+dlamda_dmu;
da1_dlamdad=2*mu/(1+3*mu^2/2);
dCT_sigma_dtheta0=4/3*(a*mu*(1+1.5*mu^2)/(8*mu+a*sigma));
dCH_sigma_dw=4*a*mu^2/(8*mu+a*sigma)*(M_Collective*(1-
9*mu^2/2)/6+...
    lamda_D)/(1-mu^2/2);
dCT_sigma_dB1=-mu*dCT_sigma_dw; % (~)
dCH_sigma_dB1=-mu*dCH_sigma_dw; % (~)
dlamda_i_dtheta0=lamda_i/T_c*dCT_sigma_dtheta0*(1/(1+(v_i/v_o)^4));
% (~)
dlamda_d_dtheta0=mu*da1_dtheta0-dlamda_i_dtheta0; % (~)
dCH_sigma_dtheta0=(a/8)*((a_1*dlamda_d_dtheta0+lamda_D*da1_dtheta0)-
...
    2*mu*(lamda_D+M_Collective*dlamda_d_dtheta0)); % (~)
dCQ_sigma_dtheta0=-(lamda_D*dCT_sigma_dtheta0+T_c*dlamda_d_dtheta0)-
...
    mu*dCH_sigma_dtheta0;
dCH_sigma_dlamdad=a/4*(1/2*a_1-mu*M_Collective);
dCT_sigma_dlamdad=a/4*(1-mu^2/2)/(1+3*mu^2/2);
% dCT_sigma_dlamdad_Mh = 1/(8/a+sqrt(sigma/2)/sqrt(CT_h/sigma));
dCQ_sigma_dlamdad=-
(T_c+lamda_D*dCT_sigma_dlamdad+mu*dCH_sigma_dlamdad);
dCH_sigma_da1=a/6*theta0_M+3*a/8*lamda;
dCH_sigma_da1=3/2*T_c*(1-a/18*theta0_M/T_c);
dCH_sigma_da1=3/2*T_c*(1-a/18*theta_075R/T_c);
dlamda_i_dtheta0=lamda_i/T_c*dCT_sigma_dtheta0*(1/(1+(v_i/v_o)^4));
% (~)
dlamda_d_dtheta0=mu*da1_dtheta0-dlamda_i_dtheta0; % (~)
dlamda_dtheta0=-dlamda_d_dtheta0;
dCQ_sigma_dtheta0=-(lamda*dCT_sigma_dtheta0+T_c*dlamda_dtheta0)-...
```

```
mu*dCH_sigma_dtheta0;
dCT_sigma_dw=(a/4)*1/(1+a*lamda_i/(4*T_c)+(v_i/v_o)^4); % (~)
T_cd=a/4*(2/3*theta0_M+lamda_D);
dCQ_sigma_dmu=3/4*mu*cd-dlamdad_dmu*T_c*lamda_D*dCT_sigma_dmu-...
    mu*dCH_sigma_dmu-CH_sigma;
% dCQ_sigma_dtheta0 = -
(lamda_D*dCT_sigma_dtheta0+T_cd*dlamda_d_dtheta0);
db1_dA1=mu*da1_dw;
da1_dB1=-mu*da1_dw;
dlamdad_da1=mu;
m_u_f=0; % pitching derivative of the fuselage
m_w_f=0; % pitching derivative of the fuselage
m_q_f=0; % pitching derivative of the fuselage

%==============================================
%Basic Rotor Derivatives in Forward Flight
%==============================================
%Coning angle at hover
a0_h=2/3*gamma*(T_c)/a - 3/2*g*Rmr/(omegaR)^2;
a0_h=gamma/8*(theta0_M+4/3*lamda);
%Change in main rotor tip speed ratio with change in forward speed
dmu_du=1/omegaR;
dmu_du_T=1/omegaR_t;
dbeta_dv=1/U0;
%Change in tail rotor inflow ratio with change in lateral speed
dlamdad_dv_T=-1/(omegaR_t*(1+dCT_sigma_dlamdad*sigma_t/(2*mu)));
%Change in main rotor inflow ratio with change in forward speed
dlamdad_dw=1/(omegaR*(1+dCT_sigma_dlamdad*sigma/(2*mu)));
%Change in lateral flapping with change in tip speed ratio
db1s_dmu_Mh=4/3*a0_h;
%Change in Y-force due to change in lateral flapping
dCy_sigma_db1=dCH_sigma_da1;

%=====================================
%Longitudinal Derivative Parameters
%=====================================
x_u=-T_c*da1_dmu-sin(alfa_D)*dCT_sigma_dmu-...
    dCH_sigma_dmu; % force/translational velocity (~)
x_w=(-T_c*da1_dw-sin(alfa_D)*dCT_sigma_dw-...
    dCH_sigma_dw); % force/translational velocity (~)
z_u=(-dCT_sigma_dmu); % force/translational velocity (~)
z_w=(-dCT_sigma_dw); % force/translational velocity (~)
m_u=(-H*x_u+L*z_u+C_ms*da1_dmu+m_u_f); % moment/translational
velocity (~)
m_w=(-H*x_w+L*z_w+C_ms*da1_dw+m_w_f); % moment/translational
velocity (~)
x_col=(-T_c*da1_dtheta0-sin(alfa_D)*dCT_sigma_dtheta0-...
    dCH_sigma_dtheta0); % force/control (~)
x_long=(dCT_sigma_dB1*sin(alfa_D)+T_c*(1+mu*da1_dw)-...
    dCH_sigma_dB1); % force/control (~)
z_col=(-dCT_sigma_dtheta0); % force/control (~)
z_long=(-dCT_sigma_dB1); % force/control (~)
m_col=(-H*x_col+L*z_col-C_ms*da1_dtheta0); % moment/control (~)
```

```
%Lift Deficienncy Factor
C_1=1/(1+sigma_t*a_tr/(8*lamda_i));
C_2=1/(1+sigma*a/(8*lamda_i));
M_star=1/g*gamma*(2*CT_h/(sigma*a));

%========================
%Helicopter Derivatives
%========================
Xu_M=x_u/m*(rho*sigma*pi*Rmr^2*omega*Rmr); % (1/s)
Xw_M=x_w/m*(rho*sigma*pi*Rmr^2*omega*Rmr); % (1/s)
Xtheta0_M=1*x_col/m*(rho*sigma*pi*Rmr^2*(omega*Rmr)^2)/57.3; %
(ft/s^2)
Yv_M=rho*Ab*omegaR^2*(Hc_bar+Tc_bar*(B1+a1s_bar))/m;
Zu_M=1*z_u/m*(rho*sigma*pi*Rmr^2*omegaR); % (1/s)
Zw_M = -4*a*Ab*rho*mu*omegaR/((8*mu+a*sigma)*2*m);
ZB1_M = -rho*Ab*omegaR^2*dCT_sigma_dlamdad*dlamdad_da1*da1_dB1/m;
Ztheta0_M=-
4/3*a*Ab*rho*omegaR^2*mu*(1+1.5*mu^2)/((8*mu+a*sigma)*m)/57.3;
Lv_M = Yv_M*H_mr*(m/Ixx);
Mu_M=(m_u/Iyy*(rho*sigma*pi*Rmr^2*omega*Rmr^2)-...
    (rho*A_T*l_T*Rmr*(V*a_tr*(alfa_to+(theta)-sin(tau_c))+...
    0.5*a_tr*(V*dlamda_i_dmu-lamda_i*omega*Rmr)))/Iyy); % (1/(ft-s)
Mtheta0_M=1*m_col/Iyy*(rho*sigma*pi*Rmr^2*omega^2*Rmr^3); % (1/s^2)
Mtheta0_M = Ztheta0_M*L_mr*m/Iyy;
Mu_M = (-Xu_M*H_mr+Zu_M*L_mr)*m/Iyy;
Mw_M = (Zw_M*L_mr)*m/Iyy;
Mtheta0_M = Ztheta0_M*L_mr*(m/Iyy);

%==============================
%Vertical Velocity Model
%==============================
Co=1;
vo=lamda_i;
C=-(rho*pi*Rmr^2*(omega*Rmr)^2)/m;
CT1=C*0.543/(Co*omega^2*Rmr);
CT2=C*4*vo/(omega*Rmr);
CT3=C*4*vo/(3*omega);
V1=(-75*pi*omega/32)*(vo+a*sigma/16)*Co;
V2=0;
V3=(25*pi*omega^2*Rmr/32)*(a*sigma/8)*Co/57.3;
CT1A=CT1*V1;
CT1B=CT1*V2;
CT1C=CT1*V3;
V4=omega^2*gamma/8*1/57.3;

%=======================================================
%Main Rotor Coupling Derivatives In Forward Flight
%=======================================================
Xv=rho*Ab*omegaR^2*Tc_bar*(A1-b1s_bar)*dbeta_dv/m;
Yu=rho*Ab*omegaR^2*(dCY_sigma_db1*db1_dmu+b1s_bar*dCT_sigma_dmu)*dmu
_du/m;
```

```
Mv=-(Xv*H_mr)*(m/Iyy);
Lu=(Yu*H_mr)*(m/Ixx);

%=========================================
%Tail Rotor Derivatives in Forward Flight
%=========================================
Yv_T=rho*Ab_t*omegaR_t^2*dCT_sigma_dlamdad*dlamdad_dv_T/m;
Yp_T=Yv_T*H_tr;
Yr_T=-Yv_T*L_tr;
Lv_T=Yv_T*H_tr*(m/Ixx);
Lp_T=Yp_T*H_tr*(m/Ixx);
Lr_T=Yr_T*H_tr*(m/Ixx);
Mv_T=rho*Ab_t*omegaR_t^2*Rtr*dCQ_sigma_dlamdad*dlamdad_dv_T/Iyy;
Mr_T=-Mv_T*L_tr;
Nv_T=-Yv_T*L_tr*(m/Izz);
Np_T=Yp_T*L_tr*(m/Izz);
Nr_T=-Yr_T*L_tr*(m/Izz);
Ytheta0_T=rho*Ab_t*omegaR_t^2*dCT_sigma_dtheta0/m/57.3;
Ltheta0_T=Ytheta0_T*H_mr*m/Ixx;
Ntheta0_T = Ytheta0_T*L_tr*(m/Izz);

%======================
%Total Derivatives
%======================
Xu=Xu_M;
Xa=-g;
Yb=g;
Ma=(K_beta-H_mr*m*g)/Iyy;
Lb=(K_beta-H_mr*m*g)/Ixx;
Xw=Xw_M;
Zu=Zu_M;
Zw=Zw_M;
ZB1=ZB1_M;
Mu=Mu_M;
Mw=Mw_M;
Mv=Mv;
Yv=Yv_M+Yv_T;
Yr=Yr_T;
Lv=Lv_M;
Lr=Lr_T;
Nv=Nv_T;
Np=Np_T;
Yp=Yp_T;
Nr=Nr_T;

%================================
%14-DoF 17-State Model
%================================
A =[Xu,0,0,-g,Xv,0,0,0,Xa,0,0,0,0,0,0,0,0;
0,Zw,0,0,0,0,0,0,0,0,0,0,0,0,0,CT3+CT1B,CT2+CT1A;
Mu,Mw,0,0,Mv,0,0,0,Ma,0,0,0,0,0,0,0,0;
0,0,1,0,0,0,0,0,0,0,0,0,0,0,0,0,0;
```

```
Yu,0,0,0,Yv,0,g,Yr,0,Yb,0,0,0,0,0,0,0;
Lu,0,0,0,Lv,0,0,Lr,0,Lb,0,0,0,0,0,0,0;
0,0,0,0,0,1,0,0,0,0,0,0,0,0,0,0,0;
0,0,0,0,Nv/100,Np,0,Nr,0,0,0,0,0,0,0,0,0;
0,0,-1,0,0,1/(omega*tau_f),0,0,-
1/tau_f,A_b/tau_f,Ac/tau_f,0,0,0,0,0,0;
0,0,-1/(omega*tau_f),0,0,-1,0,0,-Ba/tau_f,-
1/tau_f,0,Bd/tau_f,0,0,0,0,0;
0,0,-1,0,0,0,0,0,0,0,-1/tau_s,0,0,0,0,0,0;
0,0,0,0,0,-1,0,0,0,0,0,-1/tau_s,0,0,0,0,0;
0,0,(KR-sigma1)/(omega),0,0,0,0,0,0,-
sigma1,0,sigma1*Bd,sigma2,0,0,0,0;
0,0,0,0,0,(KR-
sigma1)/(omega),0,0,sigma1,0,sigma1*Ac,0,0,sigma2,0,0,0;
0,0,0,0,0,0,0,0,0,0,0,0,0,0,0,0,1,0;
0,0,0,0,0,0,0,0,0,0,0,0,0,0,0,-omega^2,-omega*gamma/8,-
omega*gamma/(6*Rmr);
0,0,0,0,0,0,0,0,0,0,0,0,0,0,0,0,0,V1];

B=[0,0,0,0;
CT1C,0,0,0;
0,0,0,0;
0,0,0,0;
0,0,0,Ytheta0_T;
0,0,0,Ltheta0_T;
0,0,0,0;
0,0,0,Ntheta0_T;
0,Alon/tau_f,Alat/tau_f,0;
0,Blon/tau_f,Blat/tau_f,0;
0,Clon/tau_s,0,0;
0,0,Dlat/tau_s,0;
0,0,sigma1*Blat/tau_f,0;
0,sigma1*Alon/tau_f,0,0;
0,0,0,0;
V4,0,0,0;
V3,0,0,0];
```

C Simulink Implementation of the High-Order LPV Model

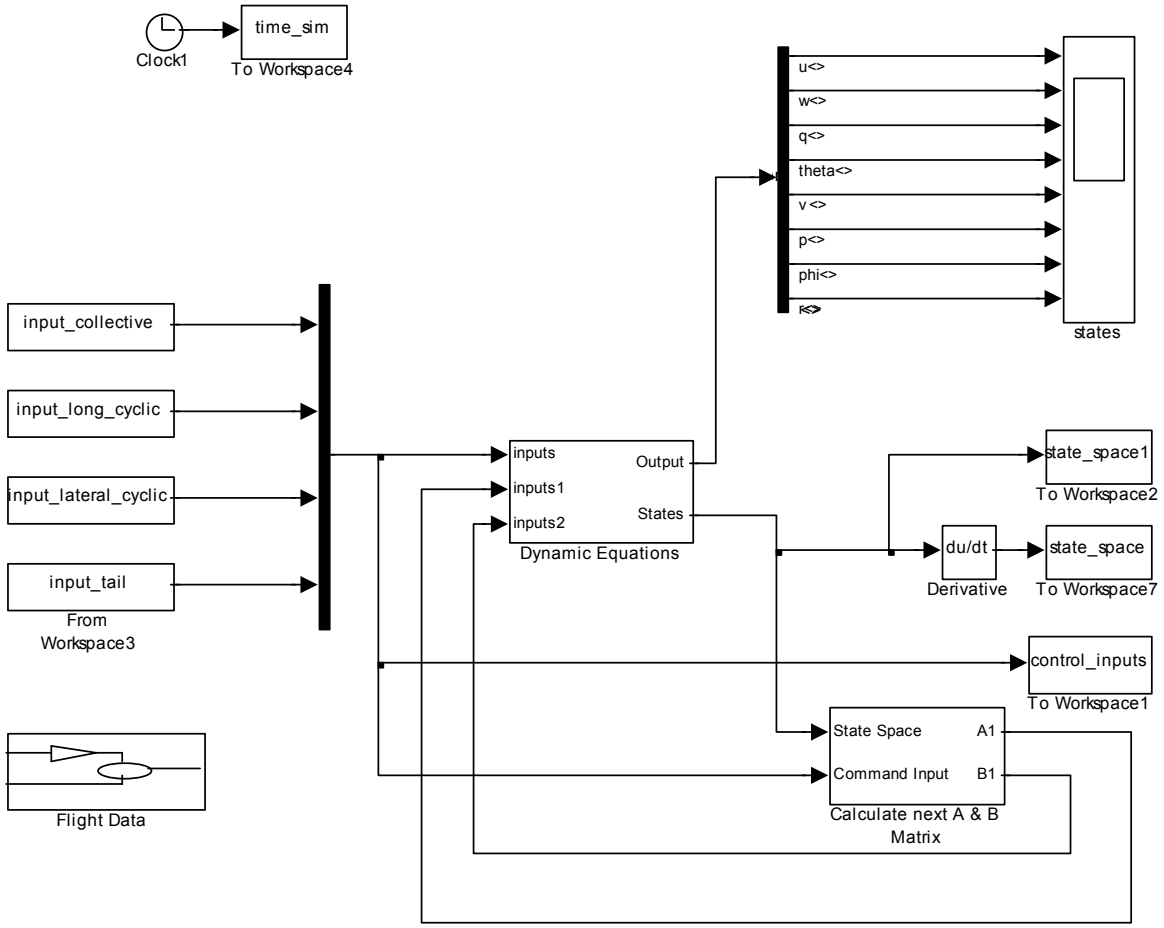

D Sample MATLAB Code for Running the Simulation

```
%%%%%%%%%%%%%%%%%%%%%%%%%%%%%%%%%%%%%%%%%%%%%%%%%
% run_raptor_sim_14.m
% Created by Subodh Bhandari
% University of Kansas
% Department of Aerospace Engineering
% April 2007
%%%%%%%%%%%%%%%%%%%%%%%%%%%%%%%%%%%%%%%%%%%%%%%%%
clc
clear

% This is a 14-DOF dynamics simulation for a Thunder Tiger
% Raptor 50 V2 Helicopter. This file runs the simulation while
initializing
% the necessary parameters.

flight_data=
oad('091604_pitch_1_conversion_conversion_flight_data.txt');
%flight_data=load('091604_roll_2_conversion_conversion_flight_data.t
xt.');
%flight_data=load('092404_yaw_1_conversion_conversion_flight_data.tx
t');
%flight_data=load('071906_sweep_conversion_conversion_flight_data.tx
t.');



%------------------------------------
    original_flight_time=flight_data(1,1);
    time = flight_data(:,1);
% For Comparing Flight Data to Simulation Data
    p1 = flight_data(:,5);
    q1 = flight_data(:,6);
    r1 = flight_data(:,7);
    nx=[flight_data(:,1),-flight_data(:,2)];
    ny=[flight_data(:,1),flight_data(:,3)];
    nz=[flight_data(:,1),flight_data(:,4)];
    p=[flight_data(:,1),flight_data(:,5)];
    q=[flight_data(:,1),flight_data(:,6)];
    r=[flight_data(:,1),flight_data(:,7)];
    i_long=[flight_data(:,1),flight_data(:,8)];
    i_lat=[flight_data(:,1),flight_data(:,9)];
    i_tail=[flight_data(:,1),flight_data(:,10)];
    i_col=[flight_data(:,1),flight_data(:,11)];
    sonar=[flight_data(:,1),flight_data(:,12)];

% User Interface
%--------------------------------------

    disp('Welcome to the Raptor 50 V2 Simulation');
    tstart = input(' enter start time:    ');
```

```
    tmax=input('  enter tmax:   ');
    tmax=original_flight_time+tmax;

% Simulation Parameters
    t0=original_flight_time;
%     t00=t0;
%     tstart = t0;
    start_time=tstart;
    tend=tmax;
    stop_time=tend;
% Set Simulation Step
    simdt=1;
    simdt0=simdt/10;

    step_size=simdt;
    tsave=simdt;
    timespan=[tstart:tsave:tend];
    disp(['computing from ',num2str(tstart),' to ',num2str(tmax),...
        ' Seconds'])
    optionssim=[];
    optionssim=simset(...
        'Solver','FixedStepDiscrete',...
        'MaxStep',simdt,...
        'RelTol',1e-3,...
        'AbsTol',1e-6,...
        'InitialStep',simdt0,...
        'OutputPoints','specified');

%==============================
% Initial Conditions
%==============================
    [size_a size_b]=size(flight_data);
    input_collective=[flight_data(:,1),(flight_data(:,11))];
%     input_collective=[flight_data(:,1),zeros(len,1)];
    len = length(input_collective(:,1));
    input_long_cyclic=[flight_data(:,1),(flight_data(:,8))];
    input_long_cyclic=[flight_data(:,1),zeros(len,1)];

    input_lateral_cyclic=[flight_data(:,1),flight_data(:,9)];
%   input_lateral_cyclic=[flight_data(:,1),zeros(len,1)];
    input_tail=[flight_data(:,1),flight_data(:,10)];
%   input_tail=[flight_data(:,1),zeros(len,1)];

    u=0; % initial forward velocity  (ft/s)
    w=0; % initial vertical velocity (ft/s)
    v=0;
    theta0_M = flight_data(1,11); % initial main rotor collective
(deg)
    A1 = flight_data(1,9);
    theta0_T = flight_data(1,10);
    B1 = flight_data(1,8);
    theta=0/180*pi; % initial helicopter body pitch angle (rad)
```

```
    u_dot=nx(1,2)*0;
    w_dot=nz(1,2)*0;
    q_dot=q(1,2)/180*pi;
    theta_dot=q(1,2)/180*pi;
    v_dot = 0;
    p_dot = 0;
    r_dot = 0;
    phi_dot = 0;
    q_0=flight_data(1,6);
    p_0 = flight_data(1,5);
    r_0 = flight_data(1,7);
    a_0 = 0;
    a1=0;
    b1=0;
    c1=0;
    d1=0;
    v_0 = 0;
    l_c = 0;
    l_s = 0;

%============================
%Run Simulation
%============================
freq=120; % Sampling frequency of flight data (Hz)
sim('uav_sim_flight_data',[tstart tend]);
u0=0;
v0=0;
w0=0;
p0=flight_data2(1,4);
q0=flight_data2(1,5);
r0=flight_data2(1,6);
theta0_M= flight_data2(1,10);
B1 = flight_data2(1,7);
A1 = flight_data2(1,8);
theta0_T = flight_data2(1,9);

%=====================================================================
=
% Build Helicopter State-Space System Matrix (A) and Control
% Input Matrix (B) and State-Space Output Matrix (C & D Matrix)
%=====================================================================
=
[A,B]=AB_Matrix_raptor_hover_14dof(u,v,w,theta,theta0_M,B1,A1,theta0
_T);
C=eye(17);
D=zeros(17,4);
sim('uav_sim_hover_14dof',[tstart tend]);
```

E Flight Test Data used for the Model Verification

Figure No.	Time History Data File used for Verification
41	Longitudinal Sweep: ***091604_pitch_1.txt*** Lateral Sweep: ***091604_roll_2.txt*** Vertical Sweep: ***Flight_Test_01-20-07_1.txt*** Directional Sweep: ***092404_yaw_1.txt***
42	Longitudinal Sweep: ***051104_pitch_forward_1.txt*** Lateral Sweep: ***051104_roll_forward_1.txt*** Vertical Sweep: ***020607_forward_1.txt*** Directional Sweep: ***081104_yaw_forward_1.txt***
43	***Flight_Test_01-20-07_1.txt***
44	***020607_forward_2.txt***

The time history data are included in the accompanying CDs.